POLITECNICO
MILANO 1863

SCUOLA DI INGEGNERIA INDUSTRIALE
E DELL'INFORMAZIONE

Study of optimized HTS solenoid configurations for the beam cooling of a Muon Collider

Tesi di Laurea Magistrale in
Nuclear Engineering - Ingegneria Nucleare

Author: **Jonathan Pavan**

Student ID: 976486
Advisor: Prof. Marco Beghi, Politecnico di Milano
Co-advisors:
Prof. Lucio Rossi: UNIMI, Prof. Marco Statera: INFN-LASA (Milan)
Dr. Luca Bottura, Dr. Bernardo Bordini: CERN, Geneva (Switzerland)
Academic Year: 2022-23

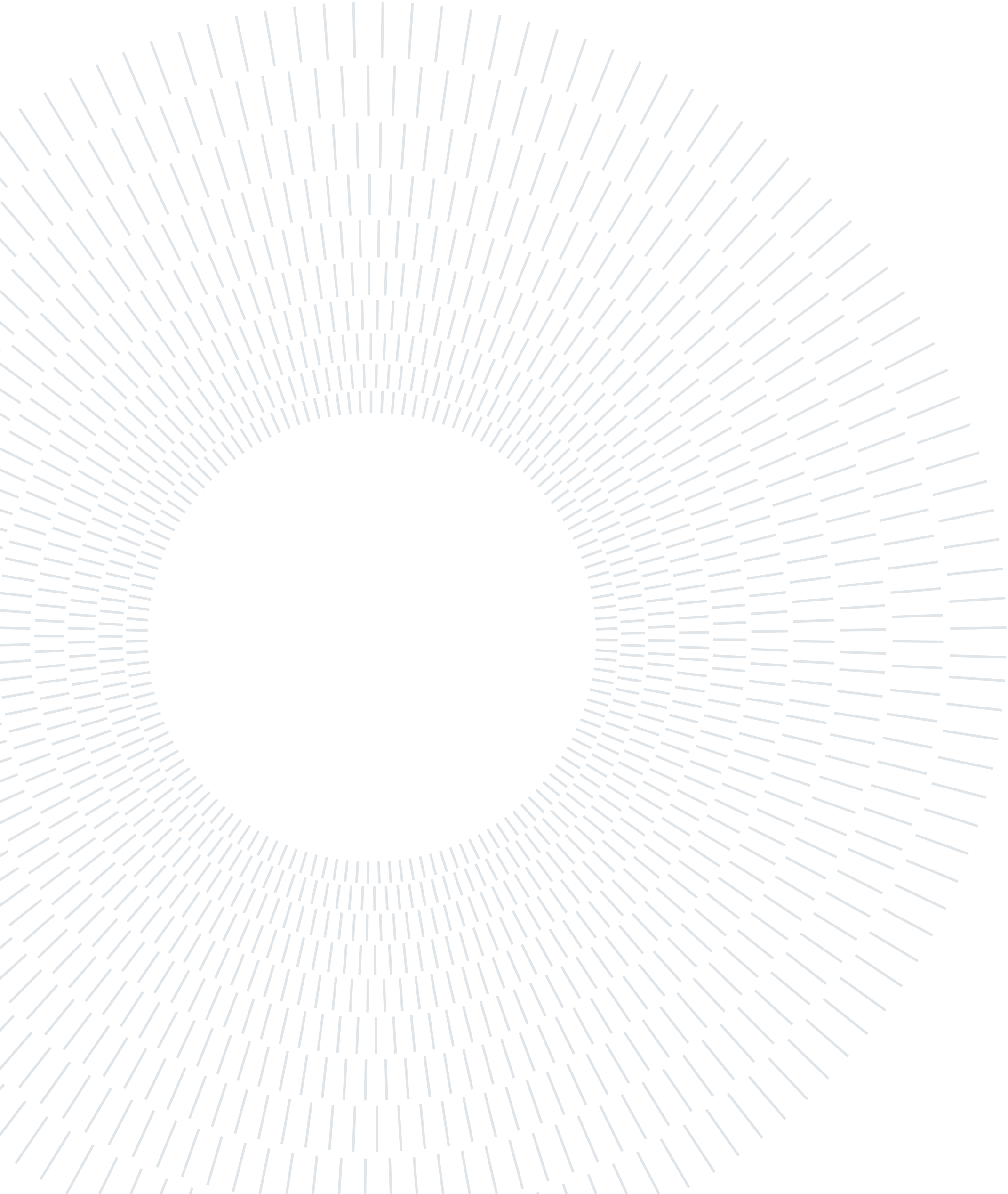

In collaboration with

CERN

INFN

UNIVERSITÀ
DEGLI STUDI
DI MILANO

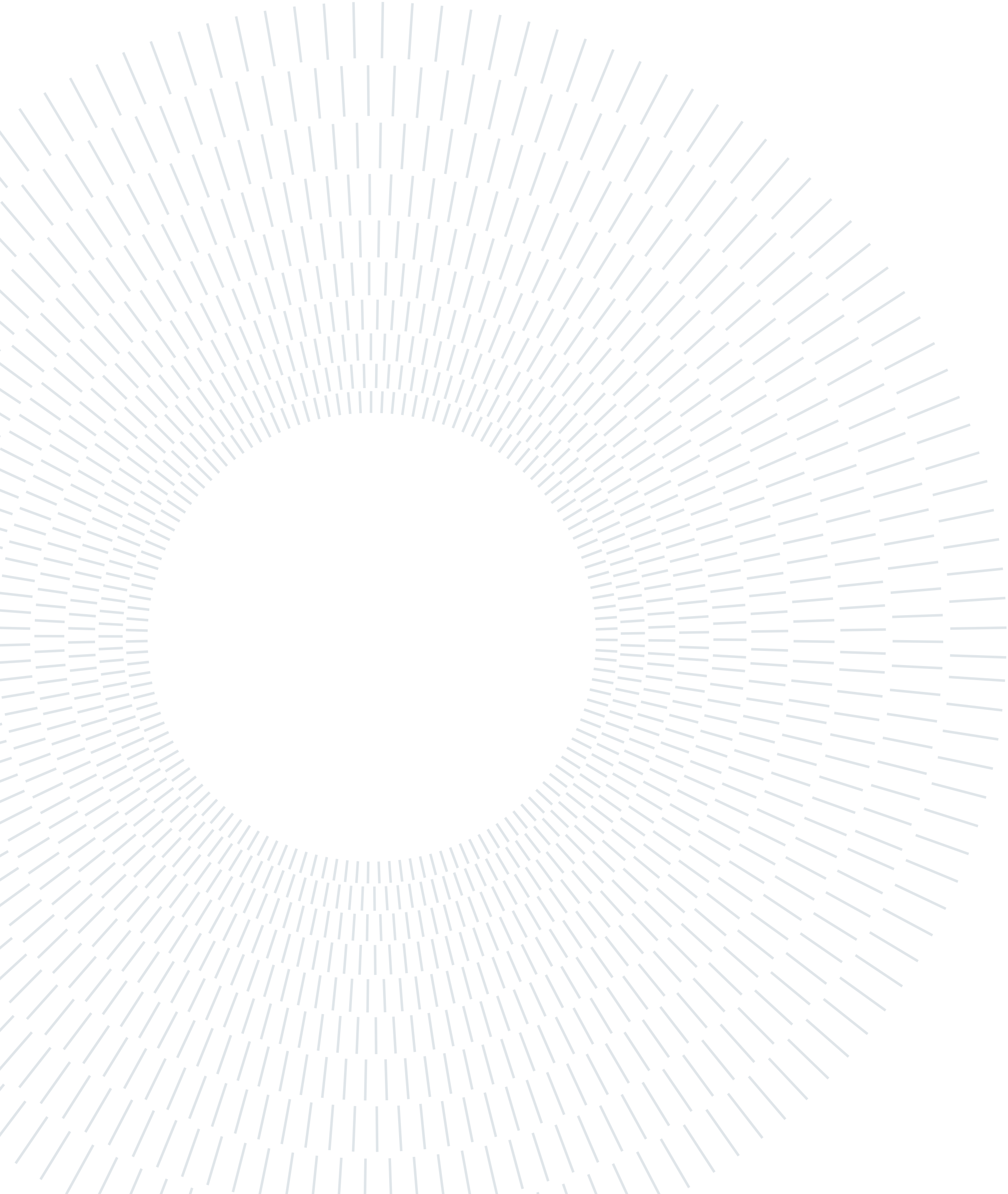

Abstract

The extraordinary ability of superconductors to transport vast amounts of electric current without any resistance is exploited, among other applications, in the design and construction of magnets for high-energy physics. Over the years, no other branch of science has grown to be more dependant upon superconductivity than this field. Physicists seek for magnets which provide increasingly higher and higher fields, to accelerate more, and more tightly, bunches of particles with the hope of unraveling the intricate mysteries of the Universe. This is also the scope of the Muon Collider, one of the possible candidates for the next generation of particle accelerators. This collider, differently from any other machines ever built, will accelerate unstable particles, muons. Muons share the same properties as electrons, except they are 200 times heavier and they decay into an electron and two neutrinos in 2.2 μs . This peculiar behaviour makes the Muon Collider design a challenge and potentially poses an even greater obstacle to its practical implementation. This is particularly true for the subject of this thesis work, the solenoids of the 6D Cooling stage of the Muon Collider. There are 12 different stages and 18 different types of solenoids, for a total number of 2954 magnets. The objective of the first half of this work was to characterize each stage and solenoid in terms of their magnetic and mechanical properties. To achieve this goal, various tools were employed, from analytical instruments to FEM simulations. This analysis assumes particular significance as it provides a comprehensive estimation of the characteristics of all the magnets involved, thereby serving as a valuable tool for evaluating the challenges that lie ahead in the future. The second part of the thesis focuses on the analysis of the quench protection aspect. For this purpose, a 1D FEM model of a quench event has been implemented in Comsol Multiphysics. The model provided an understanding of both the behaviour of a solenoid when subjected to a quench, and the underlying quench phenomenon itself. This allowed for a deeper analysis and improved knowledge of the dynamics and characteristics associated with both aspects.

Keywords: Superconductivity, magnets, FEM, Comsol, Quench

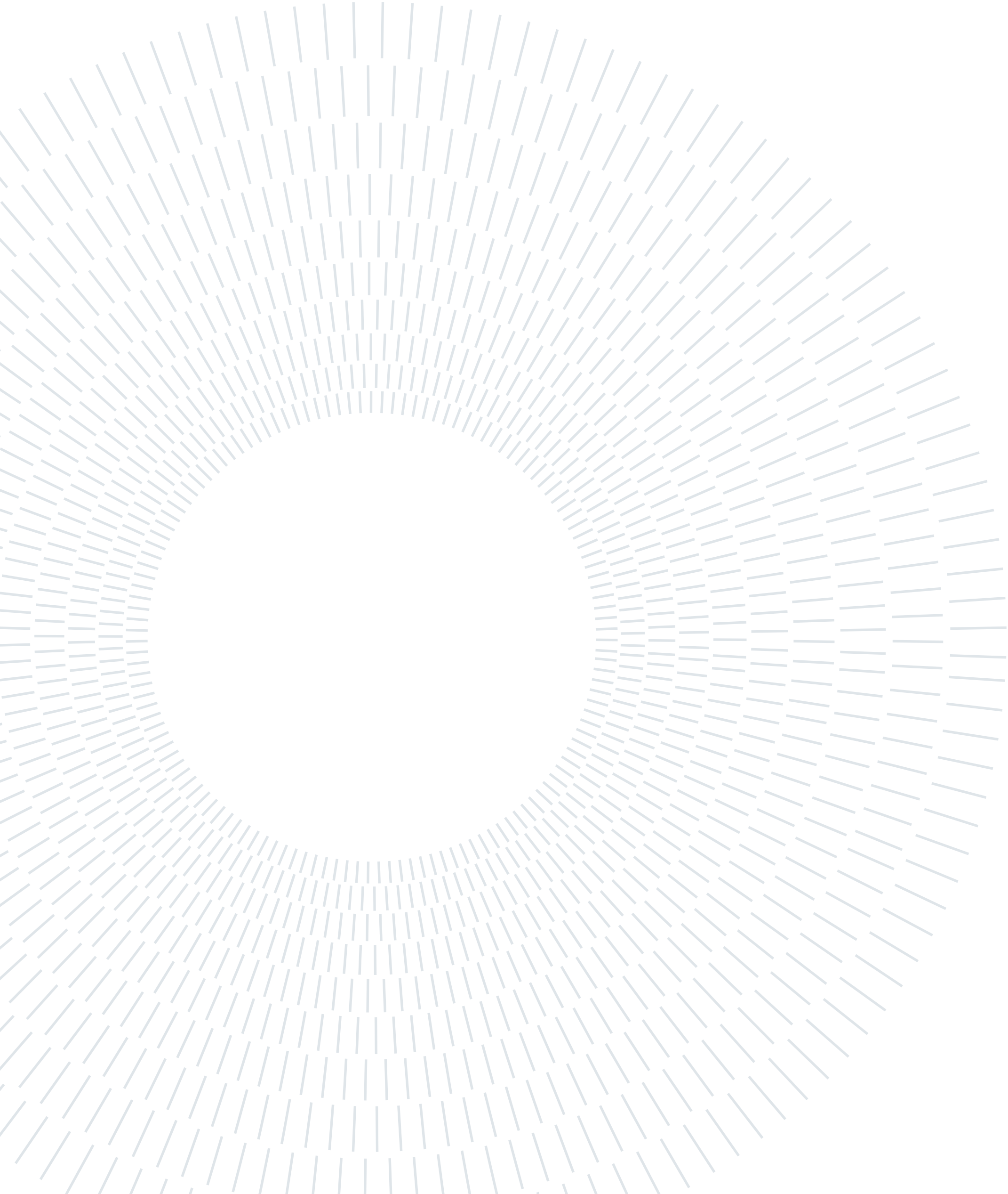

Abstract in lingua italiana

La straordinaria capacità dei superconduttori di trasportare grandi quantità di corrente elettrica senza alcuna resistenza viene sfruttata, tra le altre applicazioni, nella progettazione e costruzione di magneti per la fisica delle alte energie. Nel corso degli anni, nessun'altra branca della scienza è diventata più dipendente dalla superconduttività di questo campo. I fisici sono alla ricerca di magneti che forniscano campi sempre più elevati, per accelerare più velocemente pacchetti di particelle sempre più densi, con la speranza di svelare gli intricati misteri dell'Universo. Questo è anche lo scopo del Muon Collider, uno dei possibili candidati per la prossima generazione di acceleratori di particelle. Questo collisore, a differenza di qualsiasi altra macchina mai costruita, accelererà particelle instabili, i muoni. I muoni hanno le stesse proprietà degli elettroni, ma sono 200 volte più pesanti e decadono in un elettrone e due neutrini in 2.2 μs. Questo comportamento peculiare rende il progetto del collisore di muoni una sfida e, potenzialmente, pone un ostacolo ancora maggiore alla sua realizzazione pratica. Ciò è particolarmente vero per l'oggetto di questo lavoro di tesi, i solenoidi della sezione denominata 6D Cooling. Questa è composta da 12 diversi stadi e 18 diversi tipi di solenoidi, per un numero totale di 2954 magneti. L'obiettivo di questo lavoro è stato quello di caratterizzare ogni stadio e solenoide in termini delle loro proprietà magnetiche e meccaniche. Per raggiungere questo obiettivo sono stati utilizzati diversi strumenti, dalle formule analitiche alle simulazioni FEM. Questa analisi assume un significato particolare in quanto fornisce una stima completa delle caratteristiche di tutti i magneti coinvolti, fungendo così da strumento prezioso per valutare le sfide che attendono in futuro. La seconda parte della tesi si concentra sull'aspetto della protezione dal quench. A tale scopo, è stato implementato in Comsol Multiphysics un modello FEM 1D di un evento di quench. Il modello ha permesso di comprendere sia il comportamento di un solenoide quando è sottoposto a un quench, sia il fenomeno del quench stesso. Ciò ha consentito un'analisi più approfondita e una migliore conoscenza delle dinamiche e delle caratteristiche associate a entrambi gli aspetti.

Parole chiave: Superconduttività, magneti, FEM, Comsol, Quench

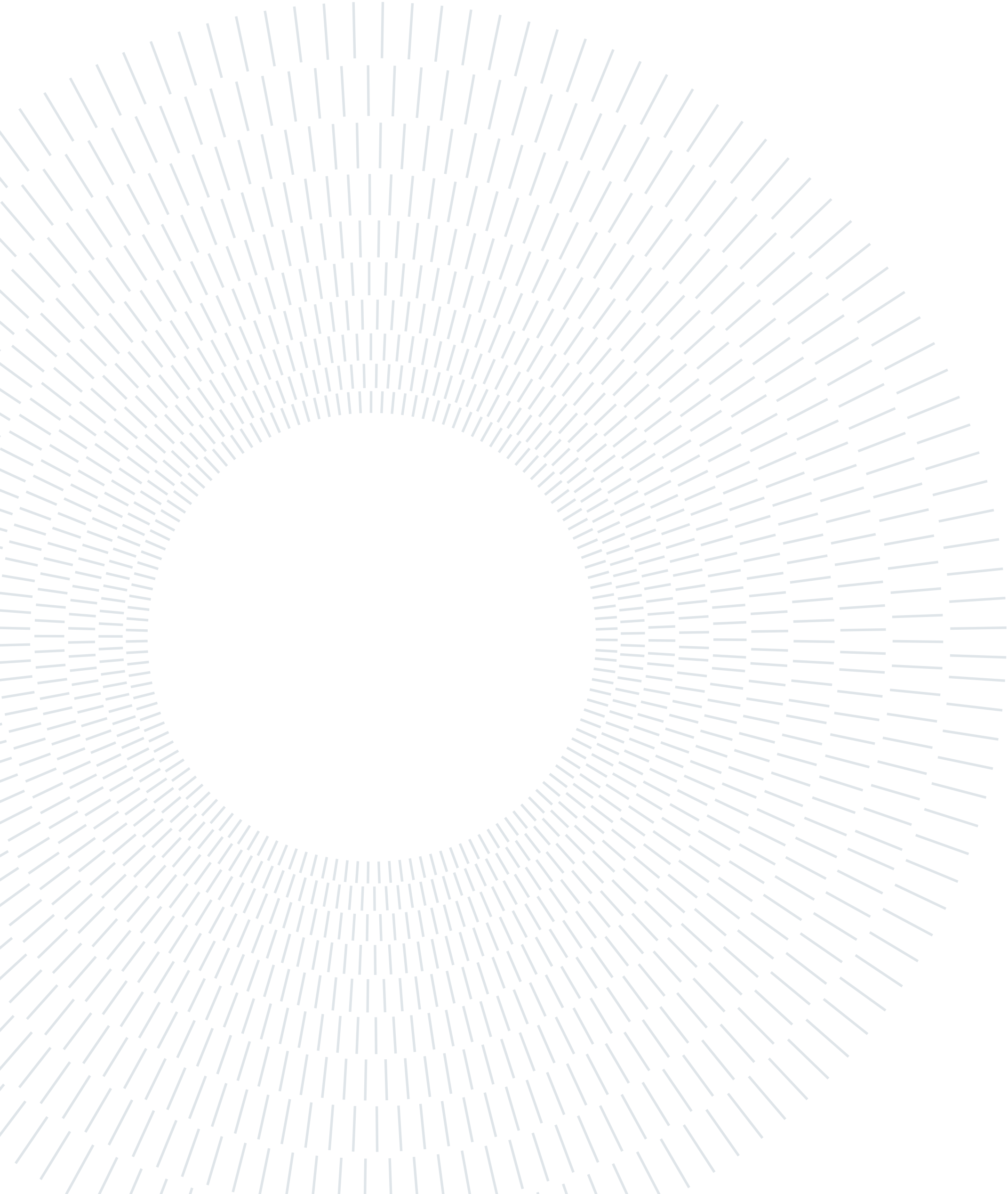

Contents

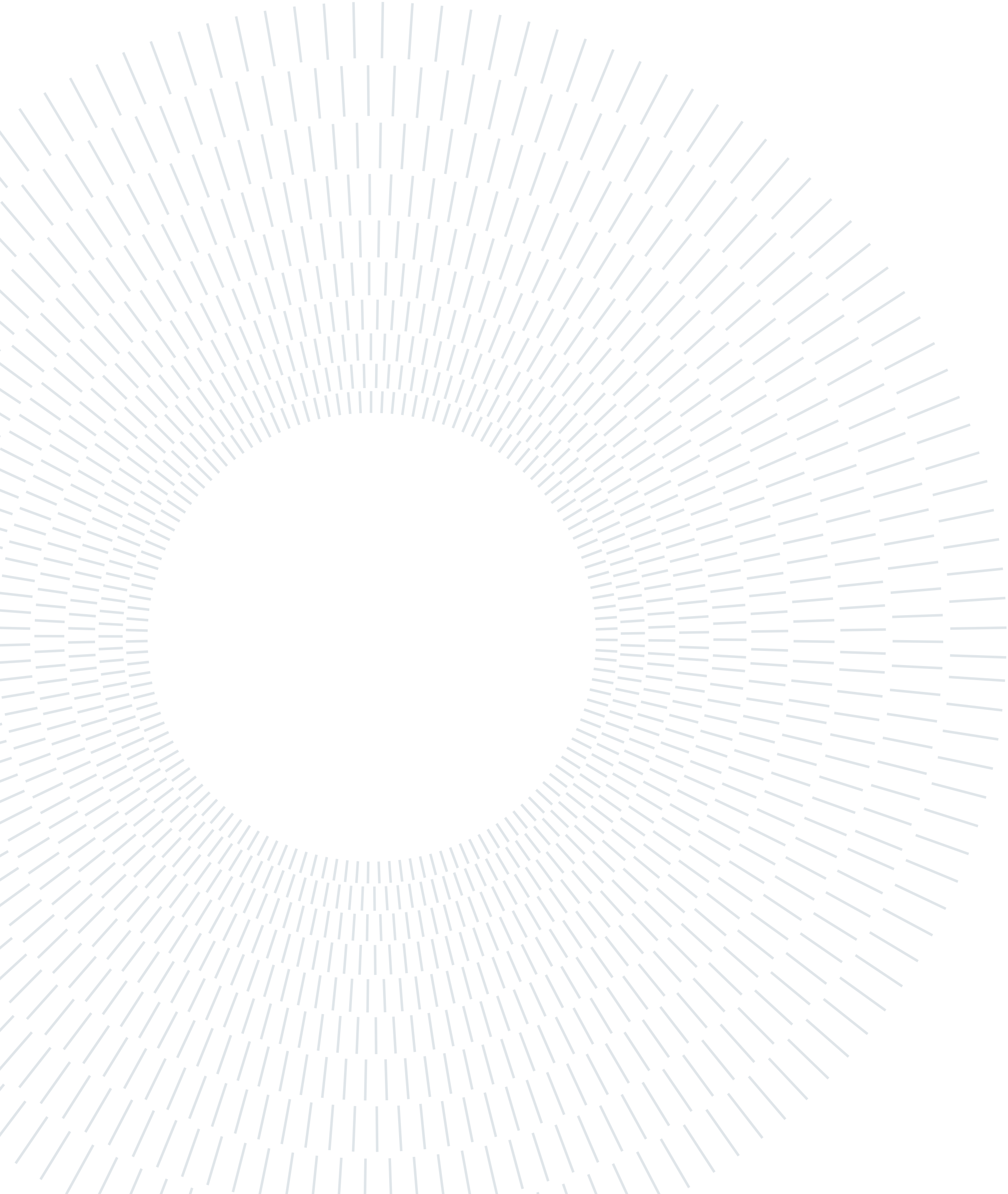

L'importante non è stabilire se uno ha paura o meno,
è saper convivere con la propria paura e non farsi condizionare dalla stessa.
Ecco, il coraggio è questo,
altrimenti non è più coraggio, è incoscienza.

Giovanni Falcone, 1988

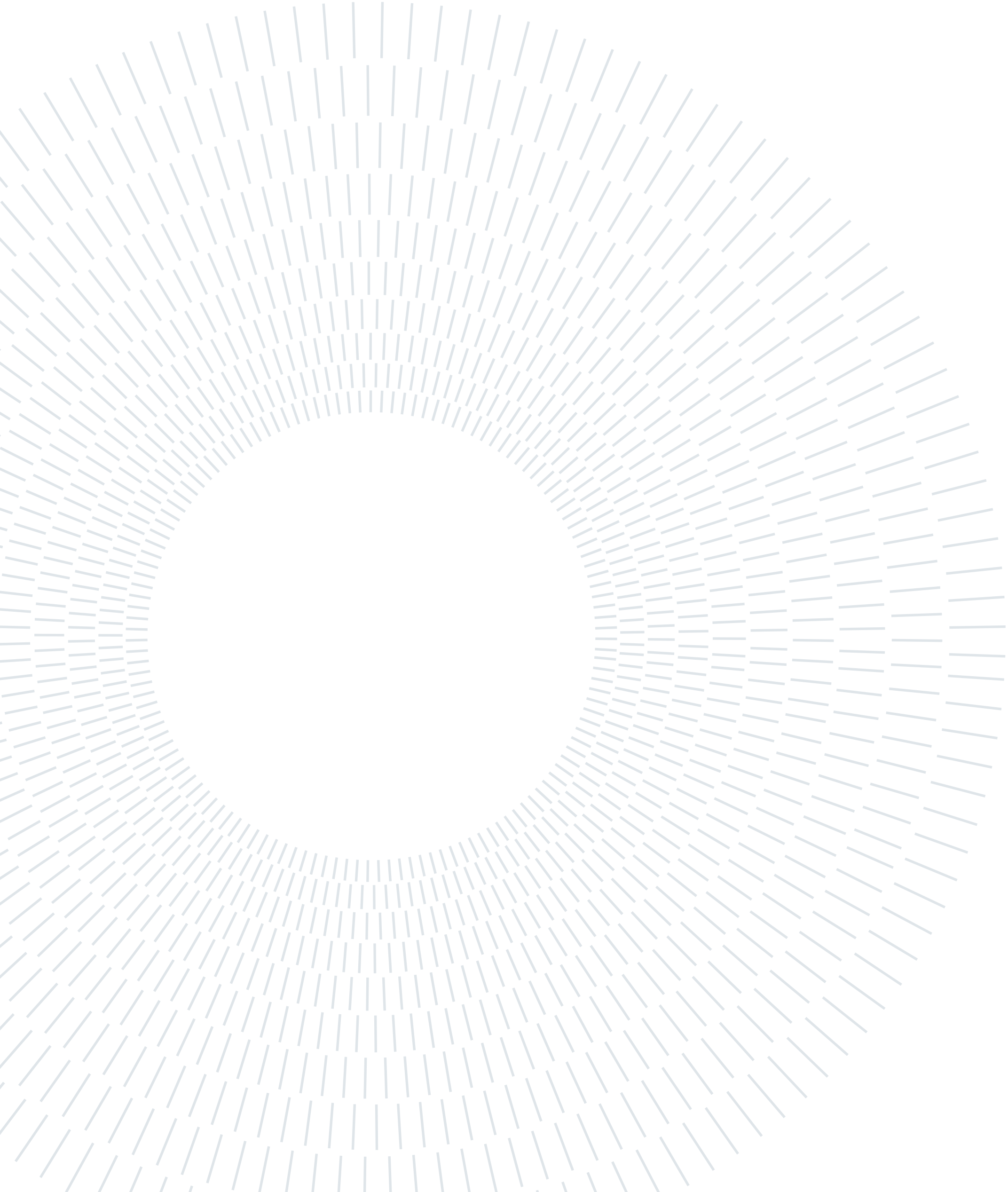

Introduction

4 pm, 8 April, 1911, Leiden. *"practically zero"*. These words marked the beginning of one of the most intriguing branch of human knowledge. Superconductivity, the phenomenon the Dutch physicist observed that Saturday afternoon of more than 110 years ago, was something no one had never experienced before and, most importantly, no one was expecting to occur. It was the collateral effect, a fortunate turn of events, of a scientific dispute about the behaviour of matter, conductors in particular, at very low temperatures, where the Kelvin scale proves more practical than the Centigrade.

Superconductivity, during the years, has been able to emerge as a technology, contributing to advances in a wide variety of sectors. From medicine, where it is iconic the example of the high-resolution MRI machines, technical prodigies which make use of superconducting magnets, to transportation with levitating bullet trains, passing through electronics, astronomy and high-energy physics.

In some regards, superconductivity is very simple to be explained. Some materials, they could be metals or even some strange oxide composites, have the ability to oppose no resistance to the flow of current crossing them. The only condition we are required to comply with is to cool them down below what is called their critical temperature. Or, at least, this is what the first pioneers believed. The reality turned out to be more complicated than we expected at the beginning. We discovered that the absence of electrical resistivity is not even the defining property of a superconductor, which is rather the Meissner effect, the expulsion of a magnetic field when it is cooled below the critical temperature. This perfect diamagnetism automatically implies the perfect conductibility of those materials. A perfect conductor is characterized by

$$\dot{\boldsymbol{B}} = 0 \ , \tag{1}$$

that is, the flux density at every point within the material does not change with time and hence, it has to remain "frozen" at the condition it was when it became resistanceless. To better understand the phenomenon and the difference between a "simple" perfect conductor and a proper superconductor, it will be useful Figure 1. The right side shows the behaviour of a perfect conductor in two different situations. In the first, it is cooled

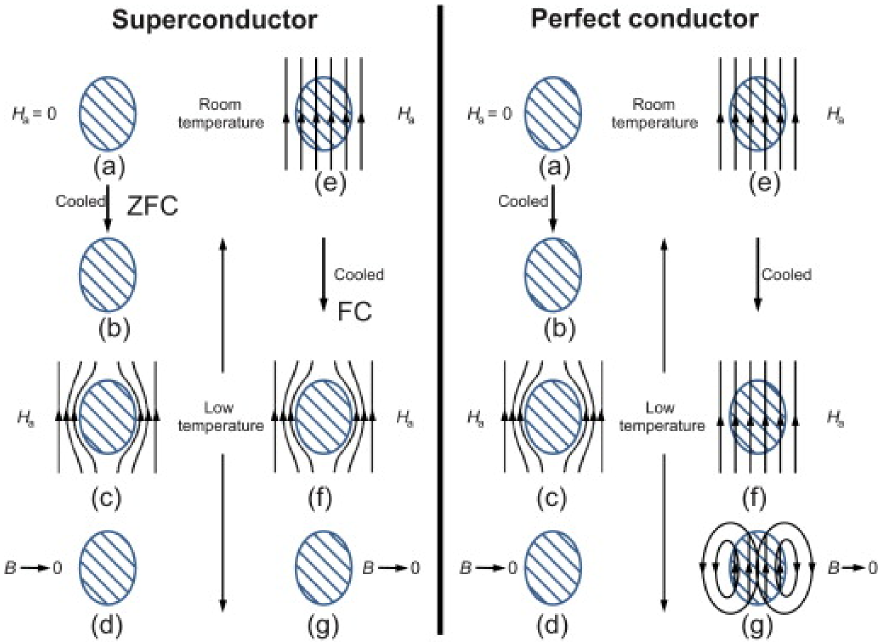

Figure 1: Difference between a perfect conductor and a superconductor [34].

and becomes a perfect conductor when no magnetic field is applied (b). When the magnetic field is finally applied, because of Equation (2), it cannot penetrate (c). Resistanceless superficial screening currents are induced in such a way to perfectly oppose and cancel the magnetic field within the domain. If the magnetic field is now turned off (d), the system simply returns to the initial condition (a). So far, the superconductor has the same behaviour. Something interesting, however, happens when the magnetic field is applied before the two materials undergo the respective transitions. For the perfect conductor nothing special happens from (e) to (f), but when the magnetic field is reduced to zero, persistent currents are generated to maintain the flux density inside unchanged. The result is that the perfect conductor is left permanently magnetized (g). What Meissner and Ochsenfeld discovered in 1933 is that, reproducing the same experiment on a superconductor, the result changes. If the magnetic field is applied above the transition, once the specimen becomes superconducting, it completely expels the field. A superconductor never allows a magnetic field within its domain, and rather than Eq (2), it follows [1]

$$\boldsymbol{B} = 0 \, . \tag{2}$$

The extraordinary ability of superconductors to transport vast amounts of electric current without any resistance is exploited, among other applications, in the design and construction of magnets for high-energy physics. Over the years, no other branch of science has grown to be more dependant upon superconductivity than this field. Physicists seek for magnets which provide increasingly higher and higher fields, to accelerate more, and more tightly, bunches of particles with the hope of unraveling the intricate mysteries of the Universe. This is also the scope of the Muon Collider, one of the possible candidates for the next generation of particle accelerators. This collider, differently from any other machines ever built, will accelerate unstable particles, muons. Muons share the same properties as electrons, except they are 200 times heavier and they decay into an electron and two neutrinos in 2.2 μs . This peculiar behaviour makes the Muon Collider design a challenge and potentially poses an even greater obstacle to its practical implementation. This is particularly true for the subject of this thesis work, the solenoids of the 6D Cooling stage of the Muon Collider, which present several technical and design barriers, but they also represent the opportunity to make a small leap ahead in the knowledge of the working principles of Nature and, maybe, the solutions that are going to be found will be used to advance the technological progress, in a way that, as usual, is beyond our current imagination.

This work consists of six chapters.
Chapter 1 offers an historical introduction. It starts from the premises which led to the discovery of superconductivity, arriving to the first evidence of the phenomenon by Kamerlingh Onnes in 1911 and the breakthrough of the high temperatures superconductors (HTS) in 1986.
Chapter 2 explores the most important theories and explanations on how superconductors work. At first, the phenomenological theories of London and the two-fluid model are presented. Then, before giving some practical insights on HTS, also a glimpse of the newer quantum theories is given.
In Chapter 3, the Muon Collider project is presented in detail, providing an overview of its key aspects and components, with a particular focus on the 6D Cooling stage.
Chapter 4 encompasses the methods employed and the results obtained in the characterization of the 2954 solenoids that constitute the 12 stages of the cooling process.
In Chapter 5, a comprehensive analysis of the quench protection aspect is conducted, accompanied by a detailed description of the implemented 1D FEM quench simulation and its corresponding results.
Chapter 6 serves as the conclusion of this thesis work, providing a summary of the key findings and insights and offers an exploration of the future prospects and potential directions for further research in the field.

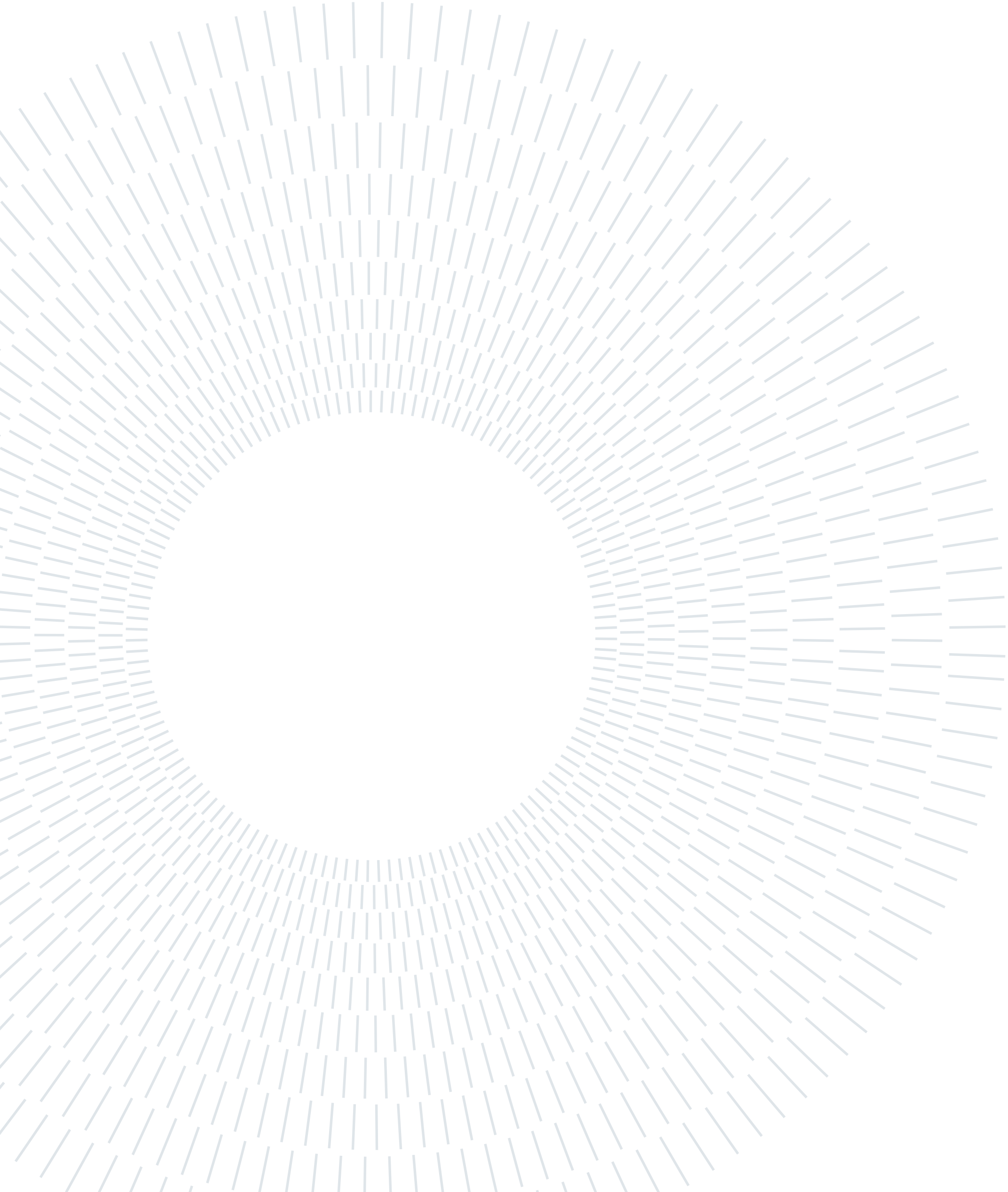

1 | The Discovery

Before starting with a physical explanation of what superconductivity is, I think it is worth going through the story of this extraordinary discovery. This story, like many others in science, is made up of plenty of failures, some wrong paths, but fortunately, also of perseverance and a good dose of luck.

No one was looking for it, but most importantly, no one was expecting it.

The story of the discovery of *superconductivity* is inexorably linked to the technological advances in the field of cryogenics, but also to the scientific progress of the concept of electrical resistivity. We can identify at least three different historical stages: the discovery itself, the development of the technology and then the breakthrough of the so called high–temperature superconductivity.

1.1. The Early History of Cryogenics

We cannot talk about superconductivity without first saying something about cryogenics, the science of refrigeration at very low temperatures. As said in the introduction, these two stories are extremely linked. Nowadays, we take refrigeration for granted but this was not the case in the Nineteenth Century. In those days, many scientists fought to reach, step by step, the bottom of the absolute scale of temperature, the coveted 0 K.

The general idea behind refrigeration is the use of the cooling action of a previously compressed gas when it is allowed to expand. When a sufficient number of compression and expansion cycles are performed, it may be possible to reduce the temperature enough to liquefy a gas. Now that we have a liquefied gas at a very low temperature, we can use it as a thermal bath for cooling down any object we want. Different gases have different boiling temperatures and hence can provide a different cooling effect [31].

The very first trials in this direction were made by the Dutch chemist Martinus van Marum who liquefied ammonia in 1769 and some years later, in 1823, the English scientist Michael Faraday succeeded in liquefying also chlorine [32]. There is a communication of Sir. Humphry Davy, a colleague of Faraday, to the Royal Society in which he explained the method to obtain such condensed gases. It consisted in placing them in one leg of a bent sealed tube confined by mercury, and applying heat to ether in the other end. The increase in pressure was able alone to liquefy high boiling temperature gases like sulphurous acid and hydrogen cyanide. On a side note, Davy, at the end of the paper wrote: "*There can be little doubt that these general facts of the condensation of the gases will have many practical applications*"[16]. He was referring to the potential industrial applications of this new technology in refrigeration of food and beyond. Nowadays, we know that its impact did not stop there [15].

One of the first true achievements in this field was accomplished by Micheal Faraday himself in 1845. He was able to liquefy carbon dioxide, reaching 195 K(-78 °C). From that time forward, the limit was lowered more and more. In 1877, Raoul Pictet and Louis Cailletet independently liquefied oxygen (90 K) and nitrogen (77 K). They used two different methods. Pictet's one consisted in a series of stages in which a different gas was liquefied by exploiting the corresponding thermodynamic properties of the preceding stage. Instead, Cailletet's approach was based on three consecutive stages: high compression, then a mild cooling, and finally a sudden decrease in pressure [32].

Many other gases were liquefied but eventually just two *permanent gases* (those existing only as gas on Earth) were missing: hydrogen and helium. Not by chance they are the two with the lower liquefaction temperatures, respectively 20 K and 4 K. The task was made difficult by two factors. The first factor, which it will tackled in few lines, is obtaining a

Boiling temperature of cryogenics fluids

	Boiling point [K]	Boiling point [°C]
Helium–3	3.19	-269.96
Helium–4	4.21	-268.94
Hydrogen	20.27	-252.88
Neon	27.09	-246.06
Nitrogen	77.09	-196.06
Air	78.80	-194.35
Fluorine	85.24	-187.91
Argon	87.24	-185.91
Oxygen	90.18	-182.97
Methane	111.70	-161.45

Table 1.1: Cryogenic fluids with their boiling point in kelvins and degree Celsius [46]

sufficient amount of gas to be processed. The second factor is the challenge of storing the gas for a reasonable amount of time without it evaporating. The turning point was provided by James Dewar in 1892. He invented a very effective insulated vessel that is now commonly known as a Dewar or a thermos. It was a double wall silver-coated glass vessel in which a vacuum was created in between the two walls [31]. This kind of configuration allowed an incredibly high insulation from the external ambient and was what scientists needed to transport and make use of the liquefied gases.

Dewar did not just invent the thermos but also was the first to liquefy hydrogen. His *modus operandi* was extremely practical. Throughout his entire career he never wrote any theoretical work.

On May 10, 1898 he succeeded in liquefying a small specimen of hydrogen using the so called Joule–Thomson effect. This effect involves the temperature change of a *real* gas when its pressure is changed and no heat is exchanged with the environment [47]. This process is described by:

$$\mu_{JT} = \left(\frac{\partial T}{\partial P}\right)_H = \frac{V}{C_p}(\alpha T - 1) \tag{1.1}$$

As it is clear in Eq (1.1), if μ_{JT} is positive (see Figure 1.1), as it is for temperature under ambient temperature, and ∂P for an expansion is always negative, then ∂T has to be also negative. This means that the gas is going to cool down while expanding.

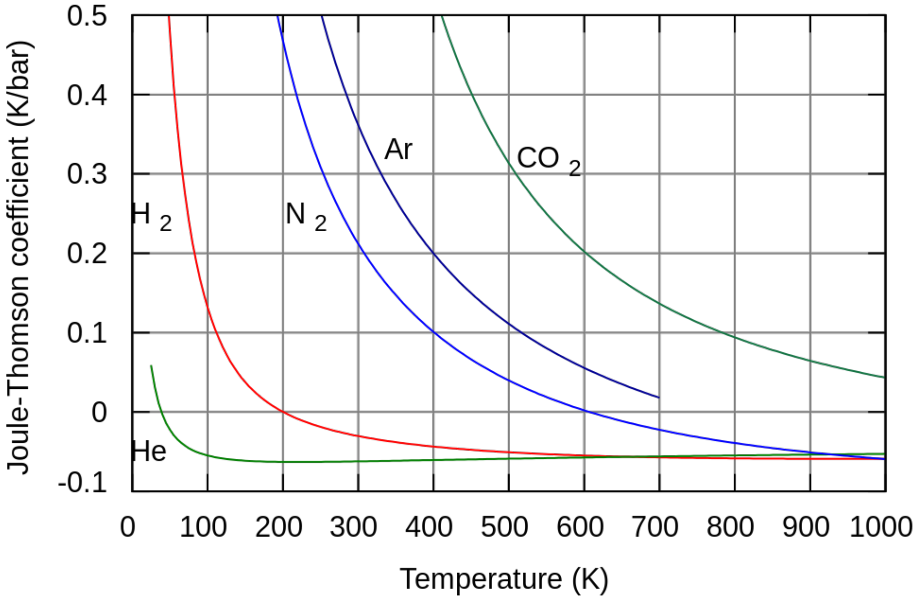

Figure 1.1: Joule–Thomson coefficients for various gases at atmospheric pressure [19]

Regarding Dewar, he also claimed to have liquefied helium along with hydrogen, believing that the two gases had the same boiling point. It turned out that what he thought was liquid helium were just impurities. The real liquefaction of helium was due to the protagonist of all the story, Kamerlingh Onnes (Fig 1.2). Onnes was a meteorologist at the University of Leiden and had a very different approach to science with respect to his "rival" Dewar [32]. His focus was on how low temperatures influence the properties of matter and his work had the theories of his friend Johannes Diderik van der Waals as a guide. Onnes's laboratory was equipped with a state–of–the–art apparatus, which enabled him to achieve his main goals: the measurement of some volumetric properties of different substances over a large range of temperatures and the systematic production of very pure liquefied gases to be used in his experiments. The process that was used was very similar to the one already used by Pictet. Each cycle had as circulating fluid a different gas, methyl chloride, ethylene, oxygen and air. However, this scheme was not able to liquefy hydrogen because its condensation temperature was far below the minimum one reachable. The solution was found using the so–called Linde scheme. This scheme made use of a regenerative cooling system [48]. By 1906 he was able not only to liquefy hydrogen but also, and most importantly, to produce it in reasonable quantity. The next goal was helium.

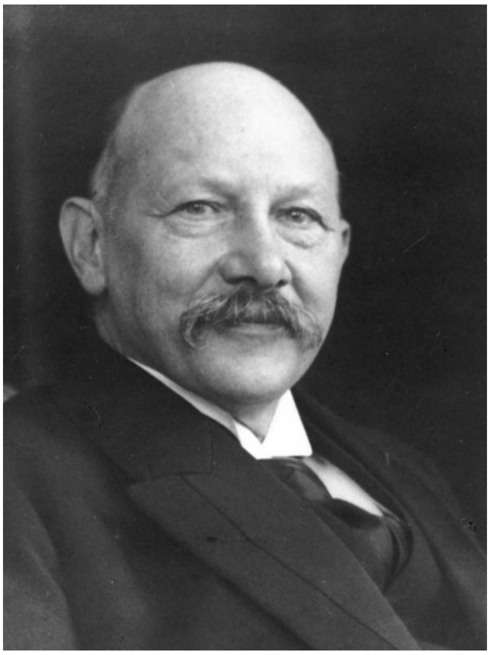

Figure 1.2: Portrait of Heike Kamerlingh Onnes [28]

Helium was discovered in 1895 and found to be produced as a daughter in the decay chain of uranium. Because of that it can be found in some minerals on Earth but, in those days, the extraction was very complicated and limited to small quantities. Many scientists attempted to liquefy the newly discovered gas, but they all eventually failed.

Aside from the technical difficulties mentioned earlier, one of the biggest problems was its scarcity. Here the good luck and the remarkable diplomatic skills of Onnes came into play. The first attempt of getting a helium supply led Onnes to the small English city of Bath. There was a problem: that same supply had already been requested and used by Dewar. *"We both want the same material in quantity from the same place at the same time and the supply is not sufficient to meet our great demands"* [32]. This was Dewar's reply to Onnes request of sharing the supply. However, Onnes did not lose heart and found out that helium could be extracted also from monazite sand. In those days the monazite was mined in North Carolina for other uses. Exploiting the help of his younger brother, who was the Director of the Office of Commercial Intelligence in Amsterdam, he was able to obtain a large supply at favourable conditions [31]. He now had the helium, the following step was to purify it. Although not yet liquefied, the data obtained at low temperatures allowed him to obtain helium isotherms. Using these and again the theory of van der Waals he was able to predict a boiling temperature at about 5 K. Finally on July 10, 1908, Onnes succeeded in liquefying some tens of cubic centimeters of helium. Initially, Onnes and his colleagues did not even realize this. Someone outside his team noticed that the bottom of the vessel, the part that should have contained the liquid, was not illuminated enough. The helium surface tension is indeed very low and it is challenging to observe a net interface between the liquid and the gaseous phases. In that day Onnes was not only the first to liquefy helium but also achieved the lowest temperature measurement ever recorded. Over the next couple of years, Onnes attempted to go even further. He tried to obtain solid helium but he did not succeed, despite reaching temperatures as low as 1 K. Now we know that it is impossible to solidify helium unless applying enormous pressure. Wisely, he decided to embark on a different sector: the electrical resistivity of metals as a function of temperature [31].

1.2. The Early History of Electrical Conductivity

As the temperature bar was set lower, scientists needed to advance their thermometric apparatus to measure it accurately. In particular, since the second half of the Nineteenth century, there has been increasing interest in the field of the electrical conductivity of metals and its dependence on temperature.

In this section the focus will be the evolution of the concept of electrical resistivity. Nowadays we consider the different electrical properties between conductors and insulators as something obvious.However, it was not obvious at all in the Eighteenth century. In 1720 Stephen Gray, a British scientist, proved that electricity could be conducted only by specific materials [33]. Later on, Benjamin Franklin suggested the now famous distinction between a conductor and an insulator.

The first attempt to study the electrical conductivity of different metals is credited to the British natural philosopher Joseph Priestley. He let equal length and diameter wires be passed by electrical discharge and measured the amount of melted metal. Although inaccurate, Joseph Priestley's results led Henry Cavendish to speculate about a possible relation between temperature and conductivity. It was only in 1821, thanks to the aforementioned Humphry Davy, that new and more reliable results were obtained. In particular, he found out that the electrical conductivity decreases with an inverse law as temperature increases. In 1826, Antoine Becquerel wrote an article on the *Annales de chimie et de physique* in which he provided a list with the electrical conductivity (in that time referred as conductive power) of different metals. The first analytical expression regarding the phenomenon was assessed by the Russian physicist Emil Khristianovich Lenz. He wrote the following law

$$\gamma_n = x + yn + zn^2, \tag{1.2}$$

where n is the temperature, γ_n the electrical conductivity at n and x, y and z are particular coefficients for each specific substance [33].

Some years later, without mentioning Lenz's work, Alexandre–Edmond Becquerel (the third son of A.C Becquerel) improved it in terms of accuracy. He concluded that the rate of change of the conductivity with respect to temperature is constant, which, expressed in a mathematical form is

$$\frac{dR}{dT} = const, \tag{1.3}$$

or, more explicitly

$$R = R_0(1 + aT), \tag{1.4}$$

where R_0 is the resistance at 0 °C and a is again a coefficient [33]. Another contribution was made by the British chemist Augustus Matthiessen. Initially, he concentrated on the different conductivities of various metals and alloys. In particular, he divided metals in two groups: the first included those metals which, once alloyed with each other, yielded a conductivity in the ratio of their relative volumes. The second group was composed of metals that did not exhibit this property [33]. Essentially, Matthiessen confirmed Lenz's formula but with a notable addition. He stated that the discrepancy between the observed and the calculated resistances of an alloy is a constant value throughout all the temperatures in the range of validity of the formula (0 °C to 100 °C).

It is in this stage that the studies on cryogenics described in Section 1.1 came into play. For example, Cailletet (already mentioned in Section 1.1 as the one who liquefied oxygen) measured the conductivity of some metals in the range from -123 to 0 °C. The conclusion drawn from this and similar studies was the fairness of the predicted behaviour of the conductivity at decreasing temperature: a proportional increase. It is not difficult to think that from this time on a lot of studies were performed to verify whether the linear trend would have been respected also at lower temperatures. In particular, one of the most important topic of discussion was the inferred behaviour near and at 0 K.

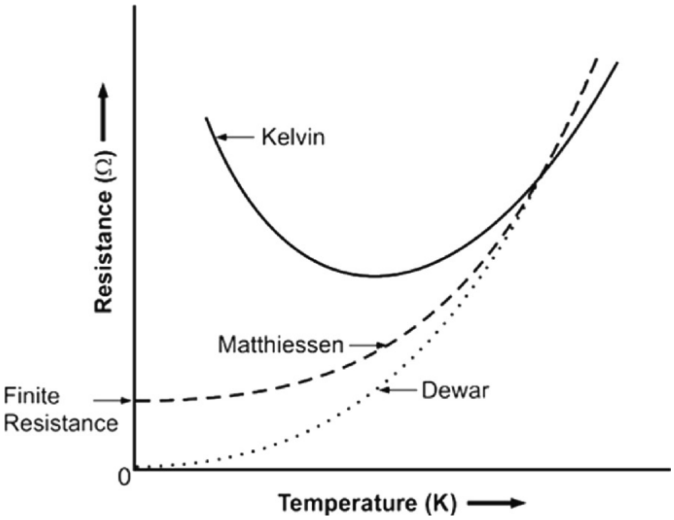

Figure 1.3: Qualitative trends for resistivity near absolute zero [38].

As it is shown by Figure 1.3, there were three different predictions of the behaviour of the metals resistivity.

At the beginning of the Twentieth Century, the Drude model was a popular explanation for the transport properties of different materials, particularly metals. Its main idea was that the electrons were responsible for the transport of the electric charge and in doing that, they were described as a moving gas. The fact that no crystal has an infinite conductivity is due to collisions: when an electron undergoes a collision with an ion of the lattice its motion is perturbed. It can be completely stopped or the direction of its velocity can be changed. In any case the transport of the charges gets worse and this can be seen macroscopically as an increase of resistivity. Starting from this idea, as said before, three different visions took place. They all had in common the linear decrease caused by the reduction of the thermal agitation of the ions.

Dewar's vision was that at 0 K the thermal agitation of the lattice positions would drop to zero, and as a result, so would the resistivity. Instead, Lord Kelvin's idea was that the resistivity should have a minimum. Below the minimum, he thought that the electrons would stick to their parent ions causing the end of the charge transport and the increase up to infinity of resistivity. In the middle between the two there was the Matthiessen model. He believed that resistivity was determined by two different causes: thermal agitation at higher temperatures and collision with defects at lower ones. The second contribution is constant and depends on the level of impurities present in the crystal. The result was a plateau at the beginning of the temperature scale.

Several experiments tried to settle the debate. It was clear since the beginning that Kelvin's proposal was not correct at all, while some doubts remained for the other two. At the beginning of December, 1910, Onnes and two collaborators, Cornelis Dorsman and Gilles Holst, set a series of new measurements based on more sophisticated techniques. They studied the resistances of gold and platinum at very low temperatures and observed no such behaviours like those predicted by Kelvin or by Dewar. Instead, at least down to the temperatures that Onnes's helium apparatus was able to reach, the Matthiessen's rule was the one that showed more accordance with experimental data [31]. The temperature of the first experiment which involved a platinum resistor was of 1.1 K. The results showed that below 4.2 K the curve began to flatten out. The resistivity had dropped to a residual value which, according to Matthiessen's idea, was related to the purity of the sample.

1.3. The Discovery of Superconductivity

If the residual value of the resistivity was due to impurities in the sample, as the series of experiments were showing, then it was logical to try to verify whether, reducing them down the lowest possible value, the resistivity would also drop to zero. This was indeed what Onnes tried to do. However, he discarded both platinum and gold in favour of mercury. There were at least two good reasons for this choice. The first was related to the know-how of the Leiden laboratory in the purification of the metal while the second one was due to the intrinsic ease with which mercury could be distilled to surprising purity. Meanwhile some updates were performed on the cryogenics apparatus. The most important one involved the addition of a separated helium cryostat where experiments could be easily performed. The new cryostat was connected to the liquefier by a brand–new double–walled, vacuum–pumped glass siphon [41].

An experiment to test the transfer of liquid helium from the liquefier to the cryostat was set on April 8, 1911. According to Onnes's notebook, the mercury resistor was put in place, hoping for a successful test [41]. The experiment started early in the morning. At first, the team took the data regarding the linear decrease of the resistivity down to a temperature of 4.3 K. At this point they started to reduce the mercury vapour pressure thus reducing the temperature of the liquid phase. The sample reached 3 K. In the afternoon, at 4 pm, the resistivity was checked again: *"practically zero"* [41]. This was not the only strange result obtained that afternoon.

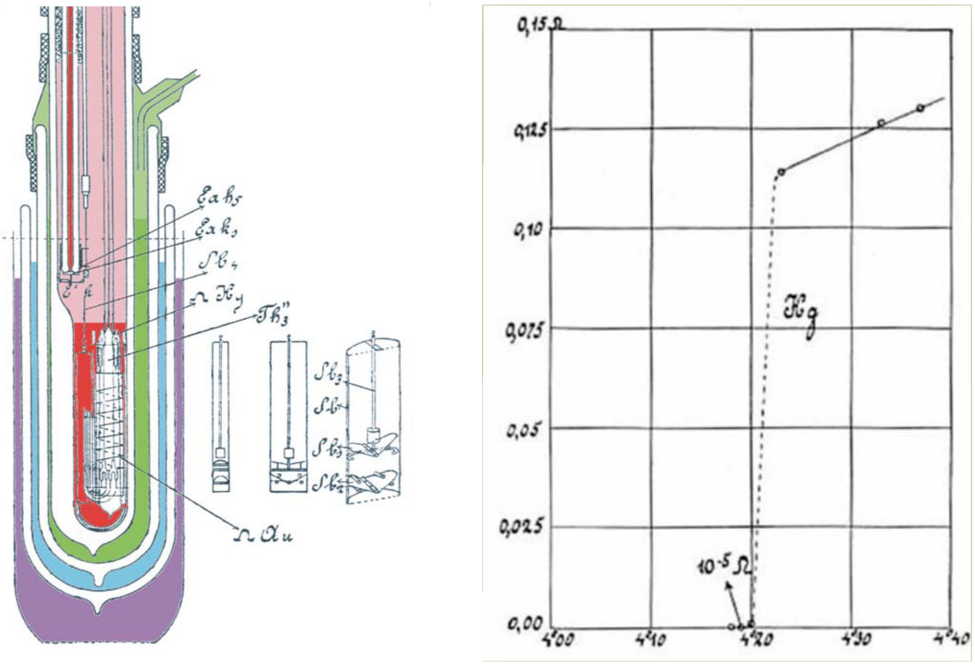

(a) Bottom of the cryostat. (b) Onnes's plot of mercury resistivity.

Figure 1.4: Images taken from Reference [41].

In fact the experiment went on almost all day long. At the end Onnes reported a strange behaviour of helium around 2 K. At that temperature the measurement was made difficult by a particularly high surface evaporation rate. Now we know that in that day, Onnes's team not only observed *superconductivity* but also helium *superfluid* transition. However, Onnes and his group still did not realize what they were facing. In fact, three weeks later Onnes reported to the Dutch Science Academy that the experimental data he got was in line with his model expectations: because the sample he was using was ultra–pure mercury, its resistivity should have been linearly decreasing with temperature down to 4.3 K and then become zero.

The definitive and most enlightening experiment was performed on 23 May. The voltage resolution had been greatly improved to 30 nV but most importantly a new strategy was defined. Indeed, for helium stability reasons, the measurements were taken starting from a lower temperature up to an higher one. The result was clear: "At 4.00 [K] not yet anything to notice of rising resistance. At 4.05 [K] not yet either. At 4.12 [K] resistance begins to appear" [41].

After a summer spent looking for short–circuits or some other malfunctions, finally in October of the same year he surrendered to the experimental evidence. Some new phenomenon was occurring under his eyes. Onnes decided to call it *supraconductivity*. A paper published in November contained the famous and historical plot showed in Figure

1.4b. The brand–new result was announced in the first of the Solvay Conferences in front of the most important scientific figures of the century.

In the following months the team did not stop there and eventually came up with three new results. First, they discovered that, to Onnes's disappointment, it was not mandatory for mercury to be ultra–pure and some impurities still allowed it to superconduct. Then they found out that also lead and tin exhibited the same phenomenon at, respectively, 6 K and 4 K. Lastly, in 1914 Onnes discovered the detrimental effect of the magnetic field on superconductivity. The critical field, the magnetic field that a superconductor can sustain at a specific temperature, of lead at 4.25 K was just 600 gauss or 0.06 T. That must have been a great disappointment for Onnes, burying his dream of superconducting coils able to produce fields as high as 10 T [41].

1.4. The Discovery of HTS

In 1964 James Schooley and his team discovered that strontium titanate could superconduct if cooled down to 0.7 K [31]. Why was the discovery of such a low performance superconductor so important? Because strontium titanate is an oxide and we did not expect an oxide to superconduct.

After the discovery of superconductivity two main paths were being followed in those years. The first one was the most logical: the race toward the theoretical explanation of the process. We shall see in the next chapter some steps in this direction. Next, there was the forbidden dream of a few scientists around the World: superconductivity at high temperature. In this case high temperature is a relative concept and means temperatures higher than the bottom of the Kelvin scale. From the initial 4 K set by Onnes the record crept upward a few degrees and a few years at a time, up to 23 K, which seemed to be a sort of insurmountable limit. This same limit led to a progressively decreasing interest from the industry for commercial applications (like magnet construction) and most importantly led the vast majority of the scientists who dedicated their life to the search for new materials to abandon the race. Many researchers thought that not only substantial advances were unlikely but maybe even physically impossible. The credibility of the high temperature dream was not only undermined by poor results but also by false claims of scientists maybe too hasty in announcing new breakthroughs. In 1973, David Johnson discovered that lithium titanate, another oxide, also superconducts. This time the critical temperature was 13 K, which could easily hold its own against those of metallic superconductors. Despite this discovery and some others, oxide superconductors struggled to establish themselves as prime candidates for high temperature superconductivity.

However, two researchers at the IBM Zurich Laboratories had different ideas with respect to all other scientists. The older of the two, Karl Müller, was a physics professor at the University of Zurich and an IBM senior employee, and he could work on just about whatever he wanted in the lab [20]. Georg Bednorz, instead, worked for Müller only after having carried out all his other duties.

In 1985 Bednorz was fascinated by some papers on copper oxides which had been synthesized by Claude Michel at Caen University. These oxides exhibited unusual metal–like electrical conductivity at room temperature, but had never been tested at low temperatures to investigate their possible superconducting properties. First, Bednorz tested the compound and found it to be a superconductor. Finally, on January 27, 1986, they discovered that a variant of the Michel material, a composite made of barium, lanthanum, copper and oxygen, superconducted at the astonishing temperature of 30 K. Because of the abundance of false claims in this field, they repeated the experiment several times before they were absolutely convinced about its results. Eventually, in mid April, they wrote a paper with the cautious headline: "*Possible high–T_c superconductivity in the Ba–La–Cu–O system*" [7].

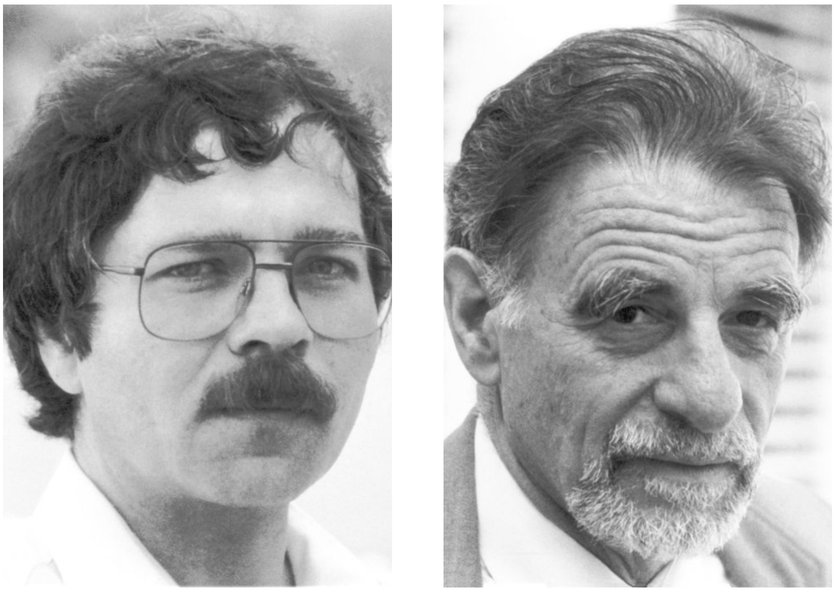

(a) George Bednorz.

(b) Alex Müller.

Figure 1.5: Johannes Georg Bednorz (left) and Karl Alex Müller (right), winners of the Nobel Prize in Physics in 1987 for the discovery of high-temperature superconductors. Images taken from [3].

After few months of review, on November 6, 1986, the paper arrived on Paul Chu's desk. Chu was born in China in 1941 and grew up during a tumultuous time in Chinese history. His family suffered greatly during the Chinese Civil War and the subsequent Communist takeover, leading to financial difficulties. Despite these challenges, Chu excelled academically and earned a scholarship to study in the United States, where he earned his PhD in physics from the University of California. Throughout his academic career, he passionately dedicated himself to the study of superconductors. He delved into their behavior under high pressure, and later, tirelessly searched for high-temperature superconductivity. When his faith was on the brink of fading and the morale of his team was at its lowest, the news from the Zurich lab burst forth like a divine calling, making everything brighter. He knew that the Zurich compound was the right path to follow, the key to unlocking the mystery he had been grappling with for so long, and he ordered his team to stop everything they were doing to concentrate full–time to it.

Today, as then, there are four steps to confirm the existence of a new superconductor. The first one is to obtain a sample using a specific synthesis process: mixing chemical elements in carefully controlled ratios and baking them with the correct temperature, atmosphere, heating and cooling rate. Once the sample has been created there are three subsequent characterization steps. Firstly, the critical temperature needs to be measured. Sometimes, the usual drop in resistance can be misleading because it can be produced by some faulty connections or short circuits. A first way to exclude any of these effects is to measure the decreasing of T_c as an external magnetic field is applied. The definitive proof and the third step of the process is the demonstration of the Meissner effect. Not only this test is essential but is also very useful in those cases (the vast majority, actually) in which the percentage of the superconducting phase with respect to the whole sample is so small that the peculiar resistivity drop cannot even be seen. The fourth and last step is the isolation, identification and characterization of the superconducting phase [20].

In their paper, Bednorz and Müller reported the achievement of just the first two steps. They didn't have the equipment to test neither the Meissner effect nor the real composition of what they had obtained. They were just convinced that out of the three phases they synthesized only one was the substance of interest. Paul Chu and his team agreed to start trying to reproduce the Zurich results first. Bednorz and Müller used a particular technique to obtain the compound called coprecipitation. Lanthanum, barium and copper are dissolved in a solution and then let to precipitate together. The resulting gelatin–like material is then baked at high temperature. In contrast, Chu's laboratory was specialized in the so–called solid–state synthesis in which dry–powdered chemicals are mixed, ground and baked. Chu's group, at this stage, had to make an important decision. The most logical one would have been to use the same technique as that used by the original paper but it was harder to reproduce and would have required time to be mastered. From the other side, the solid–state synthesis was simpler, already known by the group, but at the same time it was more risky because it wasn't the process used by the IBM researchers. There was no guarantee that the same compound could be obtained. At the end the choice was made directly by Chu: the solid–state synthesis should have been given at least a chance. Only few days had passed by and the group had already achieved its first successes. The electrical resistivity of the obtained compound dropped at 30 K, the same temperature of Bednorz and Müller. In the next couple of weeks the team continuously produced more and more samples and eventually improved the technique. With a more reproducible process, the team began to modify the original recipe. Instead of using a 4:1:5 ratio of lanthanum, barium, and copper, they discovered that using a smaller proportion of copper yielded better results. Interestingly, just one of those specimens exhibited something incredible. A sharp and clear superconducting transition at 73 K. Unfortunately that result was never achieved again: the next day something unknown must have happened to the sample because all signs of superconductivity were gone. The subsequent stage involved the use of a technique called X-ray powder diffraction to investigate the actual composition of the specimens. The task was delegated to Ken Forster, a doctoral student who was a member of Simon Moss's team (Chu's colleague in the same university). In a few days he got the same results obtained by Bednorz and Müller. The "apparently superconducting phase" [7] was due to a layer–type perovskite–like phase related to the K_2NiF_4.

The following development in the story is when Chu's distinct thinking approach came into play. He was an authority in the field of extremely high–pressure measurements of the critical temperature of a superconductor. The critical temperature T_c can be a function of pressure: in some cases it can slightly decrease, in others it slightly increases. When the measurement was performed the outcome was beyond all expectations: the resistance drop occurred at 40 K. Not only was this a world record but it also meant that there was a possibility of increasing T_c at room pressure provided that the chemical composition of the compound was changed to smaller atoms (to mimic the squeezing effect of high–pressure [20]). The natural choice was the exchange of barium with strontium. Strontium belongs to the second group of the periodic table of elements so it is an alkaline earth metal like barium, but it is slightly smaller. A new 2:1:4 compound was created ($(La,Sr)_2CuO_4$) and measured to superconduct at 39 K, at room–pressure. In the meanwhile several other laboratories tried the same change (barium and strontium, being in the same chemical group, behave very similar and the exchange seemed natural to everyone) and obtained similar results. Also calcium was tested (another alkaline) but the results were considerably worse. By the end of December Chu's team synthesized a sample of $La_{1.8}Ba_{0.2}CuO_4$ which had a reproducible high–pressure critical temperature of almost 50 K. Even if this temperature set another world record, the team's attention was once again focused on the fleeting glimpse of 70 K signals [20]. Chu was convinced that the reason behind these signals was not related to a 2:1:4 compound. In fact, only "dirty" samples seemed to show signs of considerably higher T_c.

There were clear elements to believe that in the original Bednorz and Müller compound, copper could not be substituted by any other metal because of its particular electronic structure, which seemed to be a key for superconductivity and the only element left to be altered was lanthanum. Chu selected two lanthanoids, lutecium (Lu) and ytterbium (Yb) and an element belonging to the same lanthanum's group, yttrium (Y). When the group started to produce the first samples trying several different combinations, the results were promising. The T_c increased and new signs of resistivity drop above 70 K continued to appear. There were even anomalies around 100 K. The Houston team, together with a team led by Dr. John Ashburn in Alabama (the two teams started to collaborate in the early 1980s when Chu visited the University of Alabama), narrowed their search to a promising compound, $Y_{1.2}Ba_{0.8}CuO_4$. They were so confident about the sample's properties that, for their first test, they used liquid nitrogen instead of helium. At 5.00 p.m of January 29, 1987, the measurement was made. The specimen resistivity dropped at the unbelievable temperature of 93 K. Everyone was brimming with joy as they had just made history. This was the discovery of a lifetime.

The significance of that result was in breaking the "sound barrier" of superconductivity, surpassing the liquefaction temperature of nitrogen at 77 K. Any weird phenomenon happening above this temperature can be easily transformed into a practical application because liquid nitrogen costs orders of magnitude less than liquid helium. Onnes's long-held dream of a viable application for superconductors finally became a reality.

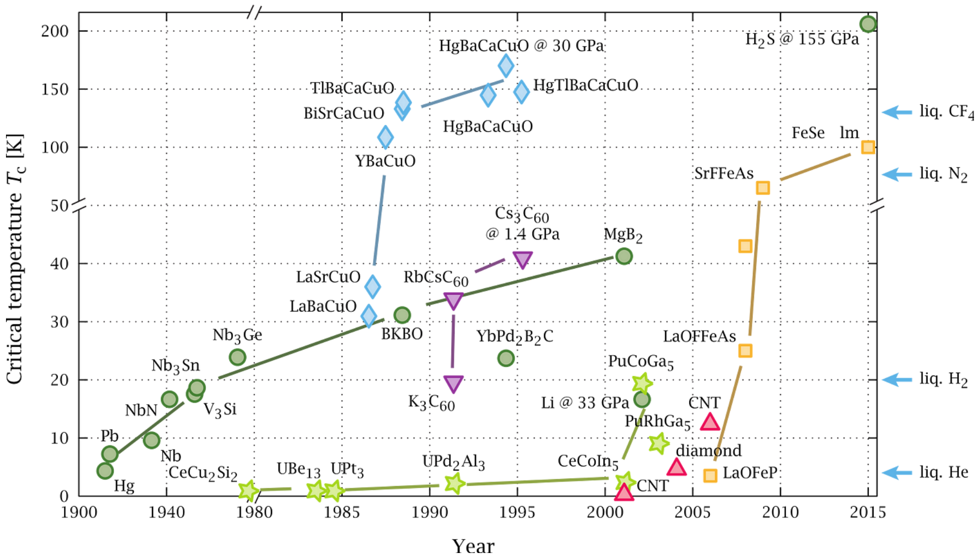

Figure 1.6: Overview of superconducting critical temperatures for a variety of superconducting materials since the first discovery in 1911 [43].

2 | The Theory of Superconductivity

The purpose of this chapter is not to provide a detailed and fully rigorous treatment of the theory behind superconductivity. Rather, it aims to provide a glimpse into the microscopic processes involved without delving too deeply into technicalities. We will start with the first attempts to describe the phenomenon, including the phenomenological theories of the *two–fluid* model and the one proposed by the London brothers. We will then move onto the Ψ and *BCS* theories. Finally, we will examine the properties of a special set of superconductors, the so-called *high temperature superconductors.*

The "theoretical" history of superconductivity went rather slowly immediately after its discovery. This is true, in fact, if we think that the discovery of the Meissner effect, a defining trait of superconductors, dates back to 1933. However, we shall not be surprised about that. Firstly we need to remember that the Leiden laboratory held the monopoly of the production of liquid helium for some fifteen years after the first liquefaction in 1908. Secondly, in 1914 *World War One* broke out and all the scientific projects were stopped or at least slowed down (the same thing that happened during the *World War Two*).

2.1. Two–fluid Model and Thermodynamics

In 1934 the idea that superconductivity could be treated as a phase transition spread. A consequence of this vision is the possibility of introducing two types of electrons, the superconducting and the normal ones. The overall current inside a cable can then be thought as the sum of two contributions:

$$\boldsymbol{J}_{tot} = \boldsymbol{J}_s + \boldsymbol{J}_n, \tag{2.1}$$

where $\boldsymbol{J}_s$ and $\boldsymbol{J}_n$ stand respectively for the current associated with the superconducting electrons and the one associated with normal electrons [2]. We shall now see how we can treat a superconductor using Thermodynamics.

The transition to a particular state of magnetization of a superconductor is a reversible process because it does not depend on the path which has been followed to reach that state but it is influenced just by the magnetic field and temperature values in that instant. Taking magnetic field and temperature as thermodynamic variables one can deduce a simple relation concerning the critical magnetic field strength, H_c, and the Gibbs free energy. The Gibbs free energy state function g is defined in such a way that its change is the maximum amount of work that a thermodynamic system can perform in a process at constant temperature, and its sign indicates whether the process is thermodynamically favorable or forbidden [44]. Furthermore, in any system the most stable state is the one with the lowest value of g. Therefore, if a specimen is cooled below its transition temperature and becomes superconducting, it is because, from a thermodynamic point of view, the Gibbs free energy of the superconducting state is less than the one of the normal state.

Now let's define the Gibbs free energy per unit volume, at temperature T and at zero applied magnetic field $\boldsymbol{H_a} = 0$, as $g_s(T,0)$ for the superconducting state and $g_n(T,0)$ for the normal one. If we apply an external magnetic field $\boldsymbol{H_a}$ and we evaluate the change in free energy, we obtain:

$$\Delta g(\boldsymbol{H_a}) = -\mu_0 \int_0^{\boldsymbol{H_a}} \boldsymbol{M}\, d\boldsymbol{H_a}, \tag{2.2}$$

where $\boldsymbol{M}$ is the induced magnetization inside the conductor, which is, neglecting the penetration depth (more on this later), $\boldsymbol{M} = -\boldsymbol{H_a}$ for a superconductor. So

$$g_s(T,H) = g_s(T,0) + \mu_0 \int_0^{\boldsymbol{H}} \boldsymbol{H}\, d\boldsymbol{H} \tag{2.3a}$$

$$= g_s(T,0) + \mu_0 \frac{H^2}{2}. \tag{2.3b}$$

The last term in Equation (2.3b) represents the amount of free energy increase which is due to the application of the external magnetic field. If, for the sake of simplicity, we consider now the normal state as essentially a non–magnetic state, then its free energy does not increase. The situation is well depicted by Figure 2.1. There is a value of the magnetic field such that the free energy of the normal state becomes lower and hence the latter is the now stable state. The point at which this happens is described by $g_s(T,H_c) \geq g_n(T,0)$, which substituted in Equation (2.3b) gives

$$H_c(T) = \sqrt{\frac{2}{\mu_0}(g_n(T,0) - g_s(T,0))}. \tag{2.4}$$

This formula represents a thermodynamic argument of the existence of the *critical magnetic field strength*, the maximum field that can be applied to a superconductor if it is to remain superconducting [1].

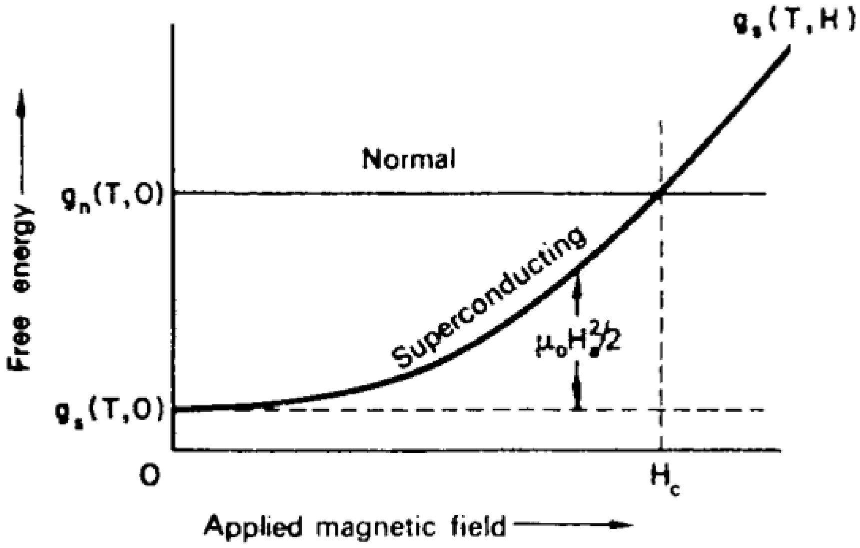

Figure 2.1: Variation of Gibbs free energy with applied field. Plot taken from [1].

We shall now show that the entropy of a superconducting state, at equal pressure and applied magnetic field, is lower than the one of corresponding normal state. By definition, the free energy of a magnetic body is

$$G = U - TS + pV - \mu_0 H_a m, \tag{2.5}$$

where U is the internal energy, T the temperature, S the entropy, p and V the pressure and the volume, and H_a and m are respectively the applied magnetic field strength and the magnetic moment. Differentiating the free energy while keeping p and H_a constant gives

$$dG = dU - TdS + SdT + pdV - \mu_0 H dm \tag{2.6a}$$

$$= -SdT \tag{2.6b}$$

where, to pass from Equation (2.6a) to (2.6b) the *first law of Thermodynamics* has been used. So, dividing by an arbitrary volume, and using again Equation (2.6b) we can obtain

$$s = -\left(\frac{\partial g}{\partial T}\right)_{p,H_a}. \tag{2.7}$$

Using Equation (2.3) and the fact that $g_n = g_s(H_c) = g_s(0) + \frac{1}{2}\mu_0 H_c^2$ we get

$$g_n - g_s(H_a) = \frac{1}{2}\mu_0(H_c^2 - H_a^2), \tag{2.8}$$

which differentiated yields

$$s_n - s_s(H_a) = -\mu_0 H_c \frac{dH_c}{dT}. \tag{2.9}$$

It is a well verified experimental fact that the critical field of a superconductor is a decreasing function of the temperature and hence dH_c/dT is always negative. As a consequence the right–hand side of Equation (2.9) is positive and, as stated above, the entropy of the superconducting state is less than the corresponding normal state [1].

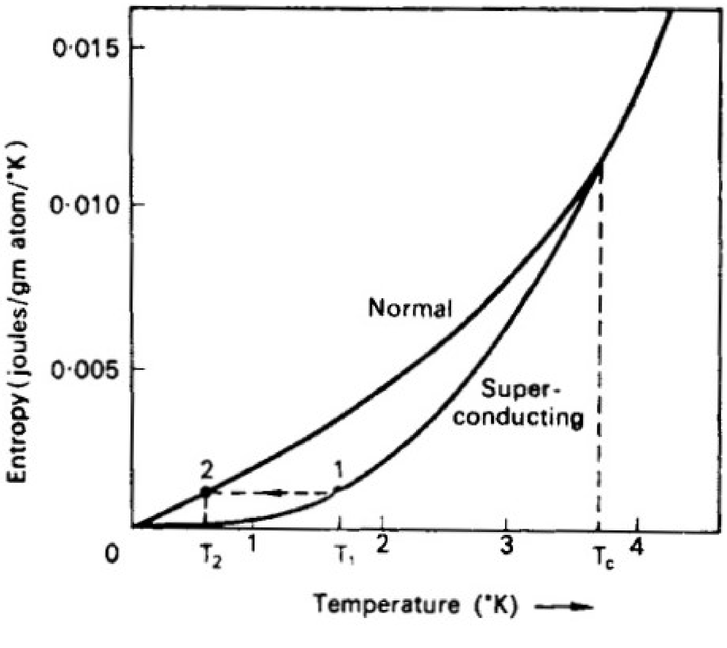

Figure 2.2: Entropy of normal and superconducting states. Plot from [1].

The peculiar nature of the superconducting state is also able to influence the thermal conductivity. We know that the conduction of heat inside a material has two contributions: the one of electrons and the contribution of the lattice, mediated by the its vibrations, or phonons. Which contribution is the dominant one depends on the kind of material, its purity, and its temperature state. In a material in superconducting conditions the superelectrons are no longer able to interact with the lattice in the same way as electrons do in normal conditions and this reflects in their ability in picking up the heat from one part of the specimen and delivering it to another [1]. This effect is more evident as long as the temperature decreases far away from the critical temperature. For temperatures lower than $0.2T_c$ [6], the number of normal electrons with respect to superlectrons is negligible and hence also their contribution to the thermal conductivity. In this range the contribution of lattice becomes dominant, helped by the reduction of its main antagonist, the scattering with normal electrons. To cite an example, at 1 K the thermal conductivity of superconducting lead is about 100 less than that of the same metal in the normal state.

We shall now discuss the specific heat, the thermal property which, maybe more than others, was responsible for the understanding of superconductors and in particular, we will see at the end of this section, for the principle which the two–fluid model was based on. First, we will draw some thermodynamic conclusions and then we will concentrate on the electronic and lattice contributions of the specific heat.

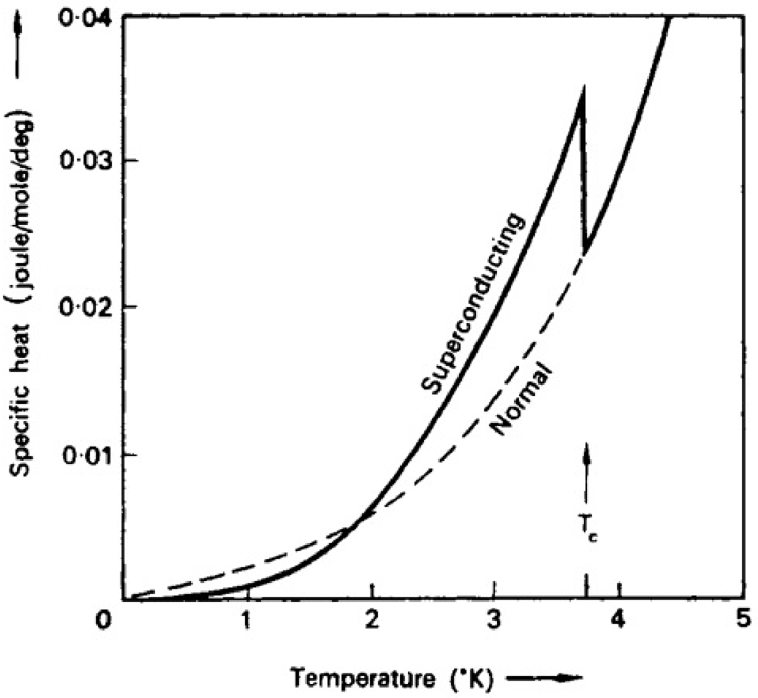

Figure 2.3: Specific heat trend for superconducting and normal state. Plot from [1].

The solid line in Figure 2.3 shows the trend of the specific heat for a superconducting material in the absence of any applied magnetic field. The dashed line, instead, refers to the corresponding normal state in the same thermodynamic conditions (the curve is obtained by applying a sufficiently strong magnetic field to a specimen while decreasing the temperature, for it not to pass the transition).

As it can be seen from Figure 2.2, $s_s = s_n$. Using Equation (2.7) together with the latter equality, we obtain:

$$\left(\frac{\partial g}{\partial T}\right)_n = \left(\frac{\partial g}{\partial T}\right)_s . \tag{2.10}$$

For Ehrenfest, the classification of phase transitions is based on the behaviour of the free energy as a function of particular thermodynamic variables [45]. For example, a transition in which the first derivative of the Gibbs free energy is discontinuous is said to be a *first–order phase transition.* The usual state transitions, like the one from solid to liquid, are of this kind because the specific volume, which is the first derivative of the free energy with respect to pressure, is discontinuous. Equation (2.10) makes clear that the normal–superconducting transition is a *second–order phase transition.* The order parameter (the first derivative) is continuous. A second–order transition is characterized by two properties: the first is that it has no latent heat involved and the second is the discontinuity in the specific heat.

The specific heat of a material is given by:

$$C = \nu T \frac{\partial s}{\partial T}, \tag{2.11}$$

where ν is the specific volume. Putting together Equation (2.11) and Equation (2.9) one can obtain:

$$\begin{aligned} C_s - C_n &= \nu T \frac{\partial (s_s - s_n)}{\partial T} && \text{(2.12a)} \\ &= \nu T \frac{\partial}{\partial T}\left(\mu_0 H_c \frac{\partial H_c}{\partial T}\right) && \text{(2.12b)} \\ &= \nu T \mu_0 H_c \frac{\partial^2 H_c}{\partial T^2} + \nu T \mu_0 \left(\frac{\partial H_c}{\partial T}\right)^2 . && \text{(2.12c)} \end{aligned}$$

In the particular case of the transition where $T = T_c$ and $H_c = 0$, Equation (2.12c) becomes the Rutgers' formula

$$(C_s - C_n)_{T_c} = \nu \mu_0 T_c \left(\frac{\partial H_c}{\partial T}\right)^2_{T_c} . \tag{2.13}$$

This formula, given that we know all the values of the right hand side, gives the discontinuity jump of the specific heat while Equation (2.12c) is more general and holds also when the applied magnetic field is not zero.

As said before, a second order transition is characterized by zero latent heat. However, this is no longer true if we consider an applied magnetic field. The latent heat between the superconducting state and the normal state is

$$
\begin{aligned}
L &= \nu T(s_n - s_s) && \text{(2.14a)}\\
&= -\nu T \mu_0 H_c \frac{\partial H_c}{\partial T}, && \text{(2.14b)}
\end{aligned}
$$

where in Equation (2.14b) has been used Equation (2.9). The equation embodies the special case $H_c = 0$ for which $L = 0$, but also predicts the behaviour when a magnetic field is applied and hence the temperature has to be lower than T_c. The latent heat arises because $s_n > s_s$ for temperatures between T_c and 0 K. If the transition normal to superconducting state is to take place at constant temperature, some heat has to be removed [1]. On the contrary, for example, if the specimen is in an adiabatic superconducting state and a sufficiently strong magnetic field is applied, then no heat can enter the system and the latent heat of the transition has to come at the expense of the internal energy of the lattice whose temperature is going to decrease.

Qualitatively the specific heat reflects the ability of a material to absorb heat and connects the variation of internal energy to the variation of temperature. It has two contributions: one related to the crystal lattice and the other related to the electrons, $C = C_{latt} + C_{el}$. Since during the transition no lattice modification occurs we can state that any eventual difference in the specific heat of the two states arises because of the electronic contribution

$$C_s - C_n = (C_{el})_s - (C_{el})_n. \tag{2.15}$$

We now have to look simultaneously at Figure 2.3 and Equation (2.11). In particular, the latter shows how the higher is the specific heat, the bigger is the rate of variation of the entropy with respect to temperature. As soon as a specimen is cooled down and undergoes the transition, the entropy of the electrons decreases more rapidly than it would in the normal state (for example in the presence of a magnetic field stronger than the critical field, the dashed line). This means that a new source of electron order has to set in, in addition to the normal decrease of entropy with temperature. Since at $H_c = 0$ the process is a second order transition without latent heat involved, the only possible source of entropy decrease is the increasing number of highly ordered superelectrons. That is exactly the way in which the thermodynamic studies on superconductors and in particular of the trends of the specific heat at the transition led to the two–fluid model [1].

As said at the beginning of this section, the idea behind the two–fluid model is the presence of two contributions to the conduction of electric charge. Some electrons behave like superelectrons (they do not make any scattering and hence can travel undisturbed) and the others like normal electrons. We will refer to the fraction of superelectrons to the total number of conduction electrons as x. The x function is an increasing function of temperature and it is such that $x = 0$ for $T = T_c$ and $x = 1$ for $T = 0$ K. So in the range 0 K to T_c there is a mixture of superelectrons and normal ones.

In general in a superconducting cable the current can be carried by both these two contributions. In the particular case of a DC current, however, all the current is carried by superelectrons. We can think of the metal as composed of two parallel conductors in which the superconducting one, the one without resistance, short circuits the other. From another perspective, we can note that for the current to remain constant, and considering the property of superelectrons of not having resistance, there must be no electric field inside the metal. Otherwise the superelectrons would be accelerated continuously and the current would increase without any bound. But if there is no electric field there is no driving potential for normal electrons. We arrived at the same conclusion as before, all the current is carried by superelectrons.

AC current is a completely different situation. If the current is oscillating, there must be an electric field which first accelerates and then decelerates the conduction electrons. So now we have an electric field which drives normal electrons. The oscillating electric field has also another effect. Since superelectrons have an inertial mass, they do not accelerate instantaneously but they lag behind the field. This is enough to generate the so-called inductive impedance of superelectrons. Therefore, now the equivalent circuit is composed of a resistive branch with a parallel perfect inductance. For low frequencies, since the value of the inertial mass of electrons is small and so the inductive impedance, the amount of current which passes through the resistive branch is extremely small and hence the dissipated power is negligible. Contrariwise, if the frequency of the applied electric field is sufficiently high (10^{11} Hz), all the current could be carried by normal electrons and the metal responds as a normal metal [1].

We showed in this paragraph how the two–fluid model is able to explain not only the behaviour of some thermodynamic quantities like the specific heat but also the way in which a superconductor responds to an AC current. Nevertheless, such a phenomenological theory cannot satisfy the desire to discover the true essence of superconductivity. If it was established that below T_c two kind of electrons coexist together, likewise there was no explanation about the nature of superelectrons and the way in which they should differ from normal ones.

2.2. The London Theory

An intermediate step in the comprehension of the phenomenon came in those same years thanks to the London brothers, Fritz and Heinz. Their theory was still a phenomenological theory, but was considered a breakthrough by the scientific community of the thirties [31]. Its main improvement was the incorporation of the Meissner effect, which was discovered one year before the publication of their paper by the German physicists Walther Meissner and Robert Ochsenfeld.

As already stated, at the beginning superconductors were thought as simple perfect conductors, in which current can flow without any resistance. This vision could be easily described using Maxwell's equations and we shall see that it leads to a well-known property of perfect conductors, their ability of "freezing" the magnetic field inside them. The motion of an electron can be described by

$$m\dot{\boldsymbol{v}} = e\boldsymbol{E}, \tag{2.16}$$

where $\boldsymbol{v}$ is the velocity of the superelectron, m and e respectively its mass and charge. Considering now a uniform collection of them, we can express the current density as

$$\boldsymbol{J} = n_s e\boldsymbol{v} \tag{2.17}$$

with n being the number of superelectrons per unit volume. Substituting Equation (2.17) into (2.16) we can obtain the so–called acceleration equation

$$\Lambda\dot{\boldsymbol{J}} = \boldsymbol{E}, \tag{2.18}$$

with $\Lambda = m/n_s e^2$. This equation can be thought of as substituting Ohm's law for superconductors and is a relation between the electric field $\boldsymbol{E}$ and the current density $\boldsymbol{J}$. Given the time derivative nature of the relation, it follows immediately that a steady-state current can be sustained in a superconductor if $\boldsymbol{E} = 0$. We will soon see that Equation (2.18) can be abandoned in favour of a different equation which encompasses the Meissner effect in a more natural way. Taking the curl of Equation (2.18)

$$\nabla \times \Lambda\dot{\boldsymbol{J}} = \nabla \times \boldsymbol{E}, \tag{2.19}$$

using Faraday's law of induction

$$\nabla \times \boldsymbol{E} = -\frac{1}{c}\dot{\boldsymbol{H}}, \tag{2.20}$$

and Ampère's law (neglecting for now the displacement current)

$$\nabla \times \boldsymbol{H} = \frac{1}{c}\boldsymbol{H} \tag{2.21}$$

we finally obtain

$$\nabla \times \Lambda\dot{\boldsymbol{J}} = -\frac{1}{c}\dot{\boldsymbol{H}} \tag{2.22a}$$

$$\nabla \times \nabla \times \Lambda\dot{\boldsymbol{H}} = -\frac{1}{c^2}\dot{\boldsymbol{H}} \tag{2.22b}$$

$$\nabla(\nabla \cdot \Lambda\dot{\boldsymbol{H}}) - \nabla^2\Lambda\boldsymbol{H} = -\frac{1}{c^2}\dot{\boldsymbol{H}} \tag{2.22c}$$

$$\Lambda c^2\nabla^2\dot{\boldsymbol{H}} = \dot{\boldsymbol{H}} \tag{2.22d}$$

From Equation (2.22c) to (2.22d) Gauss's law for magnetism has been used ($\nabla \cdot \boldsymbol{H} = 0$). Now, if one integrates Equation (2.22d) with respect to time obtains

$$\Lambda c^2\nabla^2(\boldsymbol{H} - \boldsymbol{H_0}) = \boldsymbol{H} - \boldsymbol{H_0}, \tag{2.23}$$

where $\boldsymbol{H_0}$ is the magnetic field at time $t = 0$. Equation (2.23) is a nonhomogeneous equation and hence its solution is the contribution of two terms: the general solution coming from the corresponding homogeneous equation and a particular solution. The general solution will generally depend on the geometry and boundary conditions but if, for the sake of simplicity, we concentrate on a 1D case then it becomes an exponentially decreasing function with a characteristic length in the order of $\lambda^2 = \Lambda c^2$. The particular solution might be simply $\boldsymbol{H} = \boldsymbol{H_0}$. Therefore the solution is telling us that the initial field is "frozen" inside the superconductor and the perturbation can only be in a small area near the surface in the order of λ. We could have come to the same conclusion looking directly to Equation (2.22d) and again considering a 1D case. The solution can be approximately of the kind

$$\dot{\boldsymbol{H}}(x) \sim e^{-\frac{x}{\lambda}}. \tag{2.24}$$

This means that the change in $\dot{\boldsymbol{H}}$ is able to penetrate into the material only for a small portion and no information can reach the bulk. If a magnetic field was present, it will remain there, if it was not, it will continue to.

We have just described the behaviour of a perfect conductor. As discovered by Meissner and Ochsenfeld, the problem was that superconductors were proved to be different from perfect conductors: they expel any magnetic field from their bulk. One could be tempted to just set to zero the constant $\boldsymbol{H_0}$ in the solution of the differential equation. It is in this point where the London brothers tried to give their own new vision of the phenomenon. For them, "if not all solutions of a differential equation exist in reality, the equation gives a too general description and should not be used, since it gives Nature more freedom than it wants" [24]. Then we could consider

$$\Lambda c^2 \nabla^2 \boldsymbol{H} = \boldsymbol{H} \tag{2.25}$$

not as a particular integral of Equation (2.23) but as a fundamental law. Taking the curl of Ampère's law and substituting the result in Equation (2.25) one can get

$$\nabla \times \Lambda \boldsymbol{J} = -\frac{1}{c} \boldsymbol{H} \tag{2.26}$$

which London postulated to be the fundamental equation replacing Ohm's law in superconductors [24]. This last equation embodies, by definition, the Meissner effect. This was the reasoning behind the original London's paper. These equations can be used to deduce the behaviour of a superconductor and in particular their most important successes were the incorporation of the Meissner effect and a first evaluation of λ, the London penetration depth, the layer in which a magnetic field is allowed to penetrate into the material.

2.3. The Quantum Mechanical Theories

2.3.1. The GL Theory

The Londons' theory, as said at the beginning of Section 2.2, had been a breakthrough in the theoretical explanation of superconductivity. It introduced the concept of *penetration depth*, which was used also by other theories later on. Its main problem was that, strictly speaking, it held just in case of a weak field, that is $H < H_c$ [2]. The theory which tried to cope with this problem was the so–called Ψ–theory and was published in 1950 by Lev Landau and Vitaly Ginzburg. We have already seen in Section 2.1 that the transition from the normal to the superconducting state is a second–order transition. Because of that we can express an *order parameter* Ψ, which, at equilibrium, is equal to zero for the disordered phase, while it is non-zero in the ordered one. For superconductors we can imagine that $\Psi = 0$ for the normal state and $\Psi \neq 0$ for the superconducting phase. Landau and Ginzburg chose a complex Ψ and they let it play the role of an "effective wavefunction of superconducting electrons" [2]. Using a standard rule in quantum mechanics, the function is normalized such that its module squared is the concentration of superconducting electrons.

The Helmholtz free energy density of a system composed of a superconductor and a magnetic field is

$$F_{sH} = F_{s0} + \frac{H^2}{8\pi} + \frac{1}{2m}\left|-i\hbar\nabla\boldsymbol{\Psi} - \frac{e}{c}\boldsymbol{A}\boldsymbol{\Psi}\right|^2, \tag{2.27a}$$

$$F_{s0} = F_{n0} + \alpha|\boldsymbol{\Psi}|^2 + \frac{\beta}{2}|\boldsymbol{\Psi}|^4, \tag{2.27b}$$

where $\boldsymbol{A}$ is the vector potential and α and β are the Taylor expansion coefficients of the free energy of the superconductor with respect to the order parameter. Let's now consider the easiest case, that is in absence of magnetic field. In thermodynamic equilibrium the first derivative of F_{s0} with respect to $|\boldsymbol{\Psi}|^2$ must be 0, while the second derivative has to be positive. Performing the calculation one obtains directly that β has to be always positive while

$$|\boldsymbol{\Psi}|^2 = -\frac{\alpha}{\beta}. \tag{2.28}$$

So, to stick to the definition of an order parameter given earlier, it turns out that $\alpha_c = \alpha(T_c) = 0$ and $\alpha < 0$ for $T < T_c$. In this way it is easy to verify that $|\boldsymbol{\Psi}|^2 = 0$ for $T > T_c$ and $|\boldsymbol{\Psi}|^2 > 0$ for $T < T_c$. Assuming $\alpha = \alpha_c^0(T - T_c)$ and $\beta(T) = \beta_{T_c} \equiv \beta_c$, Eq (2.28) becomes

$$|\boldsymbol{\Psi}|^2 = -\frac{\alpha_c^0(T - T_c)}{\beta}. \tag{2.29}$$

Eq (2.29) shows that the superconducting state is stable only for $T \leq T_c$ and it can be related, by the normalization definition, to the density of superconducting electrons [8].

In the presence of a magnetic field, the variation should be taken with respect to $\boldsymbol{\Psi}$ and $\boldsymbol{A}$ and one obtains

$$\frac{1}{2m}\left(-i\hbar\nabla\boldsymbol{\Psi} - \frac{e}{c}\boldsymbol{A}\boldsymbol{\Psi}\right)^2\boldsymbol{\Psi} + \alpha\boldsymbol{\Psi} + \beta|\boldsymbol{\Psi}|^2\boldsymbol{\Psi} = 0 \tag{2.30a}$$

$$\nabla^2\boldsymbol{A} = -\frac{4\pi}{c}\boldsymbol{J} \tag{2.30b}$$

$$\boldsymbol{J} = -\frac{ie\hbar}{2m}(\boldsymbol{\Psi}^*\nabla\boldsymbol{\Psi} - \boldsymbol{\Psi}\nabla\boldsymbol{\Psi}^*) - \frac{e^2}{mc}|\boldsymbol{\Psi}|^2\boldsymbol{A} \tag{2.30c}$$

The solution of the system of equations (2.30) gives the distribution of the magnetic, current and $\boldsymbol{\Psi}$ fields. It is interesting to notice that if we assume $\boldsymbol{\Psi} \equiv \boldsymbol{\Psi}_\infty = const$ then (2.30c) reduces to the Londons' equation [2]. Because of that, the penetration depth that can be retrieved by this theory coincides with the Londons' one, that is

$$\lambda^2 = \frac{mc^2\beta_c}{4\pi e^2|\alpha|} = \frac{mc^2}{4\pi e^2|\boldsymbol{\Psi}_\infty|} = \frac{mc^2}{4\pi e^2 n_s}. \tag{2.31}$$

One of the essential parameters which pops out from the Ψ–theory is called the GL parameter and is the quantity

$$\varkappa = \frac{mc}{e\hbar}\sqrt{\frac{\beta_c}{2\pi}} = \frac{\sqrt{2}e}{\hbar c}H_{cm}\lambda^2, \tag{2.32}$$

where H_{cm} is the critical magnetic field strength. Using an argument based on the sign of the surface tension, Landau discovered that the GL parameter could be used to distinguish two different types of superconductors. If $\varkappa < \frac{1}{\sqrt{2}}$ the surface density is positive and we can talk about type–I superconductors. On the other side, if $\varkappa > \frac{1}{\sqrt{2}}$ the surface density is negative and the superconductor is said to be a type–II. The theory shows also that for a type–II there could be a *mixed state* in which an instability superconducting phase is formed inside the otherwise normal phase. Superconductivity does not disappear until the applied field exceeds $H > H_{c2} = \sqrt{2}\varkappa H_{cm}$. We shall discuss more on the difference between these two types of superconductors in the next Section.

Lastly, the theory involves another length parameter. This parameter is called *coherence length* and reads

$$\xi = \frac{\hbar}{\sqrt{2m|\alpha|}} = \frac{\hbar}{\sqrt{2m\alpha_c^0(T_c - T)}}. \tag{2.33}$$

We will talk more about it in the next Section, as well, but here it is useful to annotate that the GL parameter can be expressed as

$$\varkappa = \frac{\lambda(T)}{\xi(T)}. \tag{2.34}$$

2.3.2. The BCS Theory

As pointed out in the introduction of this Chapter, the progress in the theoretical knowledge of this subject was rather slow. However, after more than 40 years of scientific evidences collected by researchers all over the World, in 1957 a new microscopic theory appeared in the scene and earned its owners, John Bardeen, Leon Cooper, and John Robert Schrieffer, the Nobel prize in 1972. The evidence being collected during those years was the presence of a band gap at the Fermi level, the isotope effect and the drastic rise (as shown in Section 2.1) of the heat capacity [50]. The existence of critical temperature and magnetic field and the exponential increase of the heat capacity all go into the direction of an energy gap. Because of the Pauli exclusion principle electrons are not allowed to condense in a single level and have the same energy. However, "a drastic change in conductivity demanded a drastic change in electrons behavior [21]". Furthermore, it was discovered that the critical temperature of a metal was influenced by the mass of the lattice ions (isotope effect). This relation was more than a coincidence because its proportionality was found to be like the inverse of the square root of the mass, the same as the Debye frequency of phonons in a lattice. The lattice should be involved. To understand the foundations of the BCS theory (as it is now called) we should start from these two independent pieces of information. The first step is to allow, in some way, electrons to be bound together. They are negatively charged particles so they tend to repeal each other via Coulomb interaction. The mechanism was first proposed by Herbert Frohlich in 1950, and allows an electron–electron interaction mediated by phonons, the quasi–particles which describe the quantized lattice vibrations. Identifying this interaction as the responsible for the attraction between electrons is nevertheless not sufficient and most importantly does not lead to superconductivity.

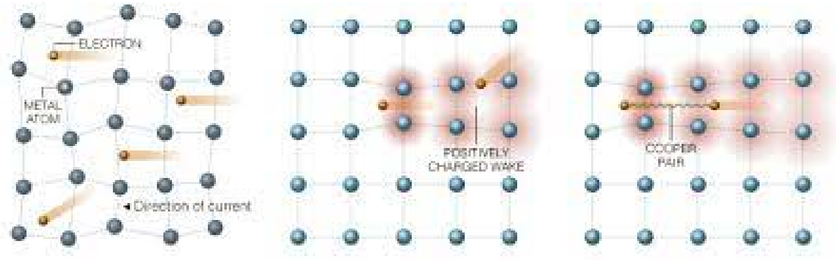

Figure 2.4: Electron–phonon mechanism [9]

The way in which such an interaction provides an attractive force lies in the quantum mechanical formulas of the theory but the following gives the general idea. As shown in Figure 2.4, when an electron passes by some lattice positions it slightly attracts them and hence induces a local modification of the charge concentration. Another electron passing by will be attracted by that positive polarization. The two electrons have exchanged momentum by means of the exchange of a *virtual* phonon. How can the phonons be involved in superconductivity and simultaneously be the cause of resistivity in normal metals? This is not a paradox. First of all, the two "kinds" of phonon involved have two different range of frequencies. Then, we shall remember that the best normal conductors which have a weak electron–phonon interaction do have also bad superconducting properties and viceversa.

The second step is to demonstrate what happens, from an energetic point of view, when an attractive interaction is allowed for electrons. Generally in physics, a system composed of two bodies tends to form a bound state if, once the system is bound, its energy is less than the sum of the energies of the bodies considered unbound. This means that during the formation of the system a certain amount of energy is released (the binding energy) and it has accomplished its thermodynamics duty of seeking the lowest energy state it can occupy. However, it is not taken for granted that under the influence of any attractive potential, two electrons can bind together. Indeed, the force coming from the phonon interaction is extremely weak. Nevertheless in 1956 L. Cooper pointed out that the possibility for two electrons to form a bound state is made possible by the influence of the remaining $N-2$ electrons, through the Pauli exclusion principle [5]. As said before, the electron–phonon interaction is way to small to "glue" together two isolated electrons, but he pointed out that the presence of all the other Fermi sea electrons changes radically the problem in a way in which a bound state starts becoming possible, no matter how weak the attractive force is. This is an example of a *many–problem*. If we want to add two electrons to an already full Fermi sea, there is no other way for us to provide them with an energy greater than the Fermi energy. The energy of the system will increase by an amount equal to the sum of the kinetic energies of the two electrons. Cooper anyway claimed that if that two electrons form a pair, then the energy of the system is somehow lowered. To use specific words, the Fermi sea is unstable against the formation of bound pairs [31].

Now we have the two main ingredients, the mechanism which provides the attractive force and the evidence that forming a bound pair is energetically favorable for the system, and they have to be put together. This is what was done by the already mentioned Bardeen, Cooper and Schrieffer when they proposed their BCS theory. The theory is a *mean field theory*, that is it considers the behaviour of a pair not to be influenced by all the other electrons, except when it comes to decide whether a state is free to be occupied or not. Each pair is described by a bound–state wave function $\phi(\boldsymbol{r}, s; \boldsymbol{r}', s')$ in which $\boldsymbol{r}$ is the position vector and s is the spin. If one has to consider the wave function of all the N electrons then it has just to multiply together N/2 identical bound–state wave functions ϕ

$$\Psi(\boldsymbol{r}_1, s_1; ...; \boldsymbol{r}_N, s_N) = \phi(\boldsymbol{r}_1, s_1; \boldsymbol{r}_2, s_2) \cdot ... \ \phi(\boldsymbol{r}_{N-1}, s_{N-1}; \boldsymbol{r}_N, s_N) \tag{2.35}$$

Nevertheless, such a wave function does not obey Pauli exclusion principle and it has to be antisymmetrized

$$\Psi_{BCS} = \Upsilon\Psi \tag{2.36}$$

where Υ is the so–called antisymmetrizer. We remind here that even if sometimes it could be tempting to consider the pair of fermions like a single boson, they are anyway different from a quantum mechanical point of view. We can see this from the fact that Ψ_{BCS} has to satisfy the Pauli principle, but it would be even clearer if we looked at the commutation relations for the creation and annihilation operators of the Cooper pairs. While one of the three commutation relations is similar to that of bosons, the other two are related to the exclusion principle, highlighting the fundamental difference between Cooper pairs and bosons. Since electrons have half–integer spin they can be paired into singlet ($s = 0$) or triplet states ($s = -1, 0, 1$). In the BCS hypothesis the pairs are singlet states so the electrons have opposite spin, while the orbital part of the wave function $\phi(\boldsymbol{r}, \boldsymbol{r}')$ is symmetric.

If we impose that it is not important the absolute position of the two electrons but just their relative displacement (the state exhibits translational symmetry) then we could write

$$\chi(\boldsymbol{r} - \boldsymbol{r}') \sim \sum_{\boldsymbol{k}} \chi_{\boldsymbol{k}} e^{i\boldsymbol{k}\cdot\boldsymbol{r}} e^{-i\boldsymbol{k}\cdot\boldsymbol{r}} \tag{2.37}$$

so that χ is the superposition of products between two one–electron levels with *equal* and *opposite* wave vectors [5]. It can be demonstrated that pairs of electrons with opposite momenta are those which are characterized by the lowest energy.

Using the tools provided by the theory, one can obtain the spatial range ξ_0 of the pair wave function. It turns out that it corresponds to the coherence length proposed by Brian Pippard and independently also by the Ψ–theory. It is of the order of magnitude of many thousands atomic lengths. Because of that many Coopers pairs overlap in space and this is essential to the stability of the state. The BCS theory requires that, as seen from Equation (2.36), all pairs belong to the same quantum state which can hence be regarded as an highly ordered state. This order does not extend over the size of a single pair but instead covers the whole lattice.

We can now use all of these concepts to explain superconductivity. The whole set of properties of superconductors outlined in previous Sections can be considered not as the essence of the many–body state, but rather as a reaction to it. Every feature of a superconductor derives from the metal trying to remain in its reduced–energy BCS ground state [31]. When an electric field is applied to a superconductor all the pairs continue to move in an ordered way, this time with a nonzero net momentum set by the value of the field. We could have expected collisions of pairs with thermal phonons, impurities, etc to reduce their net momentum down to zero, in the same way as it happens in normal metals. However, we have now to consider the interconnection of all the pairs promoted by the BCS state. All pairs should be described by identical pair wave functions. Thus a single wave function cannot be changed without changing all others simultaneously, an action which would require an enormous amount of energy and hence does not happen.

2.4. High Temperature Superconductors

Not every superconductive material discovered in laboratory can be easily transformed into a magnet–grade superconductor. This is especially true if we think about the difference between Type I and Type II superconductors. It is no coincidence that Kamerlingh Onnes, back in 1913, after his outstanding discovery, did not succeed in building even a small lead coil. Indeed, lead, as almost every other metal, is a Type I and this means that it loses its superconductivity if exposed to a very small magnetic field (0.1 T), even to its own self–field.

Since all *high temperature* superconductors are Type II, it is worth summarizing what makes these kind of superconductors different from Type I. We already saw that according to the Ψ –theory, a natural distinction between two kind of behaviours can be envisaged if we consider the $\varkappa$ value. Type I ($\varkappa < \frac{1}{\sqrt{2}}$) superconductors never allow the magnetic field to penetrate inside them. They have just one critical magnetic field B_c and if $B < B_c$ and $T < T_c$ they are said to be in the Meissner state: they superconduct, show perfect diamagnetism and their magnetization M is everywhere (a part for the already mentioned London penetration depth) equal and opposite in direction with respect to the magnetic field H. From an engineering point of view, they are not useful for two reasons. First of all, as said at the beginning of this Section, their $B_c = \mu_0 H_c$ are extremely low (less than 0.1 T) and then they allow the current to flow just inside the penetration depth defined by the London parameter λ. Since these values are in the order of 10^{-6} cm the current flow can be considered just a superficial phenomenon and the vast majority of the bulk has no usefulness in this regard.

A completely different situation can be depicted for a Type II ($\varkappa > \frac{1}{\sqrt{2}}$). One can distinguish an *ideal* case and a *non–ideal* one, but since, similarly to Type I superconductors, the former has no practical applications, we shall directly discuss just the latter. Type II superconductors have two critical magnetic fields, $B_{c1} = \mu_0 H_{c1}$ and $B_{c2} = \mu_0 H_{c2}$, respectively the lower and the upper critical field. Both B_{c1} and B_{c2} are temperature dependant and in order for the metal to superconduct, of course, it has to be maintained, as usual,

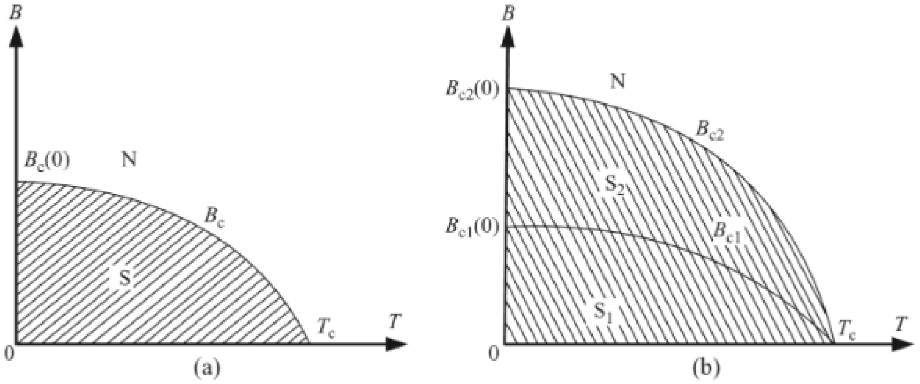

Figure 2.5: Phase diagram of a Type I (a) and Type II (b). Images taken from [42].

to a temperature below its critical temperature T_c. As it can be seen from Figure 2.5(b), there are two distinguished phases. In the range $0 < B < B_{c1}$ the superconductor is said to be in the *Meissner* state. Here its behaviour is very similar to that of a Type I: it is fully diamagnetic and hence does not allow any magnetic field inside it. Instead, in the range $B_{c1} < B < B_{c2}$ it is in the so–called *mixed* state. In this state, inside the material one can find both a normal and a superconducting phase. The superconductor is a mixture of normal–state "islets" embraced by a superconducting sea arranged into a more or less ordered structure [22]. An islet has a radius of ξ, the spatial parameter of Section 2.3. Since this region is in the normal state, a magnetic field can penetrate it and, as a result, screening currents will build up around it to screen the superconducting sea from the magnetic field. The scale over which these screening currents can survive is just the λ parameter. When the magnetic field is increased toward the value B_{c2}, the normal to superconducting zone ratio increases up to the point in which (at B_{c2}) the material is driven completely back in the normal state and stops being a superconductor.

If we consider an ideal and perfect lattice of normal islets it is clear that, in the bulk of the superconductor, the screening currents cancel each other out and no net current can be transported by the material bulk (ideal Type II). However, if the material is non–ideal, then the lattice, because of defects and other imperfections, is non uniformly distributed and this allows a net current density component also in the material interior. For this reason Type II superconductors are usually able to carry a considerably higher amount of current than any other material. Another important property of these materials is the *remanent magnetization*: if a previously applied magnetic field is removed, the magnetic field and the magnetization inside the material are not zero [42]. The non linear behaviour of the magnetization is caused by crystal defects of various kinds which determine the so–called pinning effect. These pinning centers hamper the flux lines to enter or exit from the conductor. Their role is however more profound. Let's go back a little and consider an ideal Type II superconductor in the mixed state. Here the *vortexes* (the regions around the normal islets where screening currents flow) are able to move and if an external current is applied they will be subjected to a Lorentz force

$$\boldsymbol{f}_L = \boldsymbol{J} \times \boldsymbol{e}_z \Phi_0 \tag{2.38}$$

where Φ_0 is the fluxon, the quantized amount of magnetic flux which can flow inside a normal islet [8]. Because of the motion, an electric field $\boldsymbol{E} = \boldsymbol{B} \times \boldsymbol{v}_L$ is generated and hence also energy dissipation. To avoid this vortex flow, and to apply a pinning force to them, pinning centers presence is aided during the fabrication process. They can be simple point defects but also dislocations, grain boundaries, columnar defects etc.

Among the category of Type II superconductors, there is, as pointed out in Section 1.4, a special set of materials called *high temperature* superconductors, HTS for short. They have the outstanding ability to superconduct above the liquid nitrogen temperature (77 K). This property will be important in future applications because liquid nitrogen is extremely less expensive than liquid helium.

Critical temperatures and fields of some Type I and II superconductors

Type I	$T_c[K]$	$B_c[T]$	**Type II**	$T_c[K]$	$B_{c2}[T]$
Ti	0.39	0.0100	**NbTi**	9.8	10.5
Al	1.18	0.0105	**MgB_2**	39.0	35
Sn	3.72	0.0305	**Nb_3Sn**	18.2	24.5
Hg	4.15	0.0411	**YBCO**	93	150
Pb	7.19	0.0803	**Bi2223**	110	>100

Table 2.1: Critical temperatures and fields of some Type I and II superconductors. Data taken from Table 1.2 of [22].

The main class of high–T_c is the cuprate superconductors. They are sometimes called ReBCO to highlight their composition: one Rare–earth and barium compound and a copper oxide layer. Maybe the most famous example of a ReBCO is the already mentioned *Yttrium Barium Copper Oxide*, commonly known as YBCO. Its chemical composition can be expressed by the formula $YBa_2Cu_3O_{7-x}$, where the x stands for the oxygen deficiency (an important parameter which is able to influence the critical temperature). The crystal structure of such a compound plays a fundamental role in its properties and can be described as following. Layers of yttrium atoms are sandwiched between two contiguous CuO_2 pyramidal layers. For each Y atom there are two of Ba arranged in line and moreover one–dimensional chains of Cu-O-Cu are placed perpendicularly with respect to the pyramidal layers [8].

After the discovery of HTS in 1986, there was a euphoria–resignation curve similar to that of the one which followed the Onnes' discovery. The materials seemed to have an enormous practical potential, but at the same time some of their properties made them infeasible for cable production. Among them, the two most important ones were a particularly low critical current and very poor mechanical properties. Using different processing techniques, three different HTS materials were created and commercialized: Bi–2223 powder–in–tube conductors, the Tl–1223 spray–pyrolyzed films and Bi–2212 melt–processed thick tube films [18]. They comprised what now is called the *first generation* HTS wires.

All of three had low J_c and after several years of intense studies it turned out that this was linked to their polycrystalline nature and in particular to the angle distribution of grain boundaries. High angle grain boundaries act like weak–links leading to a suppression of the current, while percolative networks of low angle boundaries have the opposite effect [18]. Furthermore, they all required a great amount of silver and this made them immediately non-competitive compared to a normal copper wire. All these problems led to the *second generation* of HTS. New processes were developed which all went into the direction of obtaining crystallographically biaxially textured and flexible metallic substrata. Among them we can name the Ion Beam Assisted Deposition (IBAD) or the Inclined Substrate Deposition (ISD). In each case the current density which has been obtained reached asymptotically the one of a single crystal. These cables have the potential to carry many hundreds or even thousands times the current carried by a standard copper wire.

To be able to use and operate an HTS cable it is essential to know the $E - J$ characteristic curve. It describes the electromagnetic behaviour of the superconductor because it encapsulates the conductive and vortex state properties of the material [8]. As already pointed out, in fact, the build up of a Lorentz force acting on the current vortexes generates an electric field and hence produces an electrical resistance. A wide–spread model involves a power law of the kind

$$E \sim J^n, \tag{2.39}$$

where n is called the index or n–value of the superconductor. Moreover, an equally important task to be addressed is the definition of a so–called *scaling law*.

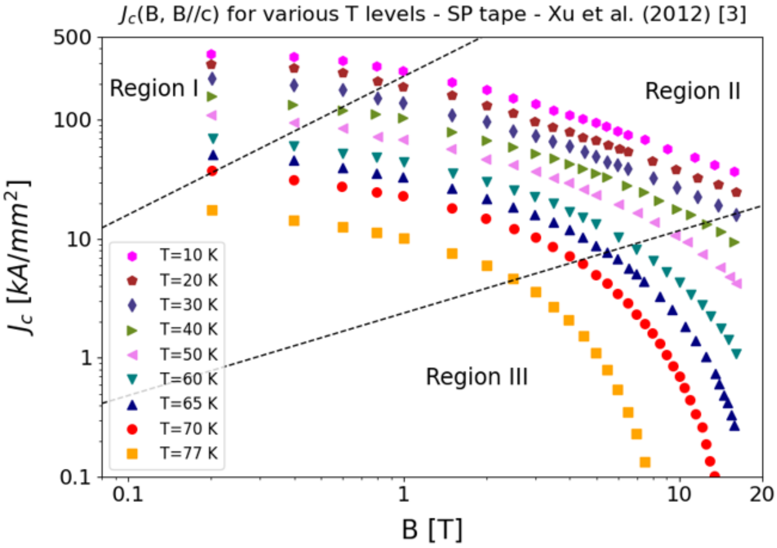

Figure 2.6: The $I_c(B)$ dependence is the combination of 3 regions in a log–log plot [40].

The critical current density (or equivalently the critical current) depends not only on the temperature and the magnetic field, but also on the stress (and corresponding strain) state and the angle between the cable and the B field. The definition of such a scaling law is particularly difficult and nowadays is still a subject of active research in the field, one reason being the limited availability of complete data–sets. As it can be seen from the plot in Fig 2.5 there are three distinct regions if we consider the dependence of I_c over the magnetic field B when the temperature and the angle are kept fixed. Without entering into to many details, the first region is characterized by a flat behaviour and is called the single vortex pinning regime. The second one shows a linear decrease and is referred as the collective pinning regime while the last one has a rapid decrease and is the thermal activation region [40]. One of the most recent attempts to recreate this behaviour in every different zones reads

$$I_c(B, T = T^*, \theta = \theta^*) = I_{c,0} \cdot \left(1 + \frac{B}{B_0}\right)^{-\alpha} \cdot \left(1 - \frac{B}{B_{irr}}\right)^{-q}, \tag{2.40}$$

where all the parameters should be referred to the specific point for which $T = T^*$ and $\theta = \theta^*$ and B_{irr} is said to be the the irreversibility field (the one for which $J_c = 0$) [40]. Regarding instead the scaling law with respect to temperature, two classical approaches can be mentioned

$$J_c(T) \sim e^{-T/T^*} \tag{2.41a}$$

$$J_c(T) \sim \left(1 - \frac{T}{T_{irr,0}}^{\nu}\right) \cdot \left(1 - \frac{T}{T_{irr,0}}^{\mu}\right) \tag{2.41b}$$

Equation (2.41a) is an exponential dependence where T^* is a fitting parameter [37]. On the other side, Equation (2.41b) is expressed in terms of a product of two scaling functions, where ν and μ are critical exponents related to the superconducting and normal state properties, respectively [26]. Another important dependence to be considered, especially for magnet–grade cables, is the relation between the angle between the crystalline axis of the superconductor and the direction of an applied magnetic field. Generally, the higher the field, the more pronounced the dependence, up to a point where a genuine peak can be observed at a specific angle. Therefore, given a specific point in the (T, B) plane, one can take advantage of a considerably higher critical current density (up to ten times higher) by choosing the correct angle.

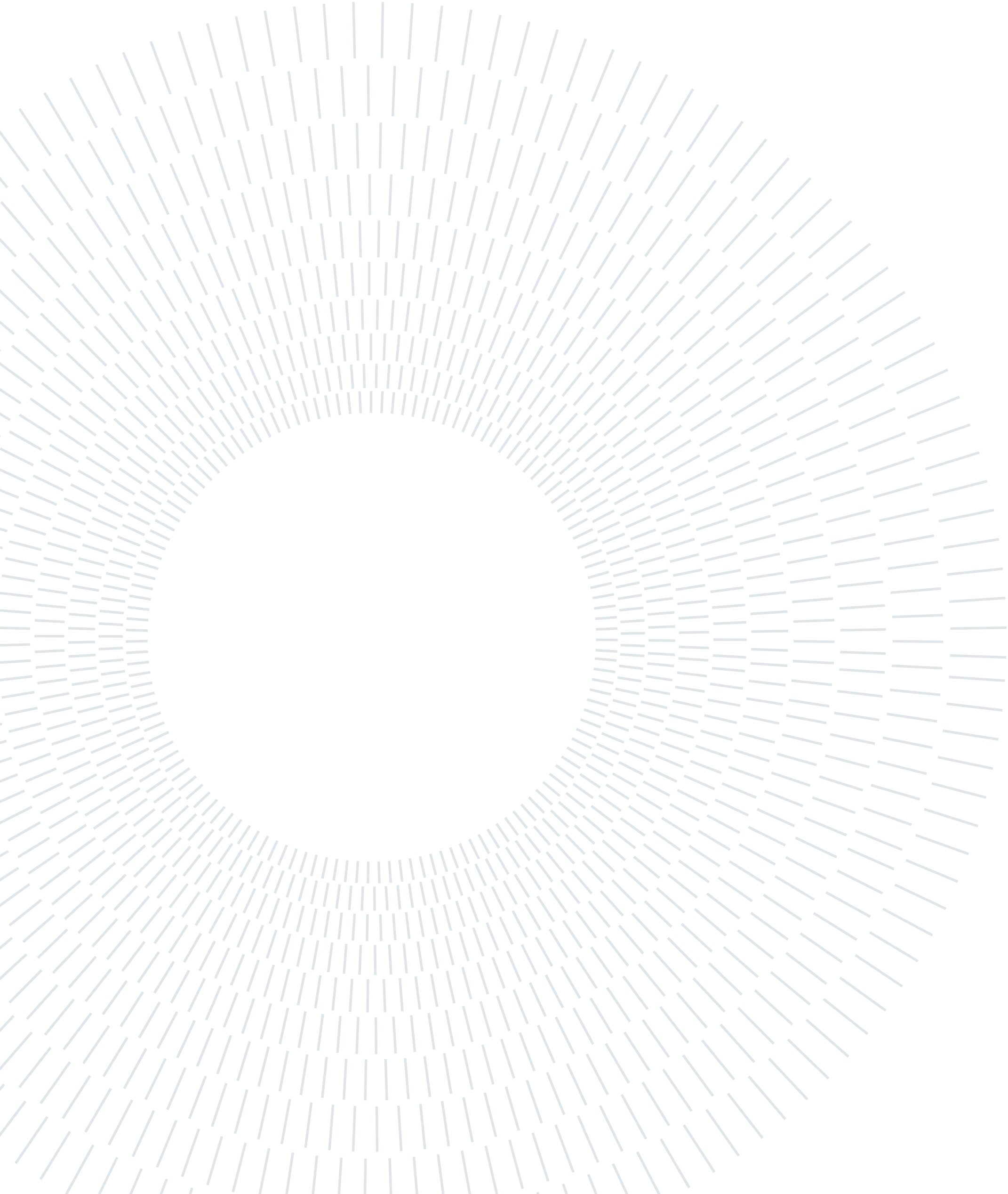

3 | The Muon Collider and the Cooling

At the time of writing this thesis work, the Large Hadron Collider (LHC) is commencing its third operational phase, called Run 3. After Run 3, it will undergo a major upgrade known as the High-Luminosity LHC (HL-LHC) project. The HL-LHC is expected to increase the machine luminosity by a factor of 10, which will enable the study of rare processes and allow physicists to explore new physics beyond the scope of the LHC's current capabilities. However, as time passes and more discoveries are made, the scientific potential of even the largest and most complex accelerator ever constructed will ultimately reach its limits. That is why the European community is currently studying new plans for the next strategy of particle physics.

As highlighted in the European Strategy for Particle Physics Update (ESPPU), the construction of the next generation of particle accelerators and colliders will be extremely challenging due to the technological obstacles that must be overcome to meet the high performance requirements [27]. It is important to note that, in addition to to the classical factors of cost affordability and useful timescale, the ESPPU envisions a key aspect that represents a new and important factor to be taken into account for the construction of future particle accelerators which is the sustainability [27].

Several projects are currently under evaluation, among which the most significant is the Future Circular Collider (FCC). While it will be always a proton-proton collider, the FCC is envisioned to produce collisions at energies up to 100 TeV, more than seven times that of its predecessor.

Nevertheless among these, in the author's opinion, one of the most challenging and interesting proposals is that of a Muon Collider, which is basis for this entire thesis work.

3.1. Why a Muon Collider?

Besides luminosity, two parameters that are of indisputable importance in a particle accelerator are the *energy* of the beam and the *precision* of the measurements. With high-energy machines, we can access energy frontiers for which new particles may be discovered. With high-precision machines, on the other hand, we can study already known processes with unprecedented accuracy, searching for slight deviations from the results predicted by the Standard Model. Unfortunately, these two strategies are characteristic of different kinds of colliders: proton colliders for high-energy machines and electron/positron colliders for high-precision machines. A muon collider can naturally achieve both goals, making it a promising tool for the particle physics research of the future [4].

The most important difference between a muon and a proton is that the latter is a composite particle rather than a point-like one. Moreover, a proton should not be thought of as being composed solely of three valence quarks (two "up" and one "down"), but rather also of gluons and other "partons". There are two main consequences. The first one is that when two protons collide together, as they do in LHC, not all their energy is exploited. Indeed, the proton-proton collision is rather a parton-parton collision and each parton carries just a fraction (defined by the PDFs, Parton Distribution Functions) of the total momentum of the proton. If we define the momentum of a parton a as $p_a = x_a \cdot p_A$, where x_a is the fraction of the proton A momentum p_A carried by the parton a itself, then the first Mandelstam variable $\hat{s}$ of the process can be written as

$$\hat{s} = (p_a + p_b)^2 = x_a x_b s, \tag{3.1}$$

where $s = (p_A + p_B)^2$. Then we can conclude that the energy available for the reaction ($E = \sqrt{\hat{s}}$) is reduced by a factor $\sqrt{x_a x_b}$ with respect to that, in principle, available considering the two protons ($E = \sqrt{s}$). The second consequence is that those partons which do not undergo the main head-on collision, also hadronize (they are color carrying particles so are not able to live alone and produce soft jets of hadrons) generating the so-called Underlying Events (UE). These UEs not only make the main event not "clean" but they are also non-perturbative and hence difficult to be modelled.

In contrast, in a muon collider, a muon μ and an anti-muon $\bar{\mu}$ collide and provide a very clean environment, especially for electroweak studies. The final states are typically simple, easy to recognise and to distinguish. Moreover, oppositely than protons, the two muons provide their full center of mass energy to produce high-energy reactions. The difference between hadron and lepton (in this case muon) colliders can be seen in a quantitative way using Figure 3.1a.

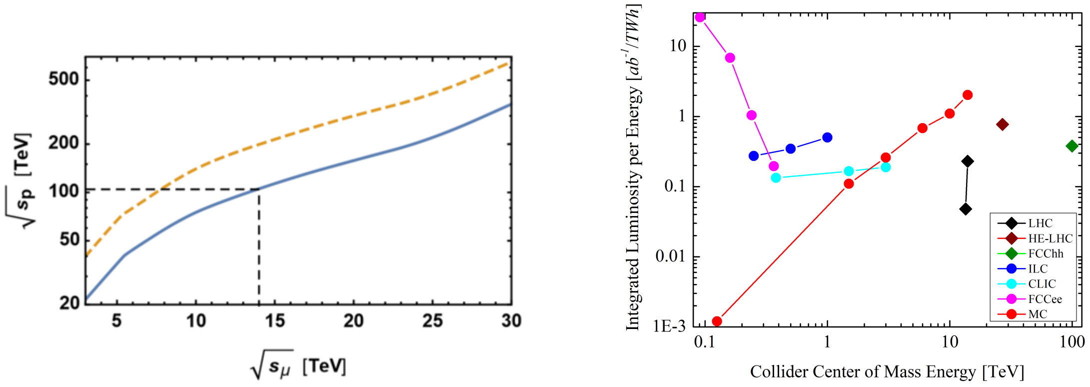

(a) Equivalent proton collider energy

(b) Integrated luminosity per energy

Figure 3.1: Left panel: equivalent proton collider energy. In orange $\beta = 1$, in blue $\beta = 10$. From [4]. Right panel: annual integrated luminosity per electric power consumption. From [25]

The plot shows the center of mass energy $\sqrt{s_p}$ that a proton collider should have to be "equivalent" to a muon collider of $\sqrt{s_\mu}$. The equivalence is expressed in terms of the pair production cross-section for heavy particles and depends on a parameter, β, which defines the relative strength of the interaction for partons and muons [4]. The dashed orange line represents $\beta = 1$ and corresponds to heavy particles which can be produced by electroweak interactions. The solid blue line ($\beta = 10$), instead, corresponds to QCD particles which are extremely more probable in an hadron collider. At the end we can conclude that a 14 TeV muon collider has the potential to provide a similar discovery reach as a 100 TeV proton collider.

Another important aspect that should be considered, especially in light of what has been said in the introduction of this Section about sustainability, is shown by Figure 3.1b. The plot makes a comparison among different machines, like the LHC but also including the next generation colliders (FCC, CLIC and the Muon Collider), with respect to the annual integrated luminosity normalized to TeraWatt-hour of electric power consumption, plotted as a function of the center-of-mass energy. As can be easily seen, the Muon Collider efficiency increases with energy. Above $\simeq 3$ TeV, a muon collider is expected to be the most energy-efficient choice [25].

For what concerns the physics potential of such a machine, its main goal is to be a so-called Higgs factory. Exploiting the considerably higher s-channel coupling of muons with respect to electrons and the high value of the Higgs production cross section, a significantly high number of Higgs bosons can be produced, allowing for a precision study

of their characteristics.
The last aspect we shall consider is the synchrotron radiation. It is well known that charged particles which follow a curved trajectory lose part of their energy because of synchrotron radiation. The amount of energy lost is proportional to

$$\Delta E_{turn} \sim \left(\frac{E}{m}\right)^4 \tag{3.2}$$

and hence is heavily dependant on the mass of the particle. Electrons in LEP2 (the electron-positron collider at CERN before LHC) lost almost $\Delta E \sim 3\ GeV$ per turn. It is clear that no high-energy circular collider could make use of electrons. On the contrary, the mass of the muon ($105,6\ MeV$), about 207 times bigger than that of an electron ($0.511\ MeV$), greatly suppresses the synchrotron radiation losses and makes muons the only viable choice for a lepton circular accelerator.

3.2. Layout of a Muon Collider

We shall now examine, without providing a fully detailed description, the layout of a Muon Collider. The information presented here is the result of a study that began in 2011 in the US called MAP (Muon Accelerator Program), which aimed to assess the feasibility of the concept as a whole, as well as all the required technologies. It is therefore important to note that a fully integrated design has yet to be developed.
The design of a muon collider is driven by the peculiar nature of the particles involved, which are fundamentally different from the "standard" electrons or protons used in previous accelerator designs, particularly in two important aspects: they have to be produced by nuclear reactions and they are unstable, decaying into electrons (and neutrinos) in $2.2\ \mu s$. As it can be seen from Figure 3.2, the Muon Collider consists of five different stages:

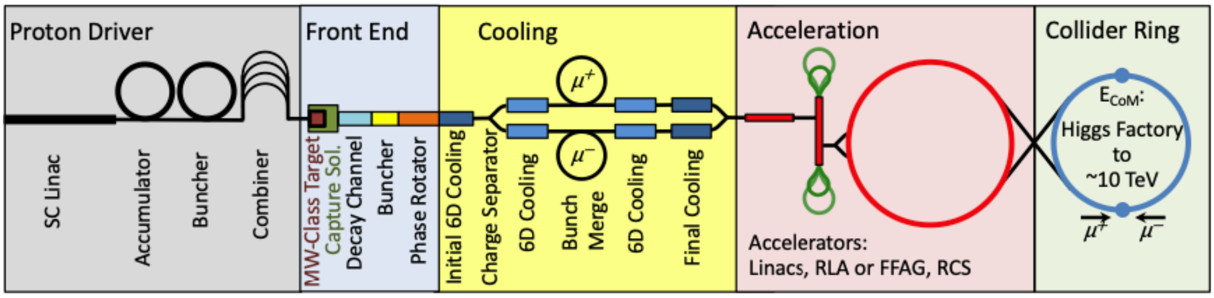

Figure 3.2: The US MAP design of the Muon Collider, from [29]

the proton driver, the front end, the cooling, the acceleration and finally the collider ring. Muons are not available in nature in the same way as protons and electrons, which can be obtained starting from a simple hydrogen bottle. Muons have to be created using nuclear reactions and one way to do this is by using bunches of protons. The first stage is thus a complex where protons are first accelerated by a linac, and then handled by sequence of other structures (the accumulator, the buncher and the combiner) which have the purpose of preparing suitable bunches to be thrown against a target. The proton beam should have an energy between 5 to 15 GeV and a power of about 2 MW.

In the *target* and *capture* section the proton bunches are made collide against a target. In preliminary studies each bunch is composed of 10^{14} 5 GeV protons with a repetition rate of 5 Hz. The target is a 80 cm long graphite rod on which protons produce pions by spallation reactions. The rod is inserted into an aluminum vessel filled with helium, which has the scopes of preventing the graphite from sublimating and also to promote heat dissipation. The aluminum vessel, together with a tungsten shield, is surrounded by an high field capture solenoid [36]. The solenoid's function is that of capturing the produced pions and guiding them toward the decay channel, where they will decay into muons. The muons will then be captured in bunches by other solenoids and RF cavities [11].

The next stage, the *cooling*, will be discussed more in depth in Section 3.3. Here we can anticipate that the cooling of the muon bunches is essential because their original 6D emittance is six orders of magnitude larger than the desired final one. To accomplish this goal a lattice of different stages of solenoids alternated by RF cavities and absorbers is used.

The penultimate step is the *acceleration* stage. Here the muons are finally accelerated toward their final energy. The first step is composed of linacs (in the original plan a room-temperature linac and then a superconducting one) in which muons are rapidlly accelerated using high-gradient RF, on a time frame to ensure adequate survival of the unstable particles [30]. It is just an acceleration to the relativistic regime which can allow an extension of the muon laboratory lifetime. After an intermediate acceleration in Recirculating Linear Accelerators (RLAs), the beams are injected in a series of RCSs (Rapid Cycling Synchrotrons) and HCSs (Hybrid Cycled Synchrotrons). These machines will require normal conducting fast ramped magnets and superconducting static magnets.

The final stage of the whole complex is the *collider ring*. In this part the muons are injected in opposite directions depending on their sign and are stored to make them collide. The ring should be as small as technically possible to avoid high losses due to muon decays.

3.3. The Cooling Stages

3.3.1. General Description

Since the superconductive solenoids of the next Chapter are those of the cooling stage, it is worth to give a more detailed description of it.

When muons enter the cooling stage they occupy a large volume in phase-space, which then has to be reduced by several orders of magnitude. Considering the muon lifetime, there is just one cooling method which is viable and it is called *6D ionization cooling*. Its concept is simple: by means of ionization energy loss in absorbers the beam momentum is reduced in every directions but it is then only replenished in the longitudinal one through RF cavities. This process is effective just in the transverse direction and hence *emittance exchange* is also needed. The dispersive beam is let pass through properly designed wedge-shaped absorbers such that the low-energy particles traverse less material and are longitudinally cooled less, and vice versa. The net result is a reduction of the longitudinal emittance at the expense of the transverse one. The emittance is then exchanged in the two directions and can be later "removed" by the ionization cooling [39]. The emittance exchange, together with the ionization, accounts for the complete 6D cooling of the muon bunches.

The 6D ionization cooling consists of a lattice of 12 different unique stage types, where each stage is a repeating series of a cell type. The number of cells in a stage ranges from 20 to 130, and the total length over 12 stages is 0.9 km. There are four stages before

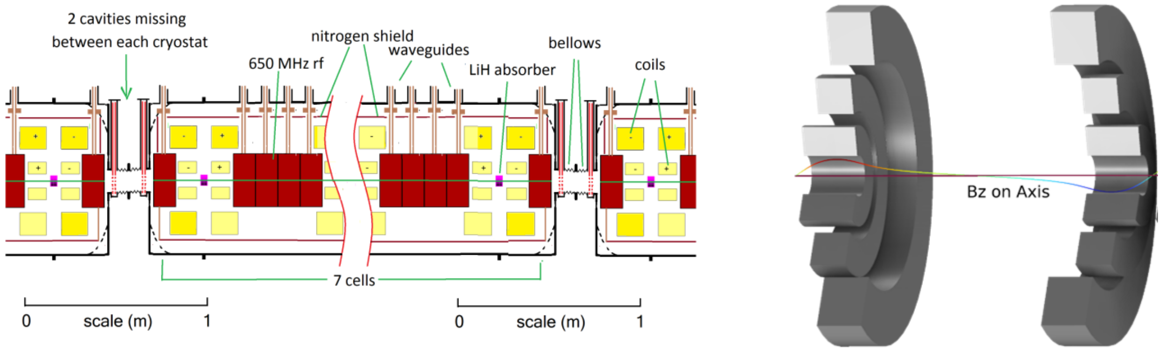

(a) Engineering sketch of the last stage of rectilinear 6D cooling [30]. (b) 3D rendering of B8 solenoids.

Figure 3.3: Left panel: possible engineering integration of a cell. Right panel: image generated using Comsol Multiphysics ©

.

bunch recombination and 8 stages after bunch recombination. We shall now give a general description of a single stage, as they all share a common structure. In each cell there are from a minimum of two solenoids up to a maximum of six and they are shown in yellow in Fig 3.3a. The cell has geometrical specular reflection symmetry, although magnets on the left have opposite polarity with respect to those on the right. The result of such a design choice has consequences on beam dynamics (as we shall see in a while) and produces a (almost) sinusoidally varying magnetic field on-axis, as can be seen from Fig 3.3b and more specifically in Chapter 4. In Fig 3.3a, one can see in dark red the RF cavities and in magenta the wedge-shaped absorbers. The solenoids are not evenly spaced and in particular those nearer to an absorber are also closer together in order to increase the focusing there and thus minimizing the β-function [39]. The original US MAP study foresaw the magnets to be tilted to generate the dipole field necessary to dispersion for emittance exchange. However, more up-to-date evaluations suggest the introduction of dipoles to simplify the engineering design. Indeed, tilting the axis of solenoids in a lattice generates restoring forces which could be difficult to be handled in an already complicated structure.

3.3.2. Lattice Design

The cooling lattice can be subdivided in three sections: the cooling before recombination, the one after recombination and the final cooling. Both initial parts consist of more stages, each with its own set of properties suited for the beam characteristics in that location. Namely, the main goal is to maintain the beam emittance larger than the *equilibrium emittance* (see 3.3.3), which is achieved by adjusting the cell length, maximum magnetic field and RF frequency from stage to stage. As pointed out before, the choice of the magnetic field configuration has a specific dynamics scope. That is to say, the alternation of opposite polarity solenoids allows to counteract the build-up of the canonical angular momentum [17]. The absorbers position, instead, is chosen to coincide with the maximum dispersion and at the same time with the minimum of the beta function.

The first section consists of four stages, from A1 to A4. The first, for example, includes 66 identical cells, each of them 2 m long and containing six independent pillbox cavities, two absorbers and four solenoids. The magnets produce sinusoidal variation of the magnetic field on-axis, with a peak value of 2.4 T. At the absorber position the lattice yields a beta function of 72.2 cm (at 200 MeV/c) and a 10.7 cm dispersion. At the end of the fourth stage the beam should have reached the goal parameters of normalized transverse and longitudinal rms emittances of less than 1.5 mm and 2.5 mm, respectively [39]. All four stages are designed to have the highest possible momentum acceptance because the muons coming from the precedent step, called phase rotation, show a big momentum spread. The phase rotation process provides 21 bunches which are cooled by this first step, one by one. Once all the bunches exit stage A4 the are recombined to produce a single bunch with a proper number of muons. However, recombination increases again the longitudinal and the transverse emittances. So the bunch has to be taken through another cooling section, which, this time, consists of eight stages, from B1 to B8. Conceptually these stages are very similar to those already presented for the previous sections. However, because now one needs a much tighter requirement on the transverse emittance (almost 0.3 mm), the β_T-function has to be reduced to 5 cm. This can be achieved by reducing the length of the cells and by increasing the peak value of the magnetic field. This time, the bunch is expected to have a lower momentum spread and hence the stages do not have to be designed to have a large momentum acceptance.

The last section is the final cooling. The beam exiting from stage B8 has achieved a longitudinal emittance of 1 mm, which is far below the requirement for the collider (70 mm), but a transverse one of 0.3 mm, out of a request for $\epsilon_z = 25\ \mu m$. To accomplish such a result, 13 small-bore high fields solenoids are required [30]. Simulations have shown that 30-40 T magnets could, so to say, suffice but the higher the field the lower the final transverse emittance, for the benefit of the machine luminosity.

The whole cooling process can be best described by Figure 3.4.

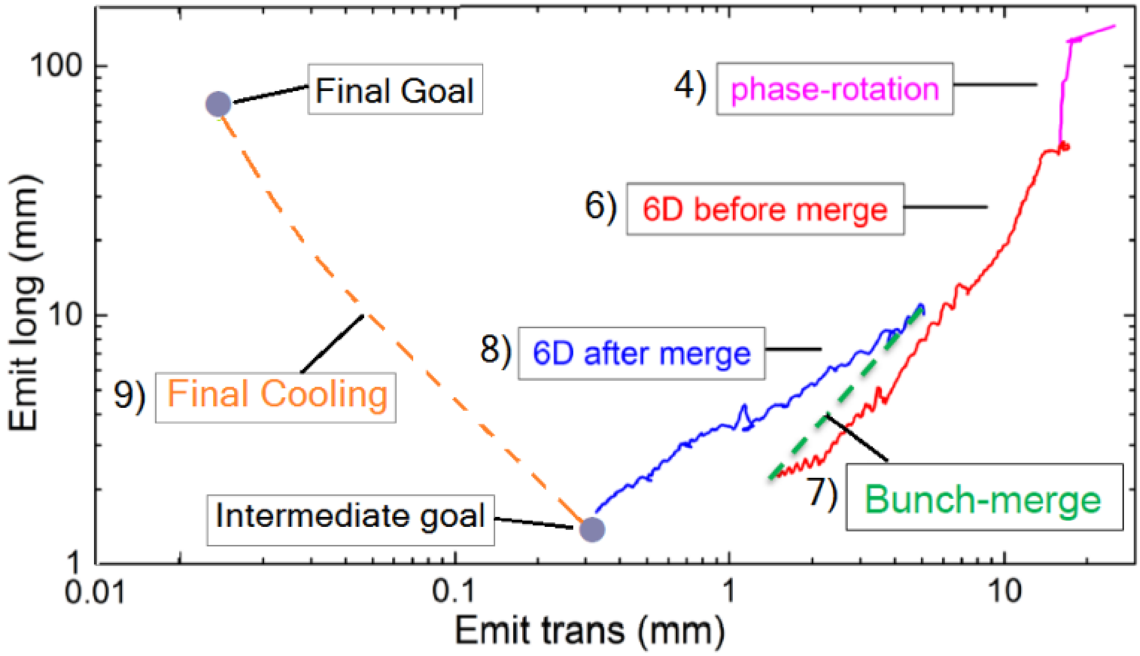

Figure 3.4: Evolution of the emittances from section to section, from [30]

3.3.3. Basic Theory

Without entering too much into beam dynamics details, it is anyway important to have a clue of what the previously cited equilibrium emittance is. As already pointed out, ionization cooling relies on the energy losses due to ionization interactions inside a medium when a beam passes through it. The momentum losses are parallel to the particle trajectories and hence are both in the transverse and longitudinal directions. The RF cavities restore then the momentum just along the longitudinal direction. Therefore the net loss of momentum leads to a reduction of ϵ_T and hence to cooling. Yet we have not considered a side effect: the random scattering processes in the absorber increases the rms beam divergence [39]. The equation of the evolution along the curvilinear abscissa of the transverse emittance (a similar equation holds also for the longitudinal one) is

$$\frac{d\epsilon_T}{ds} = -\frac{g_T}{\beta^2 E}\frac{dE}{ds}\epsilon_T + \frac{\beta_T E_s^2}{2\beta^3 m_\mu c^2 L_R E} \tag{3.3}$$

where we can distinguish two terms, the first one is a reduction term and accounts for cooling while the second one is the heating term due to multiple scattering. Following the order: g_T is a factor describing the wedge-shaped absorber and contains the dispersion, β is the particle velocity, E its energy, dE/ds is the energy loss rate given by the Bethe-Block equation and β_T is the transverse betatron function. L_R and E_s are, respectively, the material radiation length and the characteristic scattering energy.

Looking at Equation (3.3), it is clear that there is an equilibrium emittance ϵ_T^{eq} for which the two terms counterbalance each others. This is the minimum emittance that can be achieved. Putting in (3.3) $d\epsilon_T/ds = 0$ and solving for ϵ_T one can find

$$\epsilon_T^{eq} = \left(\frac{dE}{ds}\right)^{-1} \frac{\beta_T E_s^2}{2\beta g_T m_\mu c^2 L_R}. \tag{3.4}$$

Examining Equation (3.4), it is clear why absorbers are positioned where the betatron function β_T is at its minimum.

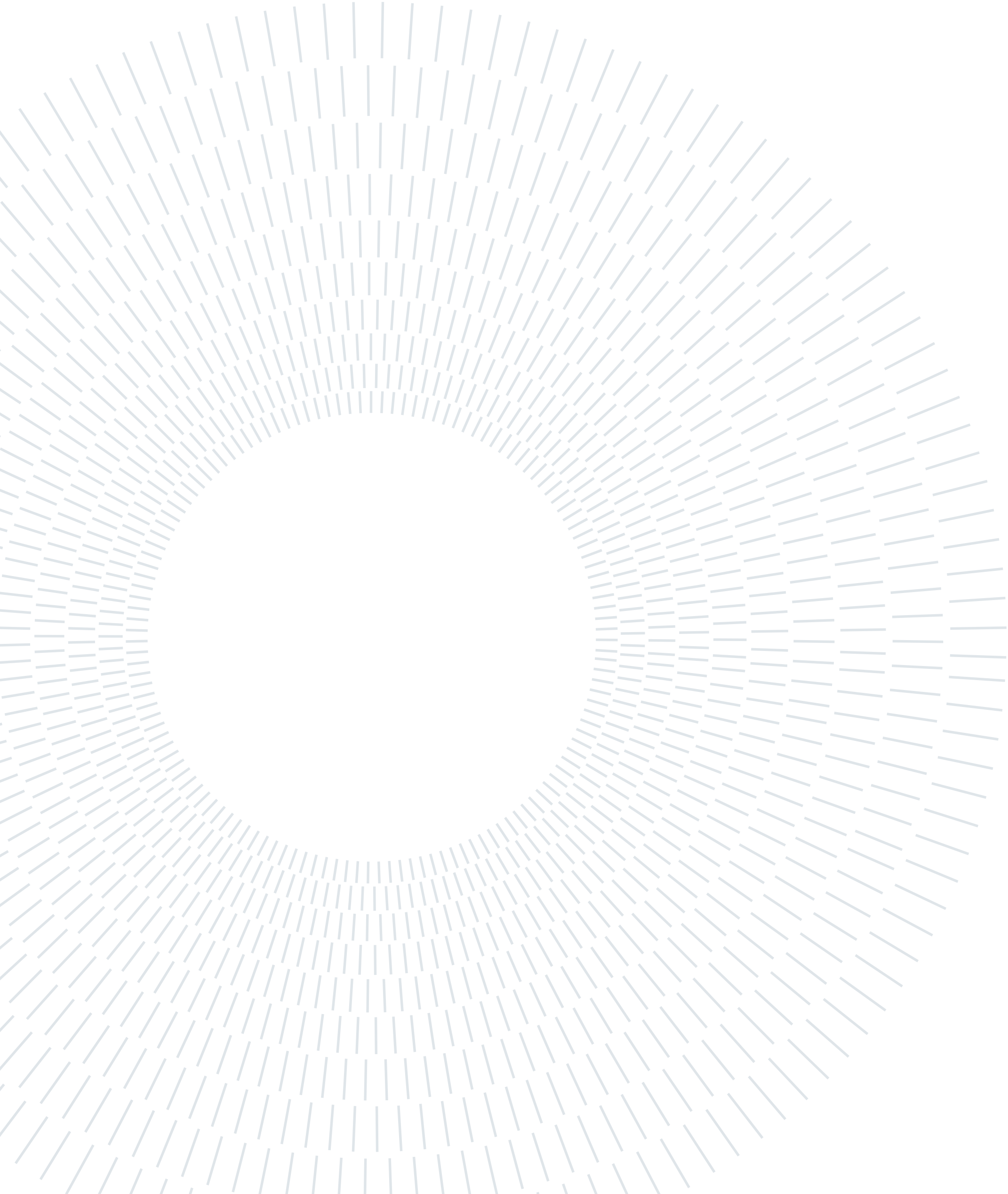

4 | The Solenoids Library

One of the goals of this thesis work has been the initial characterization of the 2954 solenoids which are used in the *6D Cooling* stage of the Muon Collider. It should be emphasized that the magnets described in the US MAP study were primarily designed to fulfill the beam dynamics requirement of producing the appropriate magnetic field on-axis. However, the majority of these magnets were not subjected to a comprehensive engineering analysis to assess their feasibility. The first step in this direction has been the initial characterization of the magnetic and mechanical properties of the 18 unique solenoids that constitute the 12 different stages of the Cooling. To achieve this goal, various tools were employed. Specifically, I developed MATLAB codes to evaluate analytical formulas, and I set up Finite Element Models (FEMs) using Comsol Multiphysics.

This chapter is divided into two sections. The first section presents the methods and the analytical formulas used while the results obtained for the magnetic and mechanical analysis are shown in the second section.

4.1. Magnetic and Mechanical Analysis

4.1.1. Magnetic Analysis: Method and Analytical Formulas

A *solenoid*, within the area of accelerator magnets, is an electromagnet usually characterized by a rectangular section of a wound coil of wire. The simplest configuration involves just a rectangular cross-section, while more complex designs may include notched coils, independently fed radial sections, and other variations.

The magnetic field produced by a general distribution of current can be evaluated from integration of the Biot-Savart law

$$\boldsymbol{B}(\boldsymbol{r}) = \frac{\mu_0}{4\pi} \int_V \frac{\boldsymbol{J}(\boldsymbol{r}') \times (\boldsymbol{r} - \boldsymbol{r}')}{|\boldsymbol{r}' - \boldsymbol{r}|^3}\, d^3r'. \tag{4.1}$$

Simplified solutions of the field on axis or inside a solenoid can be obtained by approximating the solenoid geometry to different limits. The easiest among them is the so-called infinite solenoid, which has an infinite length but a finite diameter. Considering Ampere's circuital law

$$\oint_C \mathbf{B} \cdot \mathrm{d}\boldsymbol{l} = \mu_0 \iint_S \mathbf{J} \cdot \mathrm{d}\mathbf{S} = \mu_0 I_{\mathrm{enc}} \tag{4.2}$$

and a closed path around the conductor, like in Fig 4.1a, we can obtain by a simple integration

$$B = \mu_0 \frac{NI}{l}, \tag{4.3}$$

that is the magnetic flux density B is uniform inside the magnet bore and its value is proportional to the current per unit length.

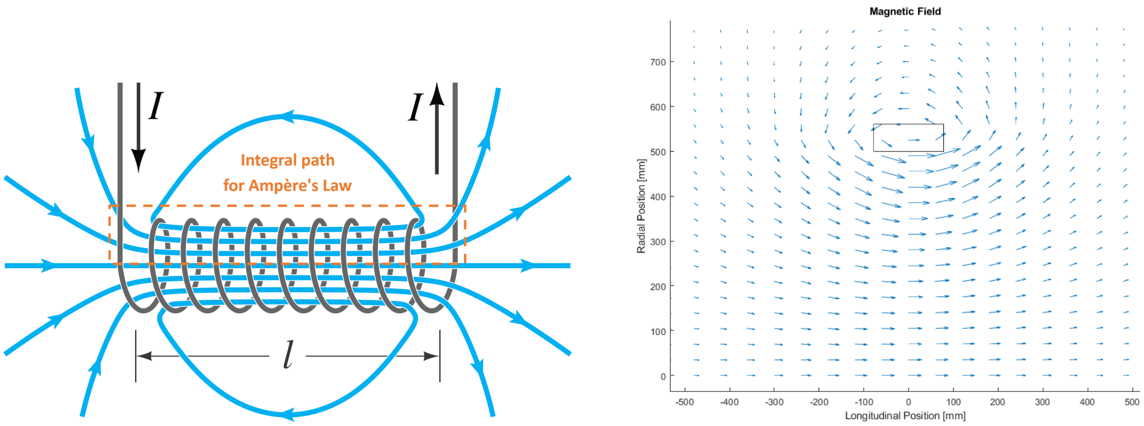

(a) Visualization of the magnetic field and the integration line for the Ampere's Law[14].

(b) Magnetic field of a finite solenoid obtained with my MATLAB code.

Figure 4.1: Magnetic field of a solenoid.

To evaluate the magenetic field of a finite real solenoid there are several methods which have been used in literature: some of them require elliptic functions and elliptic integrals while others infinite series of particular functions. According to [23], the two components of the magnetic field, B_z and B_r, respectively the axial and radial component, can be calculated using infinite series of partial binomial expansions. This approach turned out to be particularly simple to be implemented in a numerical code and precise enough in those regions of special interest, like the on-axis field and the bore volume closest to the axis. As an example, I will show how the z component is obtained.

The Biot-Savart law (Eq (4.1)) for the z component and considering just a cylindrical layer of homogeneous current density reads

$$B_z(r, z) = \frac{\mu_0 I a}{4\pi} \int_{-L}^{+L} dz' \int_0^{2\pi} d\varphi \frac{a - rcos\varphi}{\left[r^2 + a^2 - 2arcos\varphi + (z' - z)^2\right]^{3/2}} \tag{4.4}$$

where I is the total current, and a and $2L$ are, respectively, the radius and the length of the cylindrical layer. For the cylindrical symmetry of the system the azimuthal dependence is not present and the (r, z) plane is a complete representation of the overall three dimensional field. If the integration over z' is carried out, Eq (4.4) becomes $B_z(r, z) = \mu_0 I[F(r, \omega_2; a) + F(r, \omega_1; a)]$, where $\omega_{1,2} = L \pm z$ and F represents the remaining integral over $d\varphi$ after the integration in z'. It is this function which is expressed in terms of an infinite series of partial binomial expansions

$$F(r,\omega;a) = +\frac{\omega}{2\sqrt{r^2+a^2+\omega^2}} \sum_{n=0}^{\infty} \frac{(2n-1)!!}{(2n)!!} \left(\frac{2ra}{r^2+a^2+\omega^2}\right)^n R_n\left(\frac{r}{a}\right) \qquad r < a \quad (4.5a)$$

$$F(r,\omega;a) = -\frac{\omega}{2\sqrt{r^2+a^2+\omega^2}} \sum_{n=1}^{\infty} \frac{(2n-1)!!}{(2n)!!} \left(\frac{2ra}{r^2+a^2+\omega^2}\right)^n \bar{R}_n\left(\frac{a}{r}\right) \qquad r > a \quad (4.5b)$$

where the functions R and $\bar{R}$ are defined as

$$R_n(x) = \frac{1}{2^n} \sum_{k=0}^{[n/2]} \binom{n}{k} x^{n-2k} \qquad n = 0, 1, ... \quad (4.6a)$$

$$\bar{R}_0 = 0, \quad \bar{R}_n(x) = \frac{1}{2^n} \sum_{k=0}^{[(n-1)/2]} \binom{n}{k} x^{n-2k} \qquad n = 1, 2, ... \quad (4.6b)$$

Now, just the following integral separates the solution of an infinitely thin solenoid from the one of a real solenoid with finite thickness

$$B_z^h(r,z) = \frac{1}{a_2 - a_1} \int_{a_1}^{a_2} B_z(r, z; a)\, da \qquad (4.7)$$

where a_2 and a_1 are the outer and inner radii. Eq (4.7) involves both series and integrals and hence a simple analytic result cannot be worked out. However, the mean value theorem says that exists a value $\xi \in [a_1, a_2]$ for which $B_z^h(r, z) = B_z(r, z; \xi)$. Now, the problem has shifted from the evaluation of the integral to the knowledge of that value. The paper [23] claims that a good approximation of ξ, if the thickness is small compared to the inner radius (namely, $h \ll a_1$), is $\xi = \bar{a} = (a_1 + a_2)/2$, the mean radius.

As said before, this approach has been found to be sufficiently precise for the scope of this thesis work. Nevertheless, it is equally true that in the context of further developments, a more reliable and solid method should be used. The author of the paper cites that weak points of this approach based on binomial expansions are some particular regions on the conductor like the edges. In these points, to get a reasonable solution, lots of terms in the expansion of Eqs (4.5) should be used, at the expense of the code computational speed.

Other useful concepts which have been taken into account are those of inductance, mutual inductance and magnetic energy stored by the magnets.

The *inductance* of a magnet, or in general of any electrical conductor, is its tendency to oppose a change in the electric current which passes through it [49]. The existence of an inductance lies in the interrelation among a magnetic field, an electric field and currents. A current flowing through a conductor generates a magnetic field around it, a change in that current produces a change in the magnetic field which reacts back inducing an electromotive force in the conductor. At the end of the loop, the voltage induced opposes the initial change in the current and the inductance can be finally defined as the ratio between the induced voltage across the conductor and the rate of change of the current which produced it

$$v(t) = L\,\frac{\mathrm{d}i}{\mathrm{d}t}\,. \tag{4.8}$$

Such a term inside a differential equation describing a lumped circuit behaves like a viscous term, making the circuit "sluggish" [12]. In the context of magnets for high-energy applications (and not only) this aspect has to be taken into consideration carefully, for protection issues (see Chapter 5) but also for the ramp-up stage. There are several formulas in literature to calculate the self-inductance of a solenoid, and the one which has been used is the so-called Maxwell's approximate formula [35]. It reads

$$L = \frac{aN^2}{\mu_0}\left\{\log\left(\frac{8a}{R}\right)\cdot\left(1+\frac{3R^2}{16a^2}\right)-\left(2+\frac{R^2}{16a^2}\right)\right\}, \tag{4.9}$$

where N is the number of turns which build up the solenoid, a its mean radius and R is defined as the geometrical mean distance of the cross section, $R = 0.2235(a + L)$, with L being the length.

Another concept to be addressed is the *mutual inductance.* As the name suggests, it is related to the same phenomenology of the inductance but this time involves two or more coils (or two or more generic conductors). They are linked together by the magnetic field produced by one which reaches the other and by means of its change induces a voltage in the other. So, the mutual inductance is defined as the ratio between the electromotive force induced in one magnet caused by the rate of change of the current in another magnet. The mutual inductance is particularly important in the 6D cooling of the Muon Collider because its peculiar structure. We saw in Chapter 3 that each stage is composed of different cells and each cell is composed of different solenoids. Theoretically speaking, each solenoid couples with any other in the lattice through the mutual inductance (however, in practice, the influence is primarily limited to those magnets that are in close proximity to each other). Similarly to the self-inductance, also the mutual inductance is described by several formulas in literature. The formula which is best suited for solenoids in our geometry ranges and agrees when compared to numerical evaluation (such as COMSOL) is the Rosa-Maxwell formula [35]

$$M = N^2(M_0 + \Delta M), \tag{4.10}$$

with M_0 being the mutual inductance of the central circles (the coils which represent the "barycenters" of the cross sections) and ΔM a correction factor (Rosa's formula) which takes into account the real and finite dimensions (rectangular cross section) of the two coaxial solenoids. The first order value M_0 is given by Maxwell's formula

$$M = \mu_0 \sqrt{a_1 a_2} \left[\left(\frac{2}{k} - k \right) F - \frac{2}{k} E \right] \tag{4.11}$$

with

$$k = \frac{2\sqrt{a_1 a_2}}{\sqrt{(a_1 + a_2)^2 + d^2}}, \tag{4.12}$$

where a_1, a_2 and d are, respectively, the radii of the first and second coaxial circles and their distance, F and E are the complete elliptic integrals of first and second kind. The correction factor can be taken from Eq (29) of [35].

The last magnetic concept which is worth discussing is the *magnetic energy stored* by a solenoid. Actually, this is a more general concept and holds for every inductor. As said before, when a changing current flows inside an inductor a voltage drop which opposes the current is induced. To maintain the charges flow an external work has to be done on the system and this energy is stored in the magnetic field around the conductor [49]. The change in the system energy, namely the power, is

$$p(t) = \frac{\mathrm{d}U}{\mathrm{d}t} = v(t)\, i(t) \tag{4.13}$$

which, after a couple of simple mathematical steps and considering Eq (4.8), becomes

$$E_m = \int_0^I L(i)\, i\, \mathrm{d}i \tag{4.14a}$$

$$= \frac{1}{2} L I^2 \tag{4.14b}$$

where to obtain Eq (4.14b) a constant inductance L has been considered. The relation between the inductance and the energy stored in a magnet is extremely important, especially when dealing with the protection. Indeed, all that energy, in a quench event, has to be dissipated as fast as possible and this turns out to be a not so easy task if the amount of stored energy is high. If the system is not composed by just one solenoid, as it is the case in the lattice structure of the 6D Cooling, the stored magnetic energy has contributions coming from all the self-inductances but also from all the possible combinations of the mutual inductances. The overall energy stored reads

$$\begin{aligned} E_n &= \frac{1}{2} I^\top \,\underline{\underline{L}}\, I && (4.15a) \\ &= \frac{1}{2} \sum_{m,n=1}^{K} i_m L_{m,n} i_n \ , && (4.15b) \end{aligned}$$

where I is a vector containing all the currents flowing in each solenoid and $\underline{\underline{L}}$ is a symmetric tensor which contains in the diagonal the self-inductances and in the off-diagonal terms the mutual inductances.

4.1.2. Mechanical Analysis: Method and Analytical Formulas

Another important aspect to be taken into account when designing a magnet is the mechanical stress-strain analysis. The magnetic field exerts a so-called Lorentz force per unit volume on the current-carrying conductor [51]

$$\boldsymbol{F}_L = \boldsymbol{B} \times \boldsymbol{J} . \tag{4.16}$$

When dealing with superconductors, this force is particularly high because the current density and the magnetic field are also high. However, among superconductors, HTS magnets suffer even more from this condition because they generally carry an even higher current and are used to produce ultra-high fields. There are several reasons why it is important to evaluate the stress-strain state of the solenoids of the Muon Collider. The first one remains within the boundaries of the mere mechanical analysis. Because of Eq (4.16), the force exerted by the interaction between the magnetic field and the current flowing inside the conductor tends to push the solenoid outward radially. The solenoid behaves similarly to a cylinder under internal pressure. The stress state which results is intrinsically three dimensional and must be considered if the solenoid is to withstand the mechanical load. In order for the solenoid to resist under this load, the calculated stresses must be lower than the maximum allowable values given by the mechanical properties of the material under consideration (e.g. HTS tape). Thus, the accurate determination of the stress state becomes crucial in ensuring the structural integrity and reliability of the solenoid. The peculiar nature of superconductors makes this analysis insufficient. For example, in addition to structural considerations, a magnet designer must also consider that a superconducting cable can sustain an almost flat critical current up to a given stress value but then, it abruptly fails in superconducting. Nevertheless, the most serious problem is related to the quench protection. Under the action of the Lorentz body load force the magnet is taut as a violin string, ready to release locally a great amount of mechanical energy. This local release is one of the possible causes of a quench initiation. Before going through a simplified derivation of the elastic problem, it is interesting to evaluate a real case of Lorentz force density. A solenoid of cell A2 is shown in Figures 4.2.

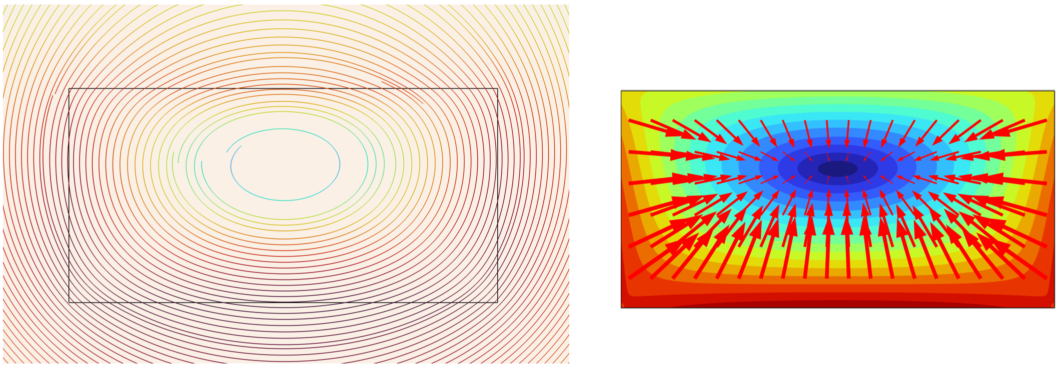

(a) Magnetic field lines in and near a solenoid.

(b) Lorentz force density magnitude and vectorial direction.

Figure 4.2: Magnetic field and Lorentz force density in a solenoid of a cell of Stage A2. The axis of revolution is below the figures. Images generated using Comsol Multiphysics ©.

The left panel is a representation of the magnetic field lines acting on the rectangular cross section of the magnet. The pattern which is shown is the typical field of a finite solenoid. In the bottom central part, the field lines are led by a positive (it is not, actually, important the absolute sign) axial component, while, toward the lateral sides, in order for them to close on themselves, a radial component starts to build up. Given the structure of Eq (4.16), the vectors of the load Lorentz force are always perpendicular to both the magnetic field line and the current density in that point. The result is shown in Fig 4.2b. The strongest component of the field is in the axial direction and produces an outward radial force density. It is this contribution which generates a circumferential hoop stress similar to that of a cylinder under internal pressure. However, the stress state of a solenoid is more complex than the one of the pressurized cylinder because of the curvature of the field lines. Toward the sides of the coil, as it is evident from the right panel, the force has a strong axial component. At the outside, where the magnetic field reverses to allow the field lines to close on themselves, the force field has a non negligible inward radial component. At the end, the final stress state is complicated and not predictable a priori

(it is heavily dependent over the geometry of the coil, we will see later on during this Chapter). Anyway, it is true that the dominant stresses will be a circumferential tension and an axial compression.
It is worth now giving an introduction of the elastic problem in solenoids. The starting point is the mechanical equilibrium equation

$$\nabla \cdot \underline{\underline{\sigma}} + \boldsymbol{B} \times \boldsymbol{J} = 0, \tag{4.17}$$

where $\underline{\underline{\sigma}}$ is the stress tensor and the force density vector has been already substituted by Eq (4.16). Given the cylindrical symmetry of the problem all the stresses are functions of just the axial and radial coordinates. Eq (4.17) in cylindrical coordinates reads

$$\frac{\partial \sigma_r}{\partial r} + \frac{\sigma_r - \sigma_\theta}{r} + \frac{\partial \tau_{rz}}{\partial z} = -JB_z(r, z), \tag{4.18a}$$

$$\frac{\partial \tau_{rz}}{\partial r} - \frac{\tau_{rz}}{r} + \frac{\partial \sigma_z}{\partial z} = -JB_r(r, z), \tag{4.18b}$$

where σ_r, σ_θ and σ_z are the stresses along the coordinate system and τ_{rz} is the shear stress. An orthotropic material has the following symmetric compliance matrix

$$\underline{\underline{S}} = \begin{bmatrix} \frac{1}{E_r} & -\frac{\nu_{\theta r}}{E_\theta} & -\frac{\nu_{zr}}{E_z} & 0 \\ -\frac{\nu_{r\theta}}{E_r} & \frac{1}{E_\theta} & -\frac{\nu_{z\theta}}{E_z} & 0 \\ -\frac{\nu_{rz}}{E_r} & -\frac{\nu_{\theta z}}{E_\theta} & \frac{1}{E_z} & 0 \\ 0 & 0 & 0 & \frac{1}{G_{zr}} \end{bmatrix} \tag{4.19}$$

with E_i the Young's moduli, G_{ij} the shear moduli and ν_{ij} the Poisson's ratios. With the engineering properties of the orthotropic material, it is now simple to relate the stress state and the corresponding strain state

$$\underline{\varepsilon} = \underline{\underline{S}} \cdot \underline{\sigma} \tag{4.20}$$

where $\underline{\varepsilon} = (\varepsilon_r, \varepsilon_\theta, \varepsilon_z, \gamma_{rz})$ and $\underline{\sigma} = (\sigma_r, \sigma_\theta, \sigma_z, \tau_{rz})$. The last equations which are needed to close the elastic problem are the compatibility equations. These equations are necessary to ensure that, during the elastic deformation, no gaps or overlaps develop inside the body. In the case of an axisymmetric solenoid they are

$$\varepsilon_r = \frac{\partial u_r}{\partial r}, \qquad \varepsilon_\theta = \frac{u_r}{r}, \qquad \varepsilon_z = \frac{\partial u_z}{\partial z}, \qquad \gamma_{rz} = \frac{\partial u_r}{\partial z} + \frac{\partial u_z}{\partial r} \tag{4.21}$$

with $u_\theta = 0$. This elastic problem, as it is, is simply too complicated to be solved analytically and as far as we know, there are no closed-form simultaneous solutions for σ_r, σ_θ and σ_z [22]. Indeed, such a problem is generally tackled using finite element methods on computers. However, with some simplifying assumptions, it is possible to arrive at a reasonable estimation of σ_r and σ_θ. The first of them is orthocylindricity, which can be understood as the condition for which a solenoid maintains its cylindrical shape even after undergoing deformation. In other words, if the solenoid begins the elastic problem with a cylindrical shape, it will continue to retain it even after the deformation process. Mathematically, this statement is equivalent to the condition $\gamma_{rz} = \tau_{rz} = 0$. We could have been arrived to the same conclusion considering a "long" solenoid for which all the variables in Eq (4.18a) are independent of z (including u_r [22]). Another assumption is to consider the material as isotropic rather than orthotropic, namely the compliance matrix is now completely determined by the knowledge of just two material parameters, E and ν. The last approximation involves taking into account a linearly decreasing axial magnetic field along the radius, i.e

$$B_z(r) = B_1 - \frac{B_1 - B_2}{a_1 - a_2}(a_1 - r), \tag{4.22}$$

where a_1, a_2 and B_1, B_2 are, respectively, the inner and outer radii and magnetic field values. All these assumptions transform Eq (4.18a) into

$$\frac{\mathrm{d}\sigma_\rho}{\mathrm{d}\rho} + \frac{\sigma_{\rho-\sigma_\theta}}{\rho} = -\frac{JB_1a_1}{\alpha - 1}\left[\alpha - \kappa - (1-\kappa)\rho\right] \tag{4.23}$$

where two nondimensional parameters have been introduced: $\kappa = B_2/B_1$ and $\rho = r/a_1$ (with $\rho(a_2) = a_2/a_1 \equiv \alpha$). Using the same assumptions and approximations also on the constitutive and compatibility equations, after some mathematical manipulations, we get [22]

$$\begin{aligned}
\sigma_\rho = \frac{JB_1a_1}{\alpha - 1}\Bigg[&\frac{2+\nu}{3}(\alpha - \kappa)\left(\frac{\alpha^2 + \alpha + 1 - \frac{\alpha^2}{\rho^2}}{\alpha + 1} - \rho\right) \\
&-\frac{3+\nu}{8}(1-\kappa)\left(\alpha^2 + 1 - \frac{\alpha^2}{\rho^2} - \rho^2\right)\Bigg], \qquad (4.24\text{a}) \\
\sigma_\theta = \frac{JB_1a_1}{\alpha - 1}\Bigg\{&(\alpha - \kappa)\left[\frac{2+\nu}{3}\left(\frac{\alpha^2 + \alpha + 1 + \frac{\alpha^2}{\rho^2}}{\alpha + 1}\right) - \frac{1+2\nu}{3}\rho\right] \\
&-(1-\kappa)\left[\frac{3+\nu}{8}\left(\alpha^2 + 1 + \frac{\alpha^2}{\rho^2}\right) - \frac{1+3\nu}{8}\rho^2\right]\Bigg\}. \qquad (4.24\text{b})
\end{aligned}$$

To get both Eqs (4.24), $\sigma_\rho(1) = 0$ and $\sigma_\rho(\alpha) = 0$ have been used. They state that the radial stress has to be zero at the inner and outer faces of the solenoid. Eqs (4.24) are

useful to get a first idea about the type of stress state which will develop inside the magnet when energized. In particular, it is interesting to study the different families of curves which can be obtained from those results changing some parameters.
Figures 4.3 show plots of normalized hoop and radial stresses for (on the left) a "thin-walled" solenoid and (on the right) a "thick-walled" solenoid. The qualitative definition of a thin or thick solenoid can be made quantitative by examining the value of α, which, as a reminder, is the ratio between the outer and inner radii. To keep the discussion more general, the stresses are normalized

$$\zeta_r \equiv \frac{\sigma_r}{JB_1a_1} \tag{4.25a}$$

$$\zeta_\theta \equiv \frac{\sigma_\theta}{JB_1a_1} \tag{4.25b}$$

For each plot in Figures 4.3 there are different stress profiles at selected field ratios κ.

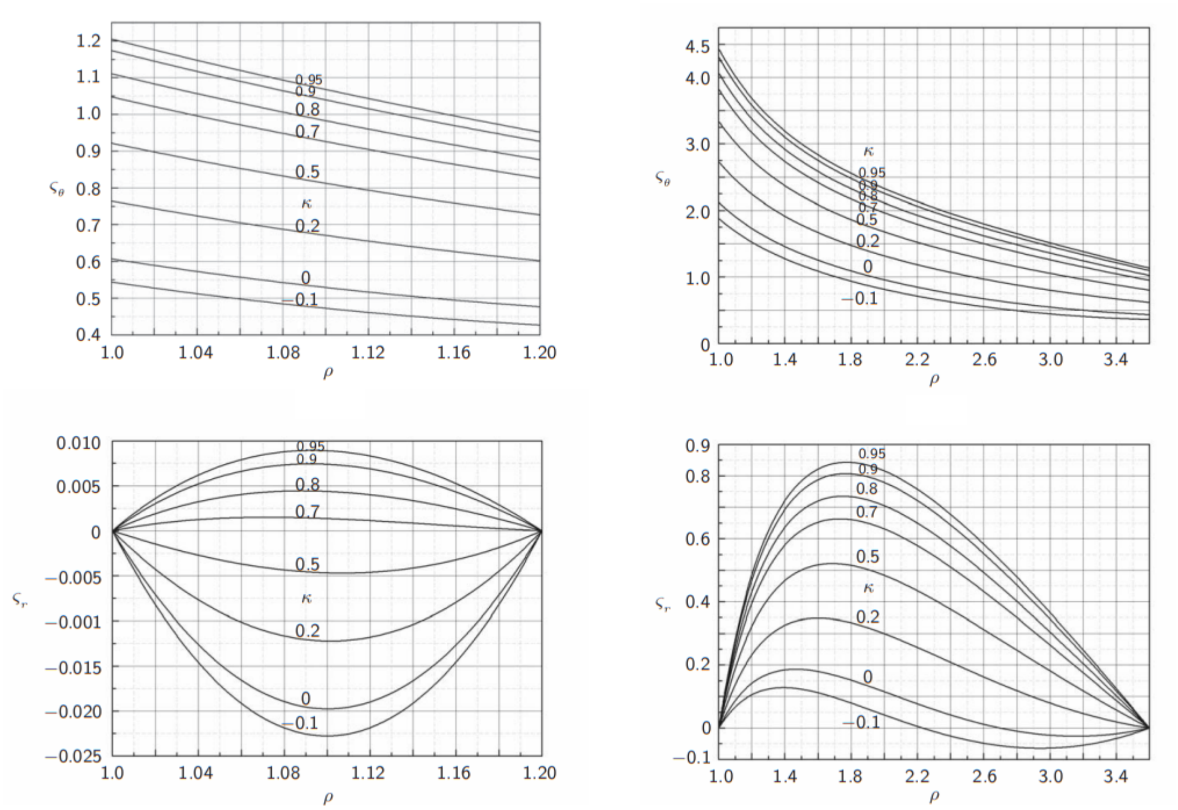

(a) Up left panel: normalized hoop stress
Down left panel: normalized radial stress

(b) Up right panel: normalized hoop stress
Down right panel: normalized radial stress

Figure 4.3: Normalized hoop and radial stresses for (left panels) a "thin-walled" solenoid ($\alpha = 1.2$) and (right panels) a "thick-walled" solenoid ($\alpha = 3.6$) at different values of κ. Plots taken from [22].

The value $\kappa = -0.1$ is appropriate for a stand-alone solenoid. The field lines have to close on themselves (see Fig 4.2a) and hence the value B_2, the axial field on the outer radius of the solenoid, has to be negative. Instead, for an ideal solenoid with no field outside it, $\kappa = 0$. Positive values of κ fit for coils exposed to a background field.

The normalized hoop stress curves are very similar for the two cases: the stress is a decreasing function of the radius and hence the maximum value and the maximum circumferential solicitation occur at the inner radius. It can be noted from Fig 4.3a and 4.3b that a thicker solenoid has, at the same κ, an higher stress state.

The radial stress state is more complicated. As expected from the choice of the boundary conditions, the profile starts at zero at the inner radius and comes back to zero at the outer radius. For the "thin-walled" coil, the radial stress forms a parabola with upward concavity for reasonable values of the field ratio (such as -0.1), transitioning from compressive to tensile at higher values (greater than 0.5). The "thick-walled" solenoid, instead, presents always a tensile profile unless κ is zero or negative. In this case the coil is in a mixed state: the inner part of the solenoid is under tension while the outer part is under compression. In general, experiencing a radial stress state of tension is unfavorable for a solenoid as it leads to the separation of turns. This condition should be particularly avoided for HTS magnets, as second-generation HTS tapes are prone to delamination.

4.1.3. COMSOL Simulation Settings

As previously mentioned in the preceding sections, numerous calculations involved in studying a magnet necessitate computer programs, specifically finite element software. There are several such programs, each with its own advantages and disadvantages. The software that has been used was Comsol Multiphysics ©. It encompasses the capability to simulate a wide range of phenomena, including acoustic, computational fluid dynamics (CFD), electromagnetic, mechanical analysis and many others, all within a single computer program. Additionally, it offers a user-friendly interface for easy operation and navigation. A Finite Element Method (FEM) is a numerical method for solving partial differential equations within a so-called boundary value problem. It is based on a space discretization of the system which is accomplished by a mesh. A continuous solution is approximated by a discrete one. For each element of the domain, a set of algebraic equations which reflects the physics of the problem is formulated. Then, these equations are assembled together to form a global system of equations. The assembly process involves combining the element-level equations to generate a bigger system of equations. The global system of equations is constructed by connecting the equations of neighboring elements through shared nodes or interfaces, thus generating a system of linear or non-linear equations that represents the behavior of the entire system. Boundary conditions and constraints are also incorporated into the global system. Once the global system of equations is assembled, it can be solved using numerical methods, like matrix inversion or iterative techniques, to obtain the solution for the unknowns and determine the behavior of the system as a whole.

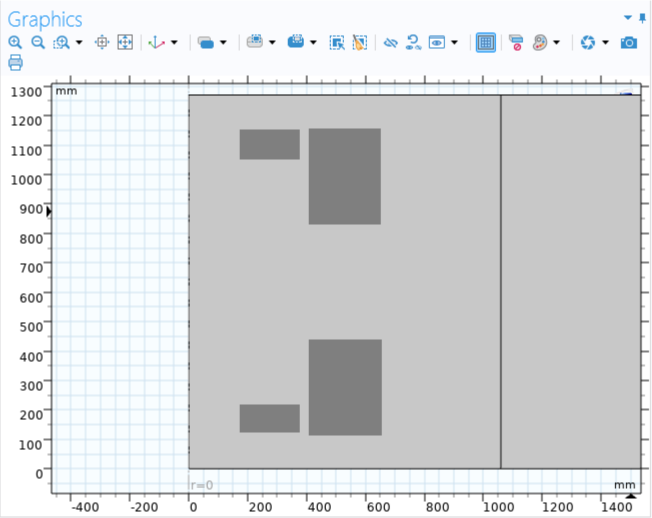

Figure 4.4: Geometry of cell B4, graphic interface of Comsol.

The electromagnetic and mechanical analysis of all the cells of the 6D Cooling of the Muon Collider was a collaborative effort between myself and CERN Fellow Siara Fabbri and it was performed using Comsol Multiphysics. Among all the possible physics moduli that can be used, I employed just two: the *Magnetic Fields* and the *Solid Mechanics* moduli. The first modulus allows to generate the geometries of the coils and energize them producing the magnetic fields. The second one takes as an "input" the Lorentz forces produced by the interaction between the currents and the self-produced magnetic fields and, by means of suitable structural boundary conditions, evaluates the stress state which is generated inside the magnets. In Comsol, you have the option to choose the dimensionality of the problem (1D, 2D, or 3D) and, if applicable, consider symmetry. In my case, the geometries of all the cells were axisymmetric, so the appropriate model was used. This step is of paramount importance: whenever a system exhibits symmetry, it is crucial to utilize it as it enables a significant reduction in simulation time. Of course, such a choice does not provide the ability to observe effects that are inherently three-dimensional, such as, for example, tilting the axes of a solenoid or changing its shape along the circumference. Since these effects were not significant or relevant at the stage of this thesis work, the choice to focus on axisymmetric analysis was appropriate.
The next step is the generation of the geometry of one cell. In the 2D axisymmetric view

the solenoids are represented by rectangles. They are visible in Fig 4.4 in dark grey with their axis oriented vertically on the left. The light grey region is the background air. The shape of the background air depends on the kind of simulation which has to be carried out. In the case of a "periodic" simulation (which will be explained in the next section), the upper and lower boundaries align precisely with the start and end of the cell. On the other hand, in a "single cell" simulation (will be also described in the next section), the boundaries are slightly larger in size. On the right side (opposite to the axis), however, the air domain extends significantly to allow the calculation of stray fields.

The *Magnetic Fields* modulus focuses on the magnetic aspect. It is worth noting that Comsol utilizes the vector potential as its primary unknown variable. To calculate the magnetic flux density, it employs the relationship

$$\boldsymbol{B} = \nabla \times \boldsymbol{A}. \tag{4.26}$$

In this modulus, the rectangles created in the geometry can be energized and transformed into actual coils with a current density flowing through them. The "Coil" feature allows the coils to be more than just large conductors; they can be composed of multiple turns. This aspect will be important for evaluating the self and mutual inductances. Specific boundaries conditions are required for the magnetic field. I have employed two types of boundary conditions depending on the aforementioned two types of simulations. In general, the outer air domain, such as in the case of the "single cell" simulation, is always enclosed by the "magnetic insulation" boundary condition ($\boldsymbol{n} \times \boldsymbol{A} = 0$). Since magnetic field lines extend infinitely in space and require infinite space to close on themselves, the magnetic insulation boundary condition ensures that the field lines close on the specified boundary. This condition, in combination with an infinite domain layer (a numerical layer that emulates the boundlessness of space), allows for an accurate representation of magnetic field behavior in a finite simulation. In contrast, in the case of a "periodic" simulation, periodic boundary conditions have been employed on the upper and lower boundaries. These boundaries are the interface surfaces between the preceding and subsequent cells. The periodic boundary condition ensures that the vector potential is the same on those two boundaries. In mathematical terms, the vector potential field is periodic with a period given by the length of the cell

$$\boldsymbol{A}(r, z) = \boldsymbol{A}(r, z + L_{cell}). \tag{4.27}$$

The *Solid Mechanics* modulus focuses on the structural analysis. The simulation is performed using linear assumptions, considering linear material properties and behavior. The

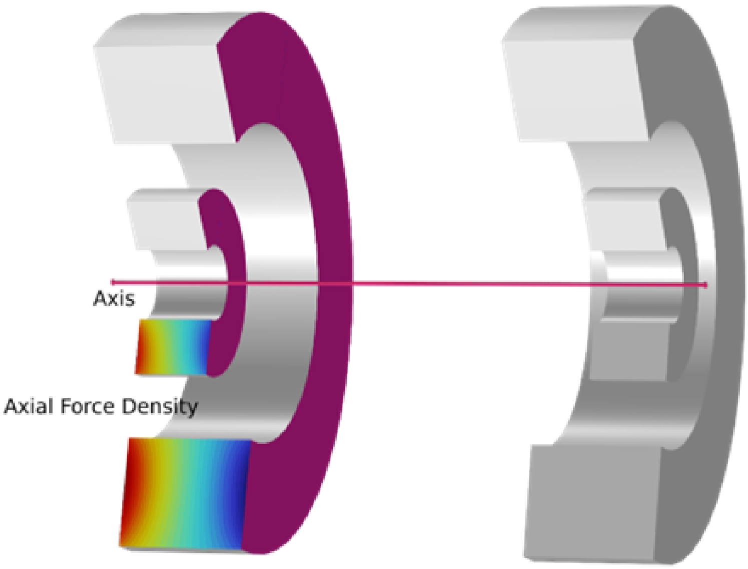

Figure 4.5: 3D representation of solenoids within a cell. The highlighted purple face indicates the location where the roller boundary condition is applied. The color scale on the cross section indicates the axial force density distribution.

coils in the simulation are composed of homogeneous copper. While copper may not represent the exact material used in real HTS tapes (where copper is just one of several layers), for the purpose of evaluating the stress state (which is of interest), the mechanical properties of the material have a negligible influence. Now, the force density field is applied to the coils. When both the magnetic field and structural analysis modules are active, the software automatically recognizes the potential interaction between them. It then suggests the Lorentz force as a possible force density source for the user. This allows for the consideration of the electromagnetic forces that arise due to the interaction between the magnetic field and the conducting material in the structural analysis. The default boundary condition used is called "free". This boundary condition imposes no constraints or loads on the surfaces, allowing for unrestricted displacement and stress distribution. All the solenoid's surfaces are free to move except one. On this face a "roller" boundary condition is used. The roller condition ($\boldsymbol{u} \cdot \boldsymbol{n} = 0$) prevents any displacement along the direction perpendicular to the surface on which it is applied. The specific face that is fixed by this constraint depends on the type of simulation and the particular cell being evaluated. However, as a general rule, it is positioned in a way that opposes the net axial force exerted on the solenoid. By fixing this face, the applied roller constraint helps to balance and counteract the axial forces experienced by the solenoid during the simulation. In the given example shown in Figure 4.5, the positioning of the roller boundary condition indicates that the axial forces exerted by the solenoids on the right side (displayed) are evidently greater than those generated by the solenoids on the left side (not displayed).

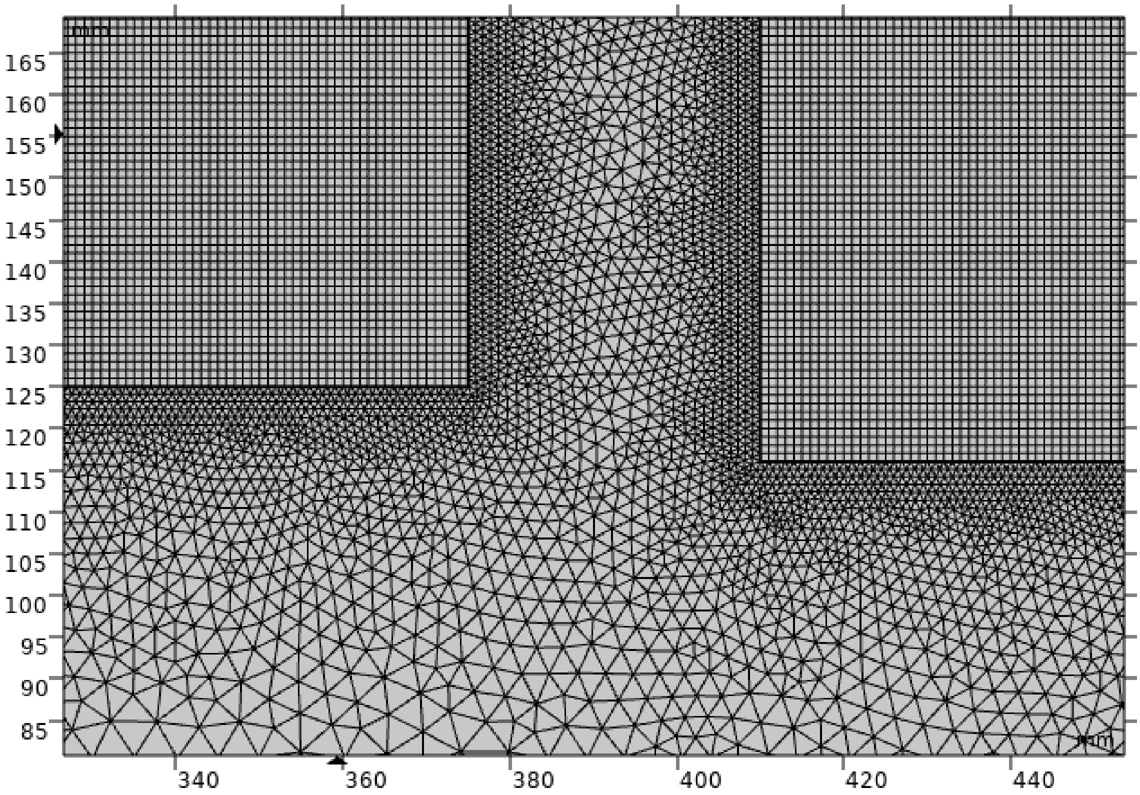

Figure 4.6: Detail of the mesh.

The mesh is generated automatically by Comsol. However, the user can intervene in the generation process to personalize the result. In particular, two of the most effective actions that can be performed are changing the maximum size of each element and modifying its shape. For example, as shown in Figure 4.6, the coils (rectangular regions) were meshed with a structured quadrilateral mesh ("mapped"), while the air domain with an unstructured triangular mesh ("free triangular"). Each component has its own maximum element dimension, and the software automatically meshes the interface regions, gradually adjusting the sizes. The coil regions are characterized by a 1 mm mesh, while the air domain has a maximum 5 mm mesh. These sizes have been chosen after conducting a preliminary study on the convergence of the final result in relation to the mesh size. Actually, the aforementioned dimensions are even smaller than the required dimensions. Regarding the solver settings, it is worth mentioning that no changes have been made compared to the default Comsol settings, except for the modification of the tolerance to 10^{-5}.

4.2. Results

The following two sections summarize one of the two main results of my entire thesis work (the other will be presented in Chapter 5).

In the 6D Cooling of the Muon Collider, there are a total of 12 different stages and 18 different types of solenoids. In our coil-naming convention, each unique coil from a cell is identified. For example, stage A1 has 4 coils which are all the same, so one unique coil is denoted as A1-1. Cell B4, instead, has 4 solenoids that are equal two by two. B4-1 is the "inner" solenoid while B4-2 is the "outer" (see Fig 4.4 for clarity). The objective

Parameters

Magnet	Bore Radius [mm]	Thickness [mm]	Length [mm]	Current Density [A/mm^2]	Cell Length [m]
A1-1	450	100	210	63.25	2
A2-1	410	130	260	126.6	1.32
A3-1	270	110	110	165	1
A4-1	220	140	90	195	0.8
B1-1	770	150	500	69.8	2.75
B2-1	500	150	360	90	2
B3-1	410	150	370	123	1.5
B4-1	175	200	92	94	1.27
B4-2	410	240	320	70.3	
B5-1	113	88	100	157	0.806
B5-2	217	165	196	168	
B6-1	84	92	100	185	0.806
B6-2	215	160	177	155.1	
B7-1	50	74	100	198	0.806
B7-2	210	145	170	155	
B8-1	45	65	120	220	0.806
B8-2	140	80	80	135	
B8-3	250	120	100	153	

Table 4.1: Geometrical parameters and current density of all the stages of the 6D Cooling

of this work was to characterize each stage and solenoid in terms of their magnetic and mechanical properties. Each stage has been studied in two different configurations: the first one considers just a single cell as stand-alone ("single cell"), while the other, which is more realistic, considers the cell as part of an infinite lattice of identical cells ("periodic"). The periodic simulation is representative of the inner cells of a real periodic lattice. Indeed, the fact that the real lattice is not infinite but has a starting and ending point spoils the perfect periodic symmetry. Conversely, the usefulness of the single cell simulation is twofold. On the road that leads to the final construction of the Muon Collider, there will be at least two demonstrators (at the time of writing) that are standalone cells without the lattice. Secondly, the final and initial cells of a lattice share properties that are common (a sort of superposition) with both the single cell and periodic simulations. As an initial disclaimer, it is important to note that this work involved evaluating the performance of an already existing design, namely the US MAP design of the Muon Collider. It should be emphasized that, at the time of writing this thesis, no optimization stage has been initiated.

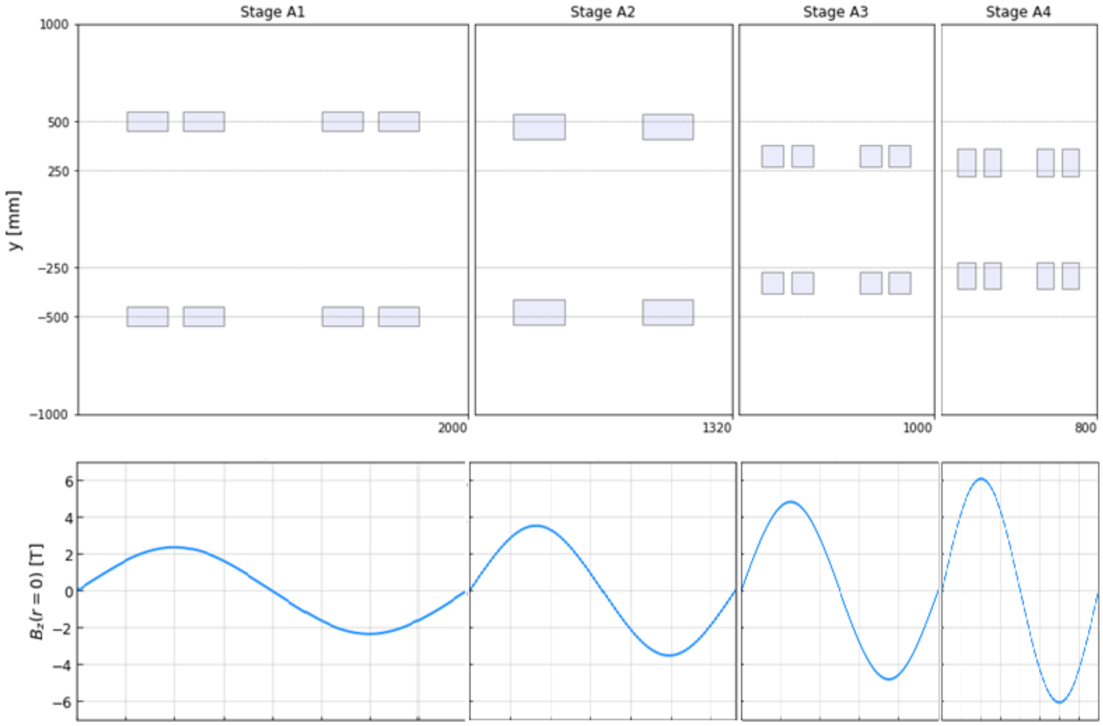

Figure 4.7: 2D axisymmetric cross section of stages from A1 to A4. Below the corresponding magnetic field. z axis in [mm]. Image courtesy of Siara S. Fabbri (CERN).

It is interesting to show the parameters of the stages before looking at the results. Table 4.1 summarizes all the geometrical parameters (plus the current density) of the cells from A1 to B8. Figure 4.7 shows, as an example, the cross sections of first four stages and below the profile of their magnetic fields. I will take advantage of Figure 4.7 to highlight that the solenoids of stages A1, A3 and A4 are split to allow the waveguides to reach the RF cavities.

4.2.1. Case Study: Cell A1

To better understand the results of all the solenoids together, it is worth considering a case study. The chosen case study, Cell A1, was selected because it is representative of the majority of the cells. See Table 4.1 for its properties.

The first aspects to be considered are the magnetic field and the magnetic properties. In Figure 5.6b, the modules of two magnetic fields are shown. The left side represents the magnetic field of the single cell, while the right side corresponds to the periodic simulation. The aim of this figure is not to depict the magnetic field in terms of its magnitude but rather to illustrate the different symmetries between the two configurations. The single cell has a symmetry plane which passes through the middle of the cell . It is a pure specular symmetry in terms of the magnitude of the field while it becomes an anti-symmetry if one considers other quantities like the axial component of the field. On the other side, the periodic simulation shows an additional degree of order. There is another symmetry plane which passes at one-fourth (and correspondingly at three-fourth) of the length of the cell. Anyway, this aspect is not general and regards just those stages where the centers of the solenoids correspond to one-fourth and three-fourth of the cell.

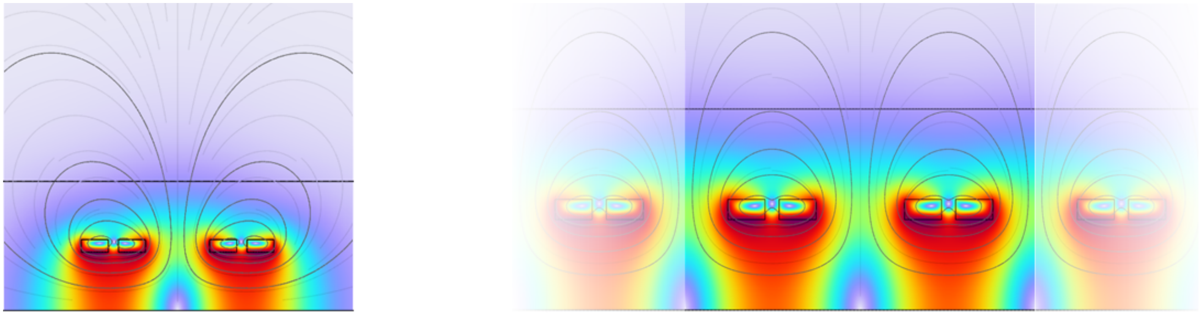

Figure 4.8: Module of the magnetic field of cell A1 for the single cell (on the left) and the periodic (on the right).

Figures 4.9 show the behaviour of the axial component of the magnetic field (B_z) in some interesting directions. The lines on which the plots are evaluated are indicated by the boxed regions above each corresponding plot. The first plot shows the axial magnetic field on-axis. It is evident the sinusoidal profile given by the opposite polarity magnets. The blue and the light blue lines represent, respectively, the result of the single cell and the periodic simulation. The differences between the two configurations are evident: in the single cell case, the magnetic field is consistently higher in value throughout the cell, and it does not reach zero at the beginning and end of it. Here, a couple of considerations can be done. The reason for the disparity between the two fields lies in the presence of solenoids with opposite polarities on the left side of the left solenoids and the right side of the right solenoids in the periodic cell. These solenoids counteract each other, resulting

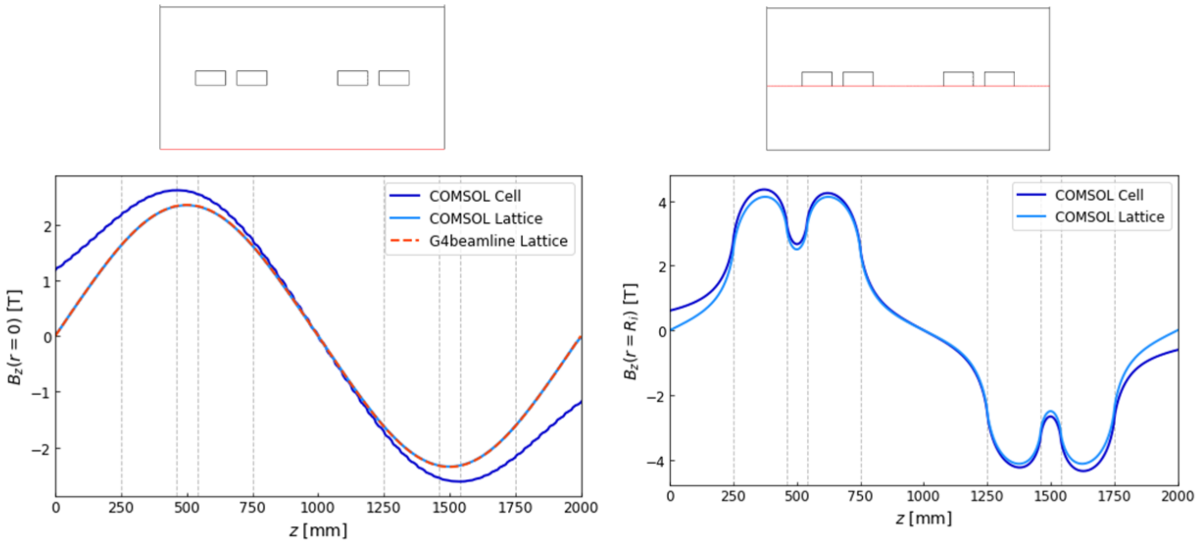

(a) On the left: B_z along the axis, on the right: B_z along the inner radius of the solenoids.

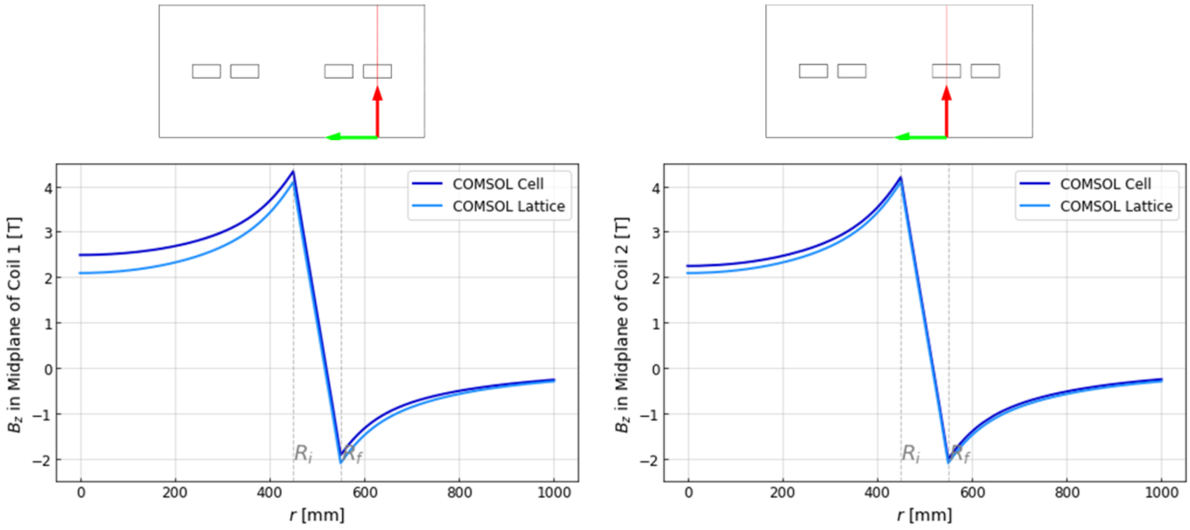

(b) On the left: B_z along the mid-plane of solenoid 1, on the right: B_z along the mid-plane of solenoid 2.

Figure 4.9: Axial component of the magnetic field along specific lines. R_i and R_f are, respectively, the inner and the outer radii.

in a decrease in the magnetic field within those regions. Indeed, in the region where the influence of additional magnets, relative to those already present in the cell under evaluation (i.e., the center of the cell), is minimal, the difference in magnetic fields is also minimal. The fact that the magnetic field in the single cell case does not reach zero at the external boundaries of the cell is perfectly natural. The magnetic field is not influenced by artificial dimensions such as the length of the cell to determine where it should reach zero. Instead, the reason why in the periodic case the field goes to zero in those locations is intimately related to the lattice structure and hence to its periodic symmetry. If the field has to be the same at the beginning of the cell and at its end, there is no other possibility, given the opposite polarity of the solenoids, for it to be zero there. The right plot in Figure 4.9a shows the axial field along an axial line which is at the same position than the inner radius of the solenoids. Knowing the field at the inner radius of a solenoid is of capital importance because the maximum value of the magnetic field is expected to occur at that location. As we move away from the axis, we can observe that the magnetic field deviates from the "smooth" sinusoidal profile and, more importantly, it increases significantly. The red dashed line labelled with "G4beamline Lattice" in (a) is the field map supplied by Diktys Stratakis from the US MAP Study, which served as a useful validation test for our fields. Figures 4.9b show the same effect but looking at the field along the radial direction and on the mid-plane of the magnets. From this perspective, it becomes clear that the magnetic field starts from a certain value on the axis, increases as it approaches the conductor, then decreases (almost) linearly inside the conductor until it reaches a negative value. Finally, it gradually increases asymptotically back to zero.

The inductance was calculated using Eq (4.9) in Subsection 4.1.1, and its accuracy was verified by comparing it with the value obtained from the Comsol simulation. The value of the inductance, as indicated by the formula, is primarily influenced by the geometrical configuration of the magnet. However, it is important to note that for the same configuration, the inductance heavily depends on the number of turns ($\sim N^2$) that comprise it. Generating the solenoid through a generic HTS ReBCO cable with dimension 12 mm × 0.11 mm, we get 329.9 H. Normalizing this value to the number of turns squared ($\sim 15900^2$), it becomes 1.3 μH. The matrix of the self and mutual inductances is

$$\underline{\underline{L}} = \begin{bmatrix} 329.91 & 128.41 & 18.48 & 10.98 \\ 128.41 & 329.91 & 36.27 & 18.48 \\ 18.48 & 36.27 & 329.91 & 128.41 \\ 10.98 & 18.48 & 128.41 & 329.91 \end{bmatrix} \tag{4.28}$$

On the diagonal there are the self inductances of the four solenoids (they are exactly the same because the solenoids are the same) while on the off-diagonal terms there are all the mutual inductances. The matrix exhibits a peculiar mathematical behavior: it is simultaneously symmetric (a symmetric matrix is a square matrix that is equal to its transpose), centrosymmetric (symmetric with respect to its center), and persymmetric (symmetric with respect to the second diagonal)(there exists a theorem which states that if a matrix satisfies at least two of these properties, it must also satisfy the third). The first row is a representation of the self inductance of the first solenoid on the left (329.91 H), the mutual inductance between itself and its dual split coil (128.41 H) and the two mutual inductances with the opposite polarity solenoids on the right (18.48 H and 10.98 H, respectively). Using Eq (4.15), the magnetic energy stored in the "single cell" case is calculated to be 5.807 MJ, while in the "periodic" case, it is 5.382 MJ. This difference accounts for the lower field observed in the periodic configuration.

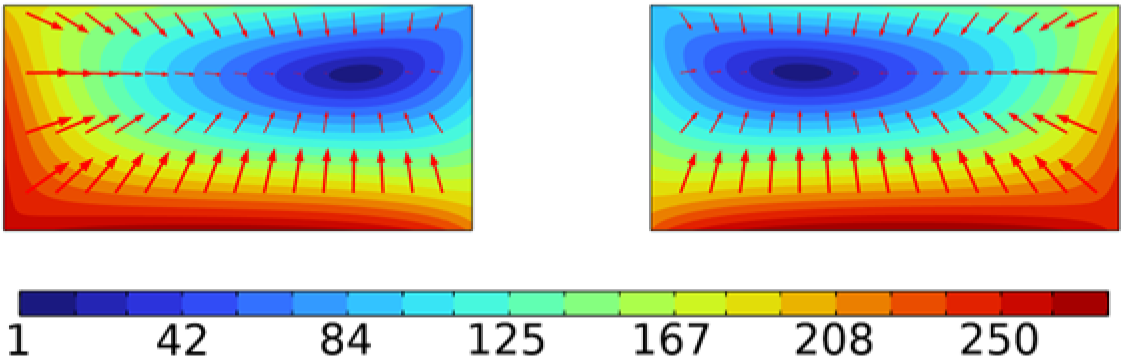

Figure 4.10: Magnitude and vectorial direction of the force density inside the two split coils in the "single cell" simulations. Legend in [MN/m^3].

Now let us shift our focus to the mechanical analysis. The first aspect to address is the positioning of the roller boundary conditions. In the case of cell A1, they are positioned on the opposing faces of the split solenoids for both simulations. Evidently, in both configurations, the attractive forces between the two split coils with the same polarity outweigh the repulsive forces with the other solenoids. This is evident in Fig 4.10: it can be visually estimated that integrating the force density results in a net force that tends to attract the two coils. This intuition is validated by the actual integration: the left solenoid is pushed towards the other with an axial force of 4.23 MN, and vice versa, the right solenoid experiences a force of 2.91 MN pushing it towards the left solenoid. The former being higher because in the "single cell" case the magnetic field is higher on the first magnet. Instead, the "periodic" case they attract each other with the same (but opposite) force of 3.80 MN.

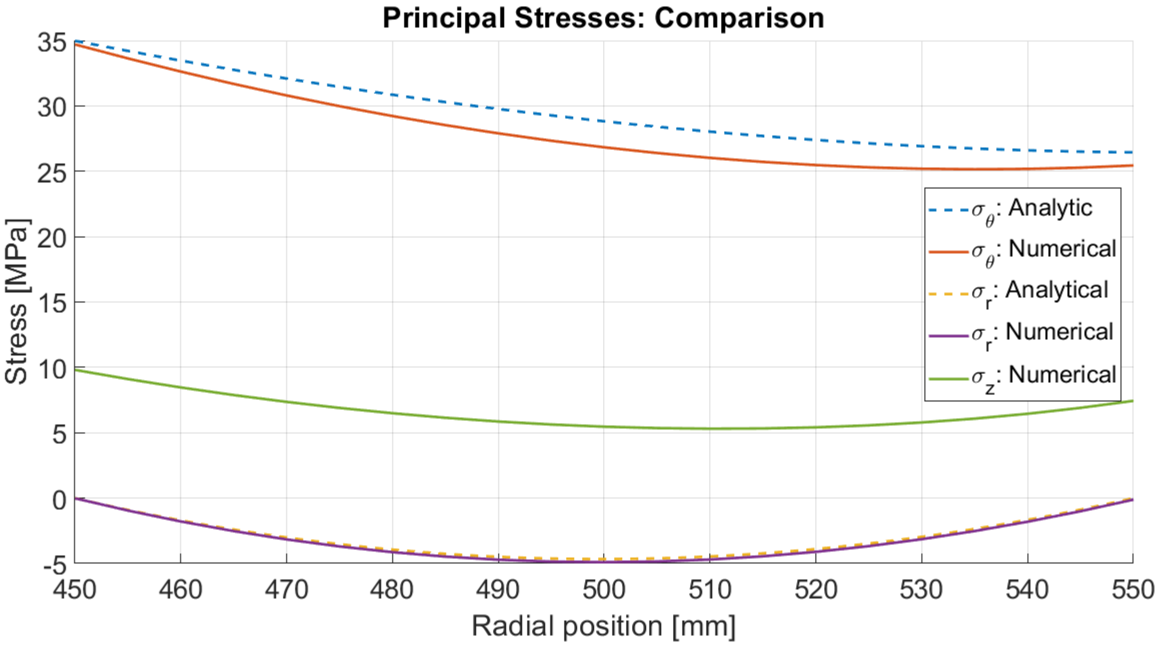

Figure 4.11: Comparison between the analytical formulas and the numerical result in Comsol of the stress state.

This force density distribution, together with the choice of the boundary conditions, results in the stress state of Figures 4.12. These results pertain to the "periodic" simulation, but they exhibit a substantial similarity with the "single cell" configuration as well. They represent the stress state one should expect from a solenoid. The hoop stress starts from a maximum value at the inner radius and then decreases. The 2D map clearly indicates that, in the majority of the cross-section, the profile exhibits a minimum that is attained towards the outer region of the coil. The radial stress is uniformly compressive throughout the entire cross-section, starting from zero at both the inner and outer radii, as it should be. Similarly, the axial stress state is entirely compressive. This outcome is not surprising when considering the chosen boundary conditions. Indeed, the positioning of the rollers is specifically chosen for them to work under compression rather than tension. However, it is important to note that while the choice of the roller boundary condition may be reasonable for a preliminary evaluation, it should be replaced by a comprehensive mechanical structure for a more accurate assessment.

Figure 4.11 depicts a comparison between the results obtained using the analytical formulas (Eqs (4.24)) and the numerical approach with Comsol. The analytical formula fails to properly evaluate the hoop stress and, in particular, although it hits the right maximum value, it then overestimates the stress in the remaining part of the domain. Conversely, it behaves reasonably well in predicting the radial stress. It is worth emphasizing that this is a good result considering the various assumptions and approximations made during the derivation of these formulas. It is also true that, as we move towards more intricate geometries (such as those found in stage B4 and beyond), the discrepancies in behavior become increasingly significant.

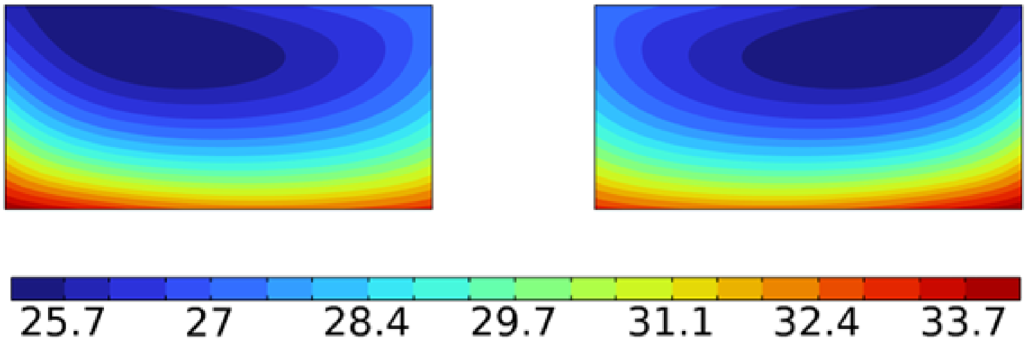

(a) 2D hoop stress.

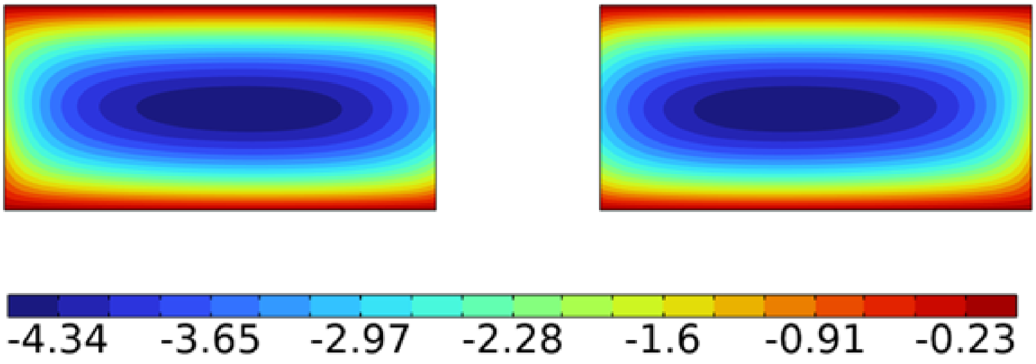

(b) 2D radial stress.

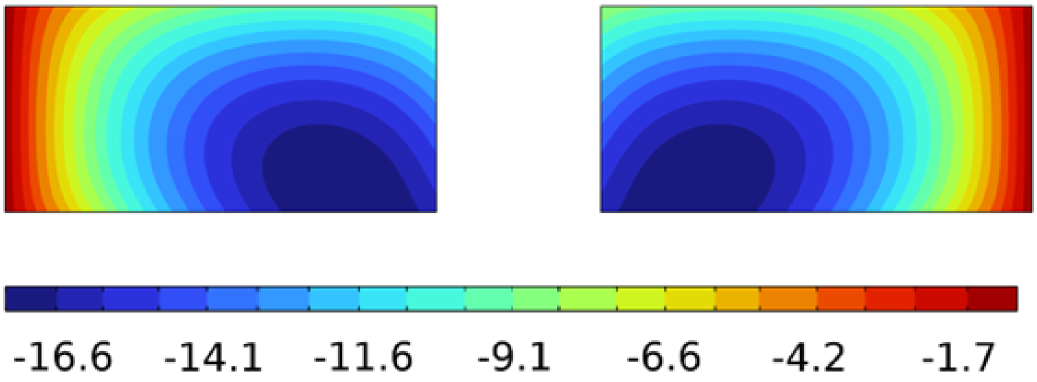

(c) 2D axial stress.

Figure 4.12: Stress state of cell A1 from Comsol simulation "periodic". Legends in [MPa].

4.2.2. Characterization of all the Stages

Now that all the utilized analytical and numerical instruments have been presented and discussed and a real case study has been analyzed in-depth, we are equipped to examine

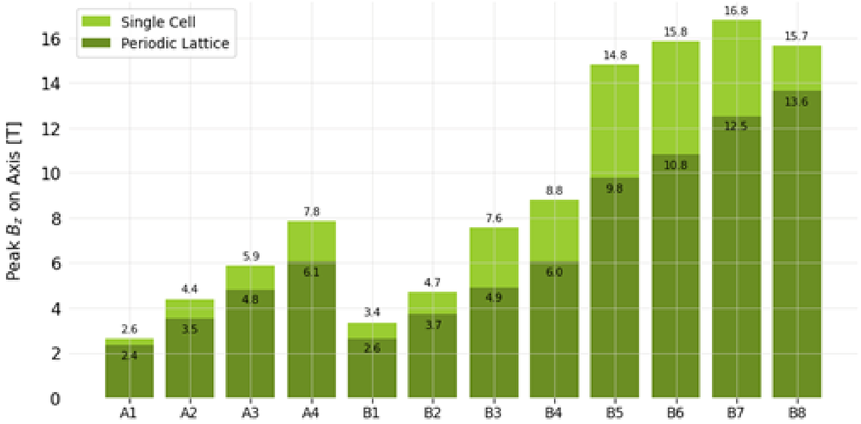

(a) Maximum value of B_z on axis.

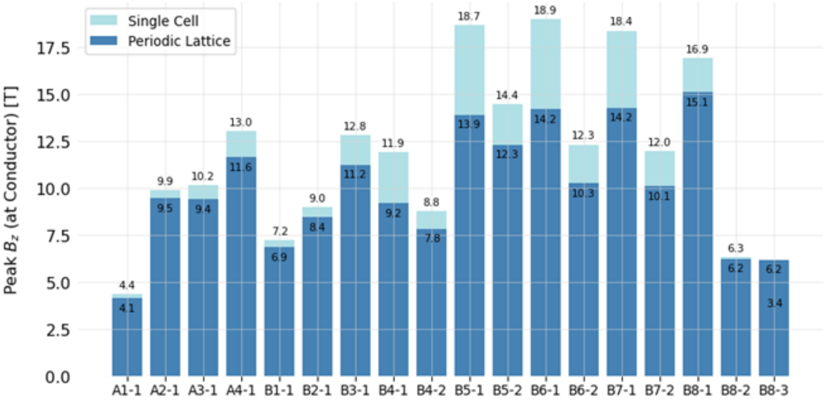

(b) Maximum value of B_z in the coil.

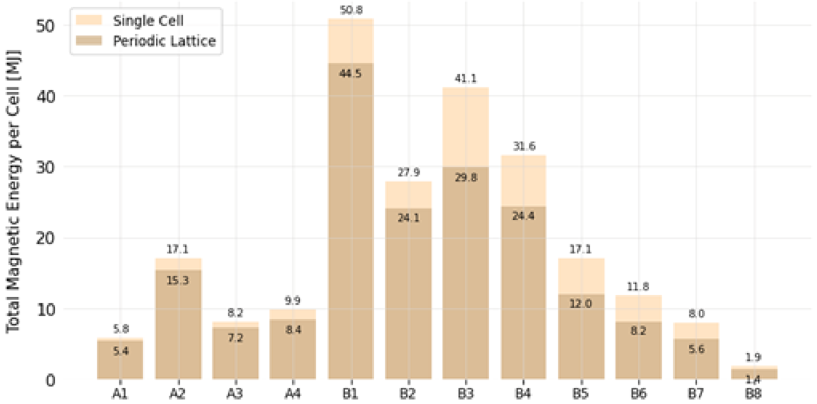

(c) Stored magnetic energy per cell.

Figure 4.13: Comparison of magnetic properties between "single cell" and "periodic".

all the magnetic and mechanical parameters which characterize the 6D Cooling of the Muon Collider. This analysis assumes particular significance as it provides a comprehensive estimation of the characteristics of all the magnets involved, thereby serving as a valuable tool for evaluating the challenges that lie ahead in the future. It is useful to remind that some of the characteristics and results shown in Figures 4.13 to Figures 4.15 are not the final outcomes, but serve as a starting point for future developments and optimizations. For example, the current densities used by the US MAP study range from more that 60 A/mm^2 up to 220 A/mm^2. Nowadays, there are second-generation HTS cables which can carry (at 20 K and a background field of 15 T) up to 600 A/mm^2. It is clear that to fully exploit the capabilities of these new cables, the design must change accordingly. In Fig 4.13a we can appreciate the profile of the maximum magnetic field on-axis going through all the cooling stages. The maximum field is 2.4 T in cell A1 and reaches 13.6 T in B8. Anyway, for a magnet designer, more important information is found in Figure 4.13b. From the perspective of the superconductor, the on-axis field is not as crucial. Conversely, what truly matters is the local magnetic field it experiences.

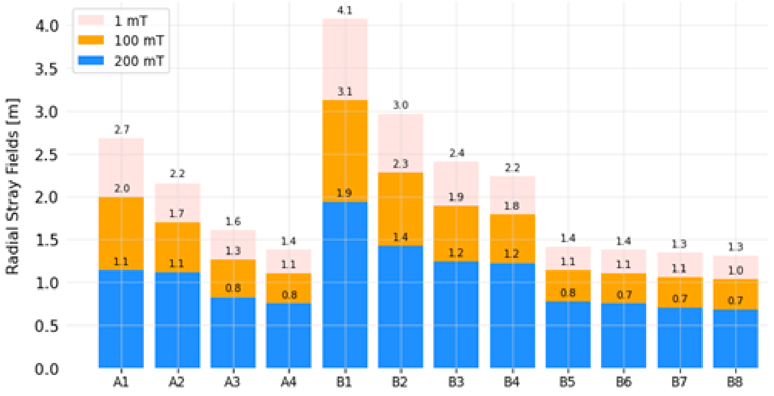

(a) "Periodic" simulation.

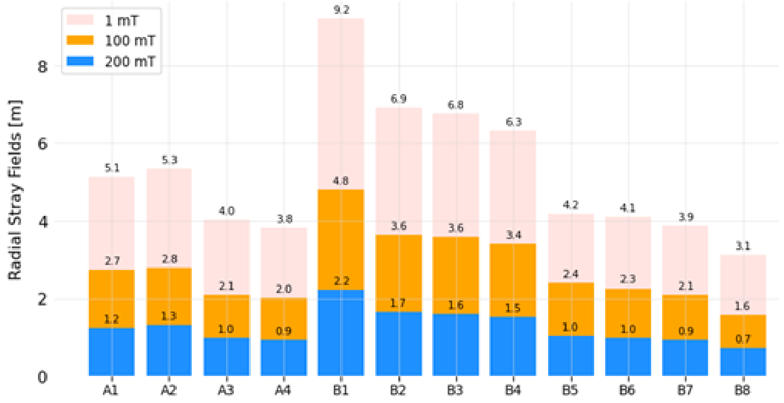

(b) "Single cell" simulation.

Figure 4.14: Stray fields.

Different superconductors (NbTi, Nb_3Sn, ReBCO HTS etc) behave differently if subjected to a given magnetic field. Specifically, Nb_3Sn and ReBCO HTS tapes are better suited for high background fields. As a result, the most heavily loaded cells, starting from B4 and onwards, will definitely depend on one of these two technologies. When examining the previous two plots together, it becomes evident the difference between the field on-axis and the corresponding field on the conductor. Cell B1, which has the largest bore radius (770 mm), has a conductor-to-on-axis field ratio of 2.6. What is not dependent, at first approximation, on the tape technology is the stored magnetic energy. The evaluated values are provided in Figure 4.13c and can be considered high, especially from the perspective of quench protection. As a reference, an LHC dipole, which is 15 m long and generates a field greater than 8 T, stores approximately 7 MJ of energy.
The last magnetic consideration is about stray fields. Every magnet used in accelerator technology must adhere to regulations governing exposure to static magnetic fields. For instance, the "Safety Rules for the Use of Static Magnetic Fields at CERN"[13] imposes the safety limit for the magnetic field at which a technician can be exposed to 200 mT. Additionally, it is worth mentioning that certain instruments perform poorly in high magnetic fields. Turbo-pumps, for example, struggle to operate effectively in an environment with magnetic fields exceeding 5/10 mT. Figures 4.14 show the radial distances at which some specific values (1, 100 and 200 mT) are attained. It is very interesting to notice that the periodic structure is able to halve these distances having then a beneficial effect.

Figures 4.15 provide an illustration of some of the mechanical calculations that have been conducted. The top plot displays the maximum (in pink) and minimum (in purple) hoop stresses of each coil. These stresses are relatively high but can be managed with a suitable mechanical structure. As a general rule, when the stress exceeds 150 MPa, a solenoid requires reinforcement, while coils made of HTS can withstand stresses up to 500/600 MPa. The most critical aspect relates to the radial stress. As shown in Figure 4.15b, some coils exhibit a purely compressive profile, while others demonstrate a mixed (mostly tensile) state. These coils behave in this manner not by chance. They correspond to the smallest bore solenoids within the "multi-bore" stages (starting from B4). These solenoids face two unfavorable conditions: a large α value (outer-to-inner radius ratio) and a κ value greater than zero (the ratio between the outer and inner magnetic field). These conditions make the design of these solenoids challenging. To ensure a negative or slightly positive radial stress state, several strategies can be implemented. Firstly, pre-tensioning the tape during winding can be employed. The second strategy is to wrap the outermost layer of the coil with a high modulus of elasticity bending wire. Lastly, subdividing the magnet into mechanically independent radial sections can be effective in reducing the α value. By

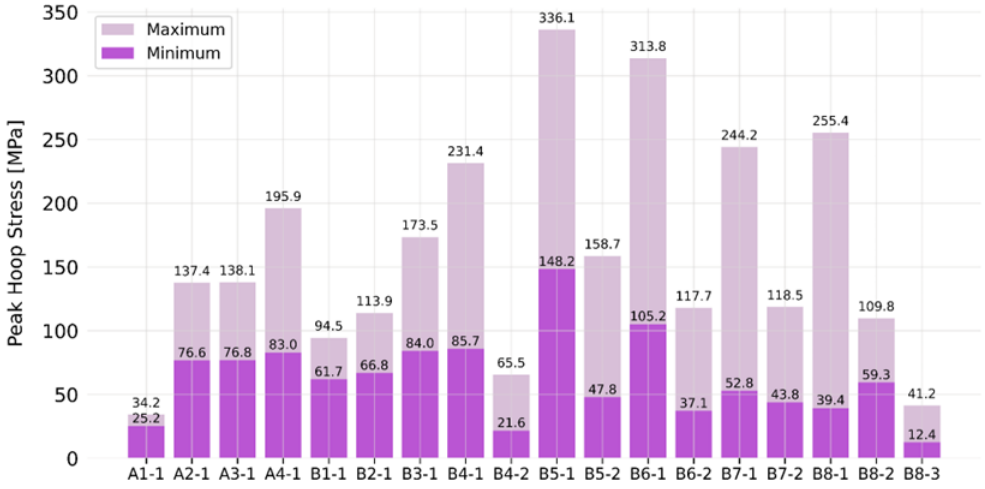

(a) Hoop stresses.

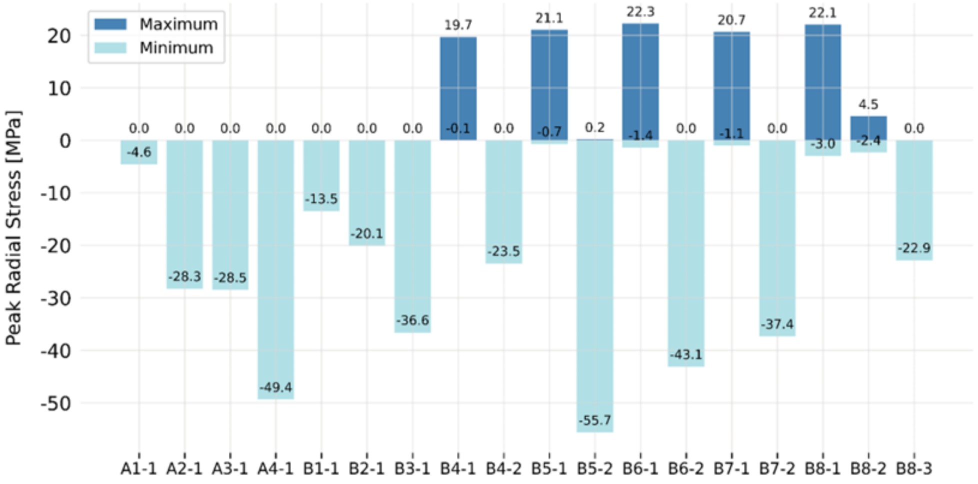

(b) Radial stresses.

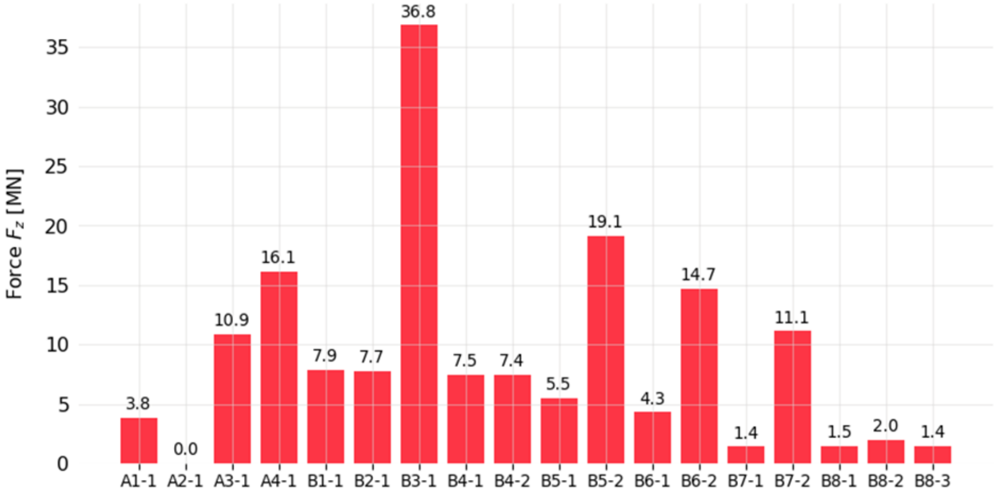

(c) Axial net force on coil.

Figure 4.15: Mechanical calculation of the "periodic" simulation.

dividing the magnet into multiple sections, the outer-to-inner radius ratio is decreased, leading to a more favorable stress distribution. These strategies, as described in [22], can be utilized to mitigate the compressive stress conditions and achieve a more desirable stress state within the solenoid. Figure 4.15c displays the axial net forces exerted on each magnet. Certain solenoids, such as those in cell B3, experience notably high lateral forces, necessitating complex mechanical structures to withstand them.

5 | The Quench Protection

The *quench* is Achilles' heel of superconductivity and, in particular, of superconducting magnets. It reminds us that, while we are granted this tremendous power, Nature withholds at least some control over it.
In this chapter, I will first explain what a quench is from a phenomenological point of view, introducing analytical formulas where possible, and then present the finite element method (FEM) simulation I created and the corresponding results. The quench protection of the Muon Collider solenoids poses a significant technical challenge, necessitating innovative solutions, particularly in situations where the non-insulated winding technique will be employed. While this is only a preliminary approach, it can still offer valuable insights in the field.

5.1. What is a Quench

5.1.1. Phenomenology

A quench is a transition from a superconducting to a normal resistive state [22]. This transition, within a superconducting cable, cannot go unnoticed, as both the current density and the resistance in the normal state are large. The current density is high due to the superconductor's capacity to carry substantial currents without difficulty. Conversely, its resistance becomes extremely high after the transition, owing to the inherent nature of the superconducting phenomenon (as explained in Chapter 2). The superconductor goes from being an exceptional conductor which carries electricity with virtually zero resistance to a state comparable to that of an insulator. This is why it is always accompanied by a metal stabilizer such as copper, which temporarily takes over the current-carrying role. However, if copper were capable of fulfilling this role as effectively as the superconductor, we would not be discussing about superconducting magnets. Indeed, the high current and the relative high (with respect to what before was a superconductor) resistivity generates an intense local Joule heating which takes the quench point and its surrounding region to temperatures which, if no protection mechanism is activated, can reach easily the melting

point of all the materials inside the cable. In this process the stored magnetic energy of the magnet and the power provided by the electric supply are converted into heat in a percentage that can range from few points up to its totality [10].
The quench phenomenon is quite complex as it is inherently a multiphysics event. By examining it from its initial occurrence to the implemented actions to mitigate it, we can truly appreciate the involved complexity. First of all we shall discuss the causes which are able to initiate a quench.

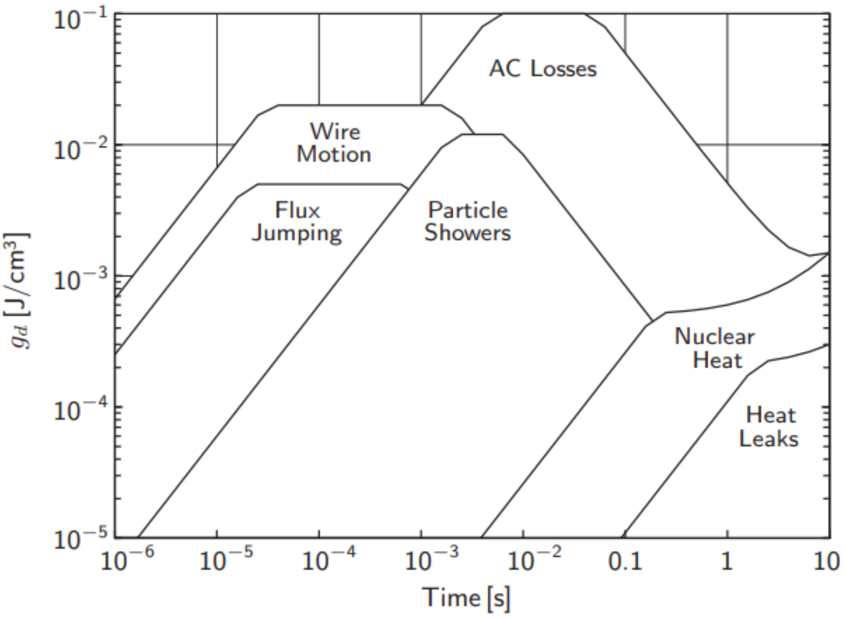

Figure 5.1: Disturbance Spectra of LTS. The term $g_d(t)$ is the heating density caused by a potential disturbance in an LTS winding. Image from [22].

During the first experiences in the construction of superconducting magnets, it became evident that a quench is initiated by a release of energy within the magnet windings. Due to the wide range of potential events which can cause it, the concept of disturbance spectrum emerged. The events can be distinguished by their temporal and spatial extent: we could have a point or distributed disturbance in space and a transient or continuous disturbance in time. A transient event is expressed in Joules (J) if localized in space (point) or in J/m^3 if distributed, while a continuous event is expressed, respectively in Watts (W) or W/m^3. An example of a point transient event is the sudden release of mechanical energy caused by a conductor slippage (wire motion). Conversely, AC losses are representation of a continuous and distributed event. Other causes are shown in Figure 5.1. These spectra are primarily generated for LTS magnets but can also be somewhat applicable for describing HTS as well.

Once the process has been initialized, a thermal transient will start. In the next section a rigorous description will be given, while here a more qualitative approach is more useful. Each disturbance in Fig 5.1 contributes a power term within the differential equation that describes the thermal behaviour of the conductor. For instance, let us examine the consequences of a localized transient disturbance. Locally, the temperature rises at a rate determined by the specific time profile of the source term and the specific heat of the conductor. If the magnet is well-designed, the conductor operates with a certain safety margin, allowing for a slight increase in temperature without any visible effect. Nevertheless, something significant is occurring. Each layer within a superconducting cable (or tape in the case of HTS) has its unique electrical resistivity, which is an increasing function of temperature. Under standard operating conditions, the resistivity of the superconductor is several orders of magnitude smaller than that of any other material, resulting in the majority of the current flowing through it. However, as the temperature increases, this hierarchy can change. A superconductor can endure a change in temperature until it reaches a threshold known as the *current-sharing* temperature. Beyond this point, the critical current at that temperature (under a specific magnetic field) becomes smaller than the current flowing through the conductor and consequently, as the name suggests, it begins to share a portion of this current with other materials, particularly copper.

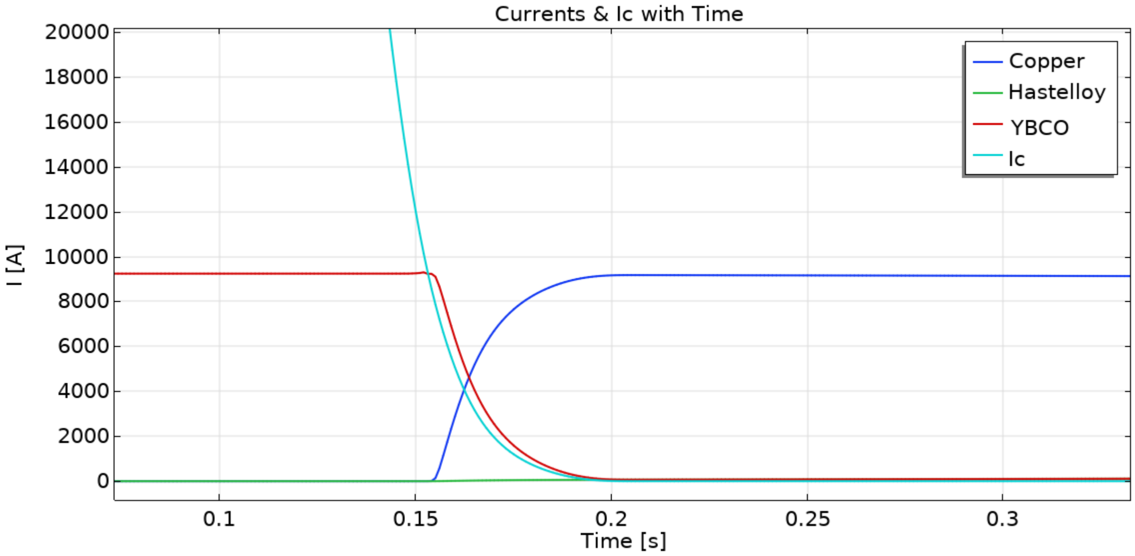

Figure 5.2: Evolution in time of the current inside each material as the temperature of the central point increases.

This process is illustrated in Figure 5.2. The light blue line represents the critical current curve of the YBCO in the simulation, while the red line depicts the actual current flowing through it. As time elapses and the temperature rises, the red line remains constant until the moment (around 0.15 s) when the superconductor begins to share the current. At approximately 0.20 s, the current flows entirely through copper (indicated by the blue line). During this transient the superconductor develops resistance and it produces some Joule heating. However, the primary contribution to the overall heating comes from copper. Copper, widely recognized as an excellent conductor at room temperature, performs even better at cryogenic temperatures. Nevertheless, it is unable to withstand the incredibly high current values encountered in these situations. As soon as current starts flowing through copper, it promptly initiates the production of Joule heating. This source term further contributes to the temperature increase, establishing a positive feedback loop. As temperature increases locally, conduction activates, enabling nearby regions to heat up and contribute to the overall process. The normal-conducting zone grows in size driven by the conduction of heat and guided by the increase of temperature which expands to the surrounding regions.

During this process there is not much we can do, except, once detected, turn off its driving source, the current (and hence the power supply). Ultimately, the fate of the magnet lies in the hands of the quench protection system. It must act promptly and reliably, ensuring that the temperature within the magnet does not exceed a predetermined safety threshold at any point.

We previously mentioned that the quench is a multiphysics event. However, our focus thus far has primarily been on describing the thermal aspects. It is worth taking a brief look at other phenomena related to different "physics". Indeed, the quench also leads to the appearance of a voltage in the magnet and in particular across the quenched region, and to a differential thermal expansion that, together with the electro-magnetic forces, induces a stress state inside the conductor. The thermal equations are, then, coupled with a set of differential equations describing the evolution of the currents and the voltages across the different parts of the system, from the magnet to the external electrical circuit. If one considers the relationship between the stress state and the conductive properties of the superconductor, it becomes evident that mechanical equations should be incorporated. It is worth emphasizing that special attention must also be given to the cooling, as the magnet is cooled by helium, which evolves following its state, mass, momentum and energy conservation equations. All these aspects must be taken into account when implementing mitigation strategies. For example, the generation of voltages in any part of the magnet or in the auxiliary external circuit could lead to excessive electrical stress or even arcing. During the quench transient the electromagnetic conditions within the whole system could change, leading to the development of thermal and electromagnetic forces which should be considered to avoid structural failure. The additional heat removal which is asked to the cooling system determines a cryogen pressure increase that has to be properly accommodated by venting lines and valves [10].

5.1.2. Governing Equations

As mentioned in the preceding section, the quench is an inherently intricate phenomenon that encompasses various branches of physics. Therefore, it can be effectively described by employing a complex system of coupled partial and total differential equations. The strategy I will adopt is as follows: I will initially present the equations in their complete and elegant form to grasp, from one side, the complexity of the phenomenon, and from the other side, to better understand the second step, which involves exploring the approximations and simplifications employed in practical applications.

The first equations are the heat diffusion equations. Strictly speaking, there is a diffusion equation for each layer i which composes the superconductor

$$C_i(T_i)\frac{\partial T_i}{\partial t} = \nabla \cdot [k_i(T_i)\nabla T_i] + \boldsymbol{J}_i \cdot \boldsymbol{E}_i + g_{d,i}(t) - g_{c,i}(t,T), \tag{5.1}$$

where $T_i = T_i(\boldsymbol{r}_i)$ is the temperature scalar field inside the material, $C_i(T)$ is its temperature dependant heat capacity and $k_i(T)$ the thermal conductivity. To accurately describe the conductive behavior of a material in different directions, the thermal conductivity k_i should be treated as a tensor. This allows for a comprehensive representation of how a conductor may exhibit distinct characteristics along various orientations. Actually, the thermal conductivity could be a more complicated function with several dependencies. The thermal behaviour of copper, for example, is influenced by the local value of the magnetic field. It is also common to include the Residual Resistance Ratio (RRR) as a parameter. The RRR is technically the ratio between the electrical resistivity at room temperature to that at (usually) 4.2 K, but it is used as a measure of the purity and the quality of the material. The lhs of the equation represents the time rate of change of the thermal energy density and is strictly related to the heat capacity and its temperature profile. It is useful to remind that Eq (5.1) is a balance equation and hence its rhs represents the reason why the thermal energy density varies in an infinitesimal portion of the material. The first of these causes is conduction. Heat flows from regions of higher temperature to cooler regions. If we concentrate on just the conduction term, temperature increases ($\partial T/\partial t > 0$) if the average temperature in the neighboring region is higher than the one inside the infinitesimal portion, and decreases ($\partial T/\partial t < 0$) if it is lower. The last three terms are the heat source or sink terms. The first of them is the Joule heating and can be also expressed as $\rho_i J^2$, where ρ, the electrical resistivity, can be a multi-parameter function depending on the material. This heating contribution comes from the microscopic interaction (collisions) between the charge carriers (the electrons) and elements of the conductor such as the phonons and the defects. The last two terms are, respectively, another heat source term and a cooling term. In particular, $g_{d,i}(t)$ represents any possible cause of quench initiation, like those depicted in Fig 5.1. Like any self-respecting time partial differential equation, Equation (5.1) should be adorned by an initial and boundary conditions. The initial condition is rather simple as it requires just to establish the temperature field in every point at the initial time t_0, $T = T(\boldsymbol{r}, t_0)\ \forall\ \boldsymbol{r} \in V$, with V being the volume of the domain. It is usual to consider a constant temperature throughout the whole volume. Before discussing boundary conditions, it is useful to remind that the coupling between adjacent layers (and consequently their respective temperature fields) is ensured by enforcing the continuity of the heat flux. The boundary conditions are notoriously three and they are

$$\text{1}^{\text{st}}\text{ kind:} \qquad t > 0 \wedge \boldsymbol{r} \in \partial V, \quad T = T(\boldsymbol{r}, t), \tag{5.2a}$$

$$\text{2}^{\text{nd}}\text{ kind:} \qquad t > 0 \wedge \boldsymbol{r} \in \partial V, \quad -k\frac{\partial T}{\partial r_i} n_i = q_n(t, \boldsymbol{r}), \tag{5.2b}$$

$$\text{3}^{\text{rd}}\text{ kind:} \qquad t > 0 \wedge \boldsymbol{r} \in \partial V, \quad -k\frac{\partial T}{\partial r_i} n_i = h\left[T(\boldsymbol{r}, t) - T_\infty\right]. \tag{5.2c}$$

In Eqs (5.2) ∂V is the domain boundary, T_∞ and h are, respectively, the bulk temperature of the cooling fluid and the heat transfer coefficient, and q_n the heat flux along the unit vector $\boldsymbol{n}$ perpendicular to the boundary (here i represents the three directions of a generic reference frame).

The equilibrium and conservation equations governing the cooling helium will not be discussed in this thesis work. This is because the FEM simulation, which will be presented in the next section, assumes an adiabatic magnet configuration without any active cooling mechanism.

On the other hand, it is crucial to accurately consider a set of equations for the electric circuit. If we collect the currents of all the coils in the system in the vector $\boldsymbol{I}$, then their evolution in time can be modeled by the following ordinary differential equations

$$\underline{\underline{L}} \cdot \frac{\mathrm{d}\boldsymbol{I}}{\mathrm{d}t} + \underline{\underline{R}} \cdot \boldsymbol{I} = \boldsymbol{V}, \tag{5.3}$$

where $\underline{\underline{L}}$ and $\underline{\underline{R}}$ are the matrices of inductances (and mutual inductances) and resistances of the circuit, and $\boldsymbol{V}$ the voltage sources provided by the power supplies [10]. Eq (5.3) is more complicated than it may seem at first glance. First of all, the resistance matrix $\underline{\underline{R}}$ contains non-linear terms (the time-dependant quench resistances). Similarly, the voltage sources $\boldsymbol{V}$ can also exhibit non-linear behavior if non-linear components such as diodes are present. Furthermore, the complexity of the system can be further amplified by the presence of switches, which have the ability to completely alter the circuit's topology.

5.1.3. Simplified Equations

Due to the high non-linear behaviour, the analytical treatment of the equations presented in the previous section is impossible and no closed-form solution can be found. One has to rely on simplified equations and approximations. A practical strategy involves decomposing the problem into several smaller, more manageable problems. By collecting and combining the solutions, a better understanding of the original problem can be obtained. This approach gives rise to the definition of various concepts such as the Minimum Propagating Zone (MPZ), stability margin, and many others.

The first approximation that can be made is to declassify Eq (5.1) to a one-dimensional problem. This simplification is reasonable considering that magnet cables are typically kilometers long, while their cross-sectional areas are only a few squared millimeters. By treating the problem as one-dimensional, we can focus on the temperature variation along the length of the cable while assuming that it remains relatively constant across the cable's cross section. Another time-saving action is to homogenize the conductor. Instead of considering each individual layer of a tape separately, they are treated as a single homogeneous material. This simplification allows us to characterize the overall properties of the conductor by taking a weighted average of the properties of the individual layers

$$\bar{C} = \sum_i f_i \gamma_i c_i, \tag{5.4a}$$

$$\bar{k} = \sum_i f_i k_i, \tag{5.4b}$$

$$\frac{1}{\bar{\rho}} = \sum_i \frac{f_i}{\rho_i}, \tag{5.4c}$$

where γ_i are the densities and f_i the volumetric ratios $f_i = V_i/V_{tot}$. The 1D homogenized equation now reads

$$A\bar{C}\frac{\partial T}{\partial t} = \frac{\partial}{\partial x}\left(A\bar{k}\frac{\partial T}{\partial x}\right) + A\bar{\rho}J^2 + Ag_d(t) \tag{5.5}$$

with A being the tape's cross sectional area. This equation is still highly non-linear since all the homogenized material properties depend on temperature.

Regarding this aspect, an approach that proves to be particularly useful is as follows. In case of a quench, the main concern is the temperature the magnet can reach. The maximum temperature is inevitably at the location where the quench started (since, there, the Joule heating acted for the longest time). A conservative estimate of the maximum temperature reached in the so-called hot-spot can be obtained starting from Eq (5.5) and by assuming adiabatic conditions [10]

$$\bar{C}\frac{\mathrm{d}T}{\mathrm{d}t} = \bar{\rho}J^2, \tag{5.6}$$

which, after a simple manipulation yields

$$\int_{T_{op}}^{T_{max}} \frac{\bar{C}(T)}{\bar{\rho}(T)}\, dT = \int_0^{\infty} J_{op}^2\, dt. \tag{5.7}$$

This approach bears similarities to the conductivity integral method employed to assess the maximum temperature within nuclear fuel pellets, where obtaining a reliable analytical function for thermal conductivity is notably challenging. The lhs is an integral function of just material properties while the rhs depends only on the circuit response. Once the profiles of specific heat and electrical conductivity are available, obtaining the left-hand side of the equation simply involves performing an integration leaving the upper boundary of the integral as a free parameter. Instead, the left-hand side is the time integral of the current density (squared). In the case of a circuit in which the magnet dissipates its inductive energy on an external dumping resistor, the time shape of the current is simply

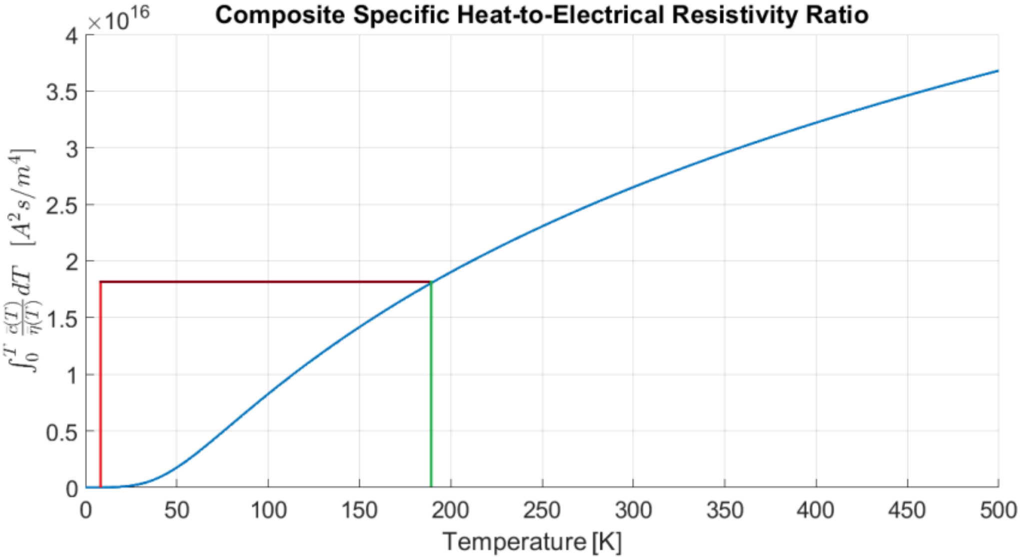

Figure 5.3: Integral function of Eq (5.7) obtained in Matlab and the process to evaluate the maximum temperature (highlighted by red, brown and green boundaries).

a decreasing exponential. Considering also a certain delay due to the time response of the switches and a validation period (the time needed to declare the effective presence of a quench), the function is of the kind

$$J(t) = \begin{cases} J_{op} & \text{if } t < \tau_{delay} \\ J_{op} e^{-\frac{t-\tau_{delay}}{\tau_{circuit}}} & \text{if } t > \tau_{delay.} \end{cases} \tag{5.8}$$

In this expression, τ_{delay} is the sum of the response and validation times while $\tau_{circuit} = L/(R_{magnet+quench} + R_{dump})$ is the time constant of the electrical circuit. Fig 5.3 visually shows the process to get the maximum value of the temperature. One should start from the operating temperature and the corresponding value of the integral function. Then, it has to sum to this value the result of the time integration of the rhs (red line). The brown line brings to the new value of the integral function while the green one shows the corresponding temperature, which now finally coincides with the maximum temperature of the hot-spot. This approach has clearly some limitations. As it is sometimes the case in physical simplifications, the computational effort required remains the same, it just stealthily shifts from one parameter to the other. In the present case the dynamics of the quench is encapsulated in the response time τ_{delay}. Indeed, when considering the same magnet and detection system, the time period during which copper is subjected to the maximum current, resulting in the highest contribution to Joule heating (the flat part of Eq (5.8)), depends on the specific evolution of the quench event. If the quench event evolves in a manner that generates a rapidly increasing voltage profile, ensuring that the quench detection parameters are satisfied beforehand, then the value of τ_{delay} will be smaller, subsequently leading to a lower maximum temperature. An accurate estimation of τ_{delay} would require the knowledge of the voltage profile, but this is not the scope of the hot-spot approximated approach. Nonetheless, other valuable information can be derived from Equation (5.7). If it is further manipulated choosing a fitting approximation for the integral function and the circuit time constant in Eq (5.8) is expressed in terms of the stored magnetic energy and the maximum voltage allowed across the dump resistor, one could obtain the following functional dependencies

$$T_{max} \sim \frac{J_{op}^4}{f_{Cu}^2} \left(\tau_{delay} + \frac{E_m}{V_{max} I_{op}} \right)^2 . \tag{5.9}$$

This relation shows that the hot-spot temperature can be reduced by using a large stabilizer (copper) fraction, reducing as much as possible the detection time of the quench and discharging under the largest possible voltage across the dump resistor. As a general rule, it is always important to try to reduce the inductance of the magnet. By keeping the geometrical configuration of the coil constant, it is possible to achieve this by merging together multiple tapes to form a larger cable (reducing the number of necessary cables and increasing the operating current flowing through each cable). Using the simulation tool described in Section 5.2, the hot-spot approach has been found to give a correct first-order evaluation of the maximum temperature that it is reached inside a magnet because of a quench event.

Another important and useful design parameter is that of stability or energy margin. It is defined as the maximum energy density Δe_h that a superconductor carrying an operating current J_{op} can locally absorb while still remaining fully superconductor [22]. Once again, this approach is considered to be quite conservative because it does not take into account any cooling mechanisms, whether internal, such as conduction, or external, such as a helium cooling system.

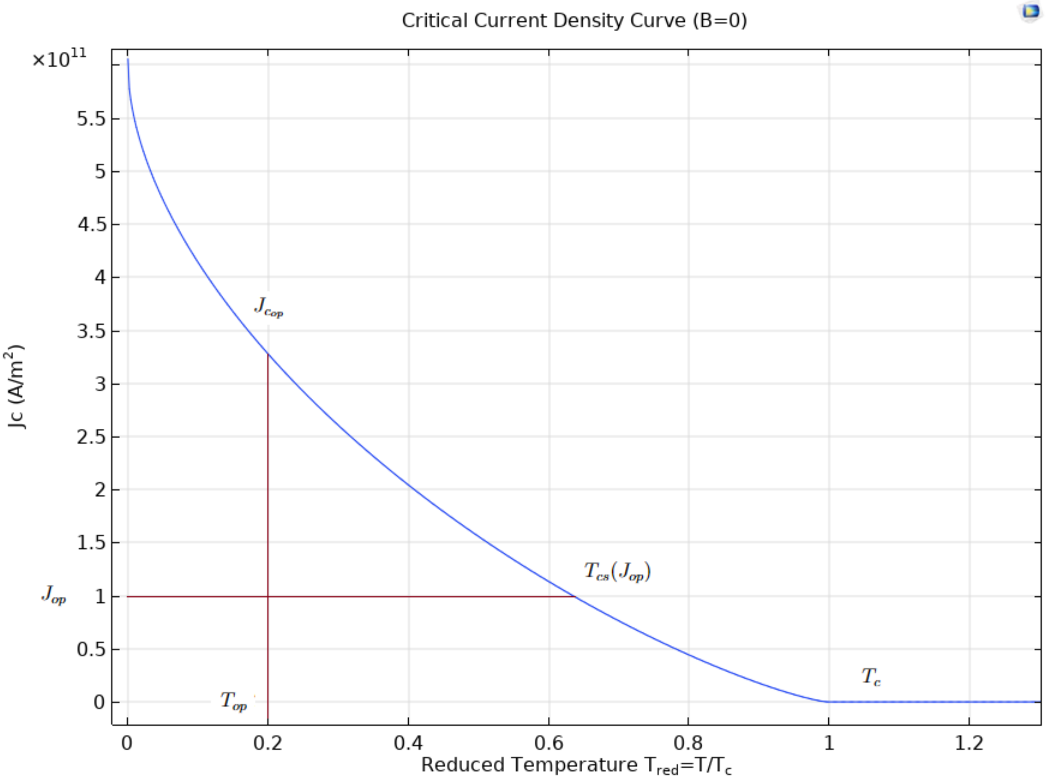

Figure 5.4: Critical current density curve at $B = 0$ of YBCO with respect to the reduced temperature, T/T_c ($T_c^{YBCO} = 91$ K).

As it can be seen in Fig 5.4, the superconductor is working at the operational current density J_{op} and at the operational temperature T_{op} (in the intersection point of the two brown lines). Unless a cooling mechanism balances the Δe_h, the superconductor is heated and its working point moves horizontally on the right. It is able to remain completely superconducting up to the point at which the critical current density at the reached temperature is equal to the operating current density, namely $J_{op} = J_c(T_{cs})$. The temperature when this occurs is called the current-sharing temperature. From this time on, the superconductor is not able to carry the full J_{op}. The current is consequently shared with copper, which now generates Joule heating. At the critical temperature T_c, $J_c(T_c) = 0$ and all the current flows inside copper. Under adiabatic conditions, the safety margin is given by

$$\Delta e_h = \int_{T_{op}}^{T_{cs}(J_{op})} \bar{C}(T)\, dT. \tag{5.10}$$

The safety margin surely depends on the conductor specific heat $\bar{C}(T)$,and the operating and current-sharing temperatures, but also on the ratio between the operating current density and the critical current at T_{op}, $j_{op} = J_{op}/J_{c_{op}}$.

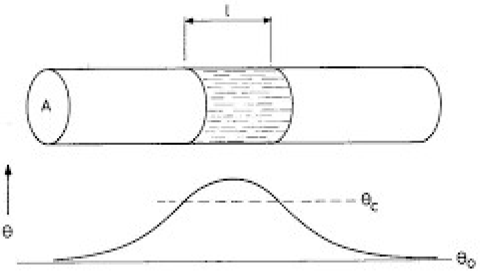

Figure 5.5: 1D normal-conducting zone representation. Image from [51].

The next two concepts are intimately related and were extremely important in the understanding of the disturbances that can occur within a superconducting magnet. To understand the first of the two, the *minimum propagating zone* (MPZ), we need to start from a 1D homogenized superconducting cable. As shown in Fig 5.5, a transient point disturbance produces a local hot-spot in a cable which is carrying its critical current density J_c. We assume, for simplicity, that the temperature of the normal-conducting zone is homogeneous across the cross sectional area A and its value is T_c or even higher, so that the hot-spot generates Joule heating at the maximum rate

$$Q_{Jh} = \bar{\rho} J_c^2 A l, \tag{5.11}$$

with l being the length of the normal area. If the rest of the conductor is at the operating temperature T_{op}, the heat dissipated out of the normal zone is

$$Q_c = 2\bar{k}A\frac{dT}{dx} \simeq 2\bar{k}A\frac{T_c - T_{op}}{l}, \tag{5.12}$$

where the factor 2 accounts for the heat flow out of both sides of the normal zone. The last part of Eq (5.12) is the way in which the temperature gradient can be approximated. Under balance conditions, the heat loss by conduction is equated by the Joule heating. Putting together the two expressions and solving for l, one can obtain

$$l_{MPZ} = \sqrt{\frac{2\bar{k}(T_c - T_{op})}{J_c^2 \rho}}, \tag{5.13}$$

the minimum propagating zone, MPZ. A normal zone that is smaller than the MPZ will

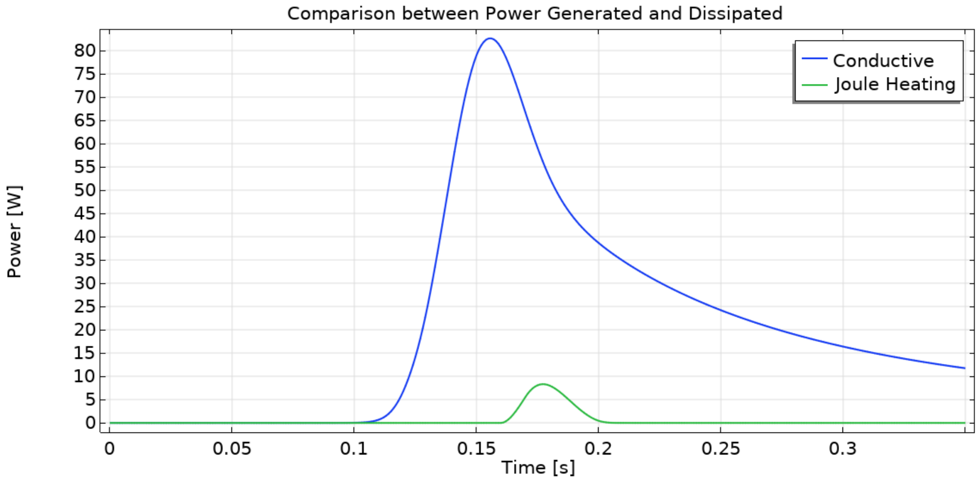

(a) Conditions which did not lead to a quench

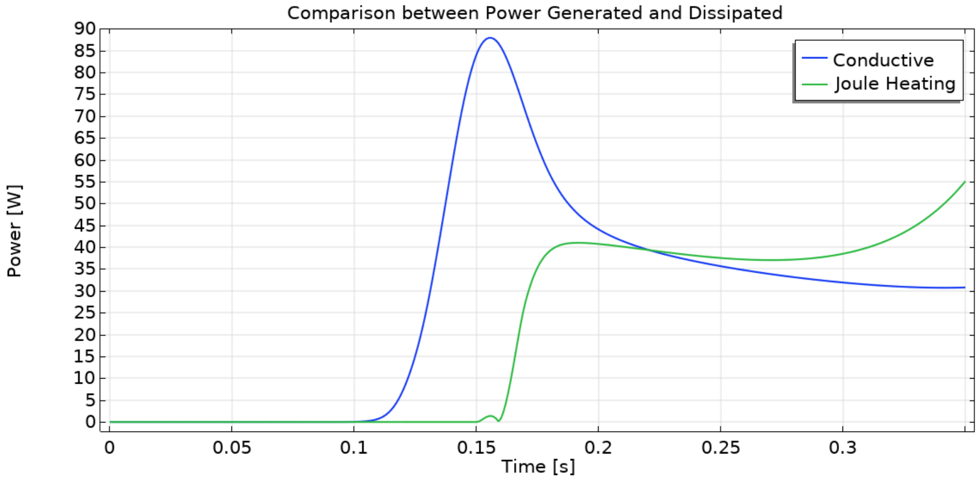

(b) Conditions which did lead to a quench

Figure 5.6: Comparison between the cooling and heating powers in a small heated region.

collapse due to the predominance of conduction over heating. Conversely, a longer zone will expand as heat generation exceeds cooling [51]. This is evident in Figures 5.6, which have been obtained using the simulation of Section 5.2. The first panel shows that the power dissipated because of conduction (blue line) is always greater than the one produced by the Joule heating and indeed the superconductor did not quench. In contrast, the lower panel illustrates that there is a specific moment in time when heating surpasses conduction. This critical point marks the initiation of the temperature runaway, ultimately resulting in the quenching of the entire magnet. The minimum propagating zone concept proves to be particularly useful in classifying the spatial size of disturbances. If the disturbance is much larger than l_{MPZ}, the heat dissipation due to conduction is negligible and the only important parameter in the quench initiation process will be the deposited energy (or power) per unit volume. The disturbance is distributed. Vice-versa, if the disturbance is much shorter, heat dissipation will dominate and the absolute energy needed to establish the MPZ will determine quench initiation. In this regime, the size of the disturbance is no more important and it could be regarded as a point. It is important not to be mislead by this concept: the MPZ is not a *conditio sine qua non* for the quench initiation. In fact, a disturbance leading to quench could be smaller than the minimum zone, as exemplified by the concept of a point disturbance. The definition just states that an already established normal zone, regardless of how it was generated, can only expand if its size exceeds that of the MPZ. Indeed, a point disturbance that heats up a very small region has the potential to trigger a quench, given that the temperature reached is high enough for conduction alone to rapidly generate a sufficiently large normal zone (equal to the MPZ) within a limited time-frame. Results in Fig 5.7 support this view. A point represents the minimum power, given the length of the heated zone, which is necessary

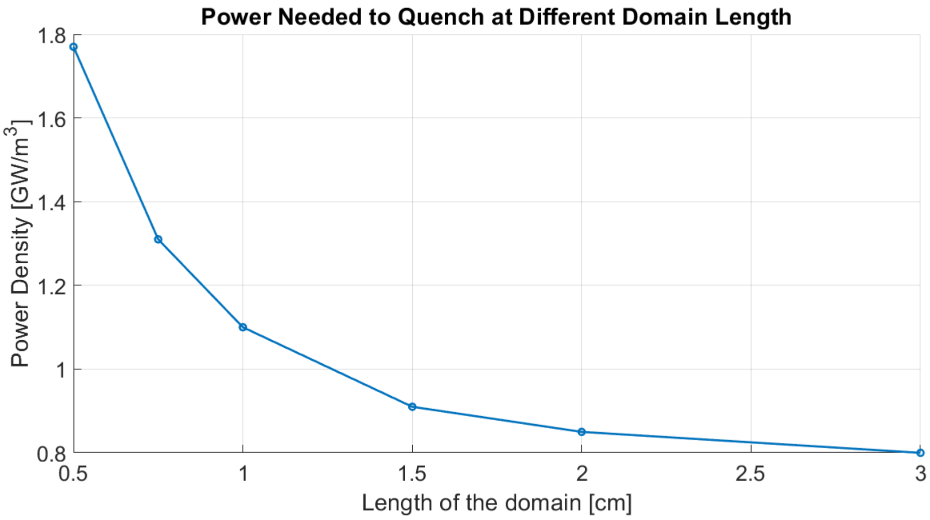

Figure 5.7: Power density needed to initiate a quench for different disturbance dimensions.

to initiate a quench. The profile shows that the smaller is the size of the disturbance, the higher should be its deposited power. To give an order of magnitude of l_{MPZ} for a composite HTS one could safely replace $\bar{\rho}$ and $\bar{k}$ with just those of copper (evaluated as average values between the operating temperature and the critical temperature, $\rho_{Cu} \simeq 3 \times 10^{-9}\ \Omega$ m and $k_{Cu} \simeq 330$ W/(m K)), obtaining $l_{MPZ} \simeq 2$ cm for $RRR = 10$, $T_{op} = 4.2$ K and $B = 6$ T.

An aspect related to the minimum propagating zone is the *minimum quench energy*, MQE. For a 1D homogenized superconductor and in an approximated view, it can be stated that the MQE is the amount of energy which is required to produce the MPZ

$$MQE = V_{MPZ} \int_{T_{op}}^{T_{cs}} \bar{C}(T)\, dT, \tag{5.14}$$

where $V_{MPZ} = l_{MPZ} \cdot A$ is the volume of the minimum propagating zone. Using the value of the l_{MPZ} found before, the MQE can be estimated to be $\simeq 1$ J.

The last concept which is worth discussing here is the quench *propagation velocity.* Once a normal zone has developed, it will continue to expand under the combined action of conduction and Joule heating [51]. The effect is that of a normal state wavefront travelling through the superconducting regions. The quench propagation velocity is particularly useful in evaluating the voltage profile, which is driven by the increase in resistance as the quench expands. The velocity depends on the conductor properties, geometry and the cooling conditions. Since the simulation is adiabatic, the derivation of the quench velocity will also be adiabatic. The first step is to start with Eq (5.5), the 1D temperature diffusion equation. The Joule heating term is approximated by the following temperature profile

$$G(T) = \begin{cases} 0 & \text{if } T < T_s \\ G_c & \text{if } T > T_s, \end{cases} \tag{5.15}$$

where $T_s = (T_{cs} + T_c)/2$, an average temperature between the current-sharing and the critical temperatures. Assuming that the point x_s, the one where $T = T_s$, moves at a constant velocity, it is possible to define a moving reference frame $\varepsilon = x - x_s = x - vt$. With the new coordinate ε, one can express both the time and space partial derivatives under the same total derivative, obtaining

$$\frac{d^2T}{d\varepsilon^2} + \frac{v\gamma C}{k}\frac{dT}{d\varepsilon} + \frac{G(T)}{k} = 0. \tag{5.16}$$

Eq (5.16) is a second order differential equation which has two distinct solutions due to the structure of (5.15). A solution corresponds to the normal region where $G = G_c$ while the second one to the outer superconducting region ($G = 0$). At the interface ($\varepsilon = 0$) it holds that $T = T_s$. The boundary conditions are

$$\varepsilon \to -\infty, \qquad T \to T_{eq}, \tag{5.17a}$$

$$\varepsilon \to +\infty, \qquad T \to T_{op}, \tag{5.17b}$$

where T_{eq} is an equilibrium temperature inside the normal zone. Imposing also the continuity of the heat flux across the interface, the solution reads

$$v_{ad} = \frac{J_{op}}{\gamma C}\sqrt{\frac{\rho k}{T_s - T_{op}}}. \tag{5.18}$$

The accuracy of this formula can be enhanced if the material properties are substituted with the average values over the temperature range of the transition.

5.2. A 1D FE Analysis of a Quench

The introduction of this chapter made it evident that studying a quench is a highly challenging task. Therefore, in obtaining a comprehensive and reliable understanding of its dynamics, as well as the behavior of a quenched magnet, numerical simulations become the primary tools. Considering the intrinsic multiphysics nature of this phenomenon, opting for the already mentioned Comsol Multiphysics © was the appropriate decision. Undoubtedly, capturing all the aspects involved in a magnet quench would necessitate a comprehensive 3D simulation. Nevertheless, it is also true that developing such a model would demand years of experience and several months of dedicated work for its implementation. Due to this reason, within the framework of this thesis work, a more simplified approach was envisaged. The simulation had two main goals. The first, and perhaps the most significant, was to have a reliable and efficient tool for studying the quench phenomenon. Indeed, complementing a theoretical study with practical experience, even if solely numerical, is always beneficial. The second goal is associated with the design of the solenoids for the Muon Collider. In fact, the simulation, albeit simplified, provides an initial understanding of the magnet quench protection analysis, which is considered one of the most crucial tasks for a magnet designer, as discussed earlier. The final step involved converting the simulation into an application. The purpose of the application is to provide users who do not have access to a Comsol license with the opportunity to utilize it. Once the application has been developed, it can be made executable or uploaded to a server, eliminating the need for a license. The instructions for utilizing this application can be found in Appendix A.

The simulation is a 1D transient finite element analysis. Every variation is allowed just along one direction. It is fully parametric, allowing for a vast range of configurations to be covered, from those that are typical of the 6D Cooling solenoids, to those required for conducting parametric studies (as described in Section 5.3). The main component of the model is a 20 m long HTS cable that experiences localized and transient heating due to a disturbance. The occurrence of a quench depends on the properties of the disturbance. Insufficient power density deposition will cause the heated zone to return to its initial conditions, while adequate deposition will trigger a quench which will be subsequently studied in some of its aspects (voltage profile, front velocity, maximum temperature reached and so on).

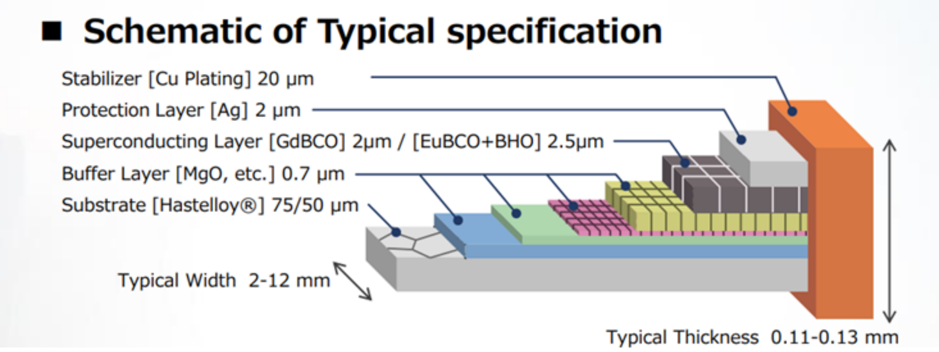

Figure 5.8: Composition of a Fujikura ReBCO tape. From Fujikura website.

The tape used in the simulation is a multi-layer HTS tape that is modeled as a homogenized material. This approach considers the multi-layer structure not by analyzing singularly each layer, but rather defining a fictitious material which is the result of the mixture of their properties. A second generation HTS tape is a very complex component with several layers and materials, as shown in Figure 5.8. Out of all them, the copper stabilizer, the Hastelloy substrate, and the YBCO (Yttrium Barium Copper Oxide) superconductor are the most significant, and they are the ones modeled within the simulation. Each material has its own set of properties and the ones which are useful in the analysis of a quench event are the thermal conductivity, the heat capacity and the electrical resistivity. Depending on the type of material, each of those functions can depend on temperature alone or on other parameters as well. Some examples are shown in Figures 5.9. Let's examine each of them separately, starting with copper. Copper's specific heat is just a function of temperature while both the electrical resistivity and the thermal conductivity are also dependant on the RRR and the applied magnetic field. As for Hastelloy, its properties can be straightforwardly modeled as functions of temperature

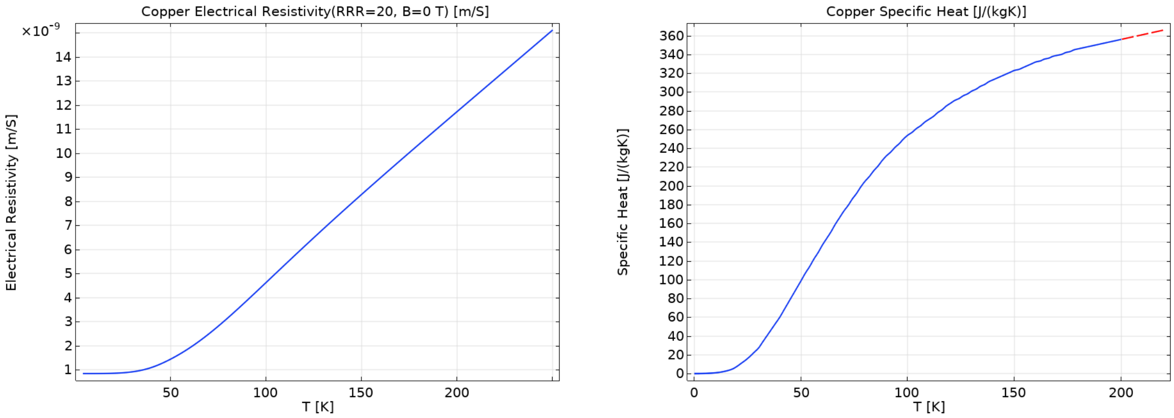

(a) Copper Electrical Resistivity.

(b) Copper Specific Heat.

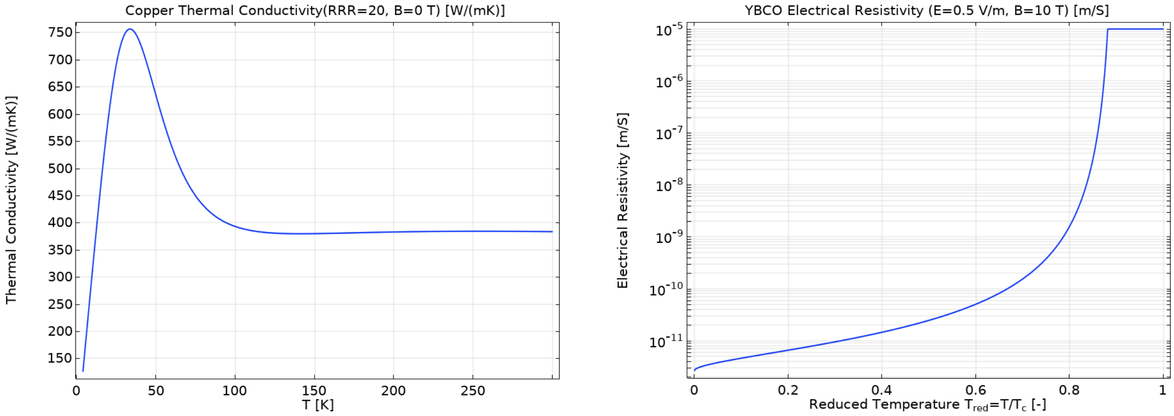

(c) Copper Thermal Conductivity.

(d) YBCO Electrical Resistivity ($B = 10$T).

Figure 5.9: Copper properties and YBCO electrical resistivity used in the simulation.

alone. The same applies for YBCO thermal conductivity and specific heat, while its electrical properties demand more attention. The electrical resistivity of a superconductor, as explained in Chapter 2, can be modeled as a power law, and in particular, in the simulation is expressed as

$$\rho_{\text{YBCO}}\left(T_{red}, E, B\right) = \min\left(\frac{E^{\frac{n-1}{n}} \cdot E_0^{\frac{1}{n}}}{J_c(T_{red}, B)} + \rho_0,\ 10^{-5}\ \Omega\ m\right). \tag{5.19}$$

The minimum function is important because the power law holds when the superconductor is in the superconducting state, but ceases to be valid when it is fully normal. It is clear that the resistivity depends directly on the electric field the conductor is subjected to and on the (reduced) temperature and magnetic field by means of the critical current density. The latter function is the same as the one presented in Section 2.4 (Eq (2.41b)). Regarding, instead, the function in Eq (5.19), $E_0 = 100$ mV/m and $\rho_0 = 10^{-16}\ \Omega$ m. The homogenization of the properties is performed by

$$C_{\text{comp}} = \sum_i f_i \gamma_i c_i, \tag{5.20a}$$

$$k_{\text{comp}} = \sum_i f_i k_i, \tag{5.20b}$$

$$\gamma_{\text{comp}} = \sum_i f_i \gamma_i, \tag{5.20c}$$

$$\rho_{\text{comp}} = \sum_i \frac{f_i}{\rho_i}, \tag{5.20d}$$

with $i = \{\text{Copper, Hastelloy, YBCO}\}$ and γ the density. The composition of the tape can be tuned by the user changing the volume fractions, keeping in mind that $\sum_i f_i = 1$ must hold.

Similar to the solenoids simulation in Chapter 4, in this case as well, the different "physics" are assigned to separate modules. The first among them is the *Electric Current* module. In this module, a current density can be applied to one of the two ends, effectively converting the component into an actual cable. No sources or sinks of electric charge are present within the domain, meaning that the electric current entering one end is equal to the current exiting the other end. The two main equations governing this node are

$$\boldsymbol{J} = \underline{\underline{\sigma}}\boldsymbol{E} \rightarrow J_x = \sigma E_x, \tag{5.21a}$$

$$\boldsymbol{E} = -\nabla V \rightarrow E_x = -\frac{dV}{dx}. \tag{5.21b}$$

The first is the constitutive equation which relates the current density and the electric field (it is called the microscopic Ohm's law) while the second is the relationship between the electric field and the voltage. The voltage V plays an important role being the dependent variable of the module.

The second module is the *Heat Transfer in Solid.* It allows to simulate the temperature evolution inside the domain. It relies on the thermal equilibrium equation (like Eq (5.1)) and its dependent variable is of course the temperature T. The initial condition is set as the operating temperature, while the boundary conditions involve maintaining the two ends of the domain fixed again at the operating temperature. Keeping the two extreme points fixed at the initial temperature is a form of cooling. However, since the goal of the model is to simulate an adiabatic quench, a solution is to make the cable extremely long, making sure that the heat flow in those locations is negligible. With a 20 m long cable, the heat flow escaping the domain is evaluated to be at least 5 to 6 orders of magnitude less than that in the central part. No heat flow is allowed across the transverse directions with respect to the cable axis. The transient disturbance is simulated by a Gaussian impulse of power density while the Joule heating is added as a power source $E_x \cdot J_x$ distributed throughout the domain.

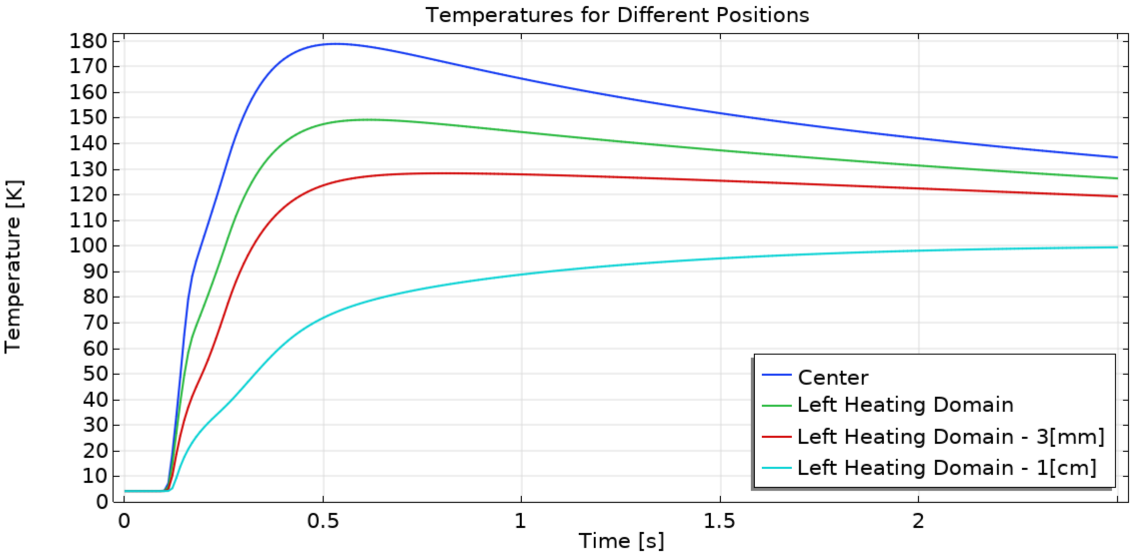

(a) Temperature time profile in different points of the domain.

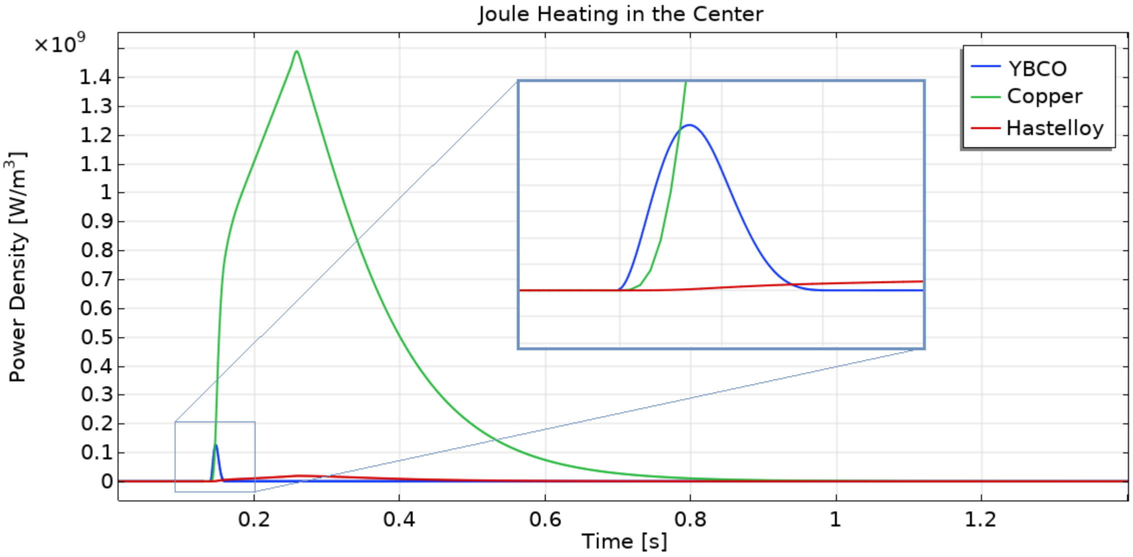

(b) Joule heating time profile in the central point.

Figure 5.10: Examples of temperature (a) and Joule heating (b) profiles.

The first plot of Fig 5.10 shows the temperature profiles of four different points within the domain ("Center": central point; "Left Heating Domain": left interface between the small central domain where the Gaussian heating operates and the remaining part of the cable;

"Left Heating Domain -3[mm]": 3 mm to the left from "Left Heating Domain"; "Left Heating Domain -1[cm]": 1 cm to the left from "Left Heating Domain") . For simplicity, focusing solely on the central point (blue line), the simulation clearly illustrates an initial runaway. The temperature experiences a rapid increase due to the combined effects of the heat disturbance and Joule heating, reaching a maximum value before subsequently decreasing. Without any protection circuit in place, the temperature would continue to rise without bound, leading to the complete failure of the system. In Figure 5.10b, the plot depicts the Joule heating contributions in the central point. In the zoomed region, a small initial contribution from the superconductor during the current-sharing regime can be observed. However, when considering the overall plot, the substantial contribution from copper becomes apparent, reaching magnitudes on the order of some GW/m^3. In this plot, the effect of the exponentially decreasing current, caused by the protection system, can be observed in the decreasing power generation. As the current diminishes, the power generated also decreases accordingly.

The final module, the *Electrical Circuit*, plays a crucial role in the simulation as it enables the incorporation of any desired electrical circuit, including the safety system. The software translates the topology of the input circuit into a system of coupled differential equations and then uses the solution inside the simulation itself. For example, the cable appears in the circuit as a time dependant resistor whose properties change step by step due to the evolution of the quench. This module and the rest of the simulation are strictly

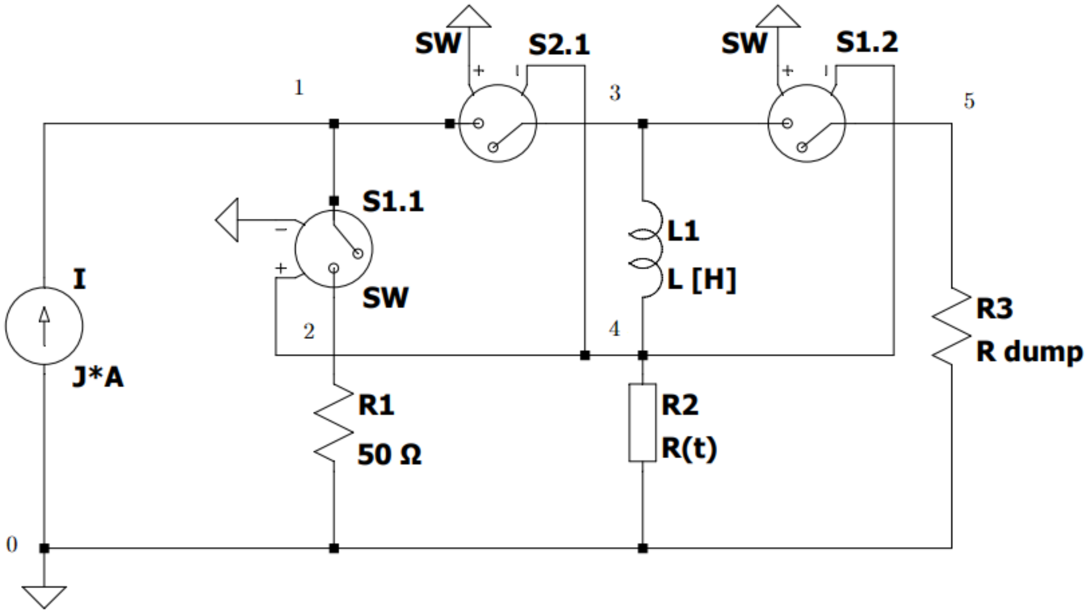

Figure 5.11: Overall electrical circuit of the simulation.

coupled: the evolution of the current inside the circuit influences the thermal response which in turn influences back the circuit. Figure 5.11 shows the topology of the circuit that was implemented. From node 0 (ground) to node 1, an ideal current generator provides a constant $J_{op}A$ current. Branch 32 simulates the solenoids by means of an inductance in series with a resistor. There are two kind of switches but they are triggered by the same event: the voltage across the magnet has to overtake a threshold value of 100 mV for a validation time of 10 ms. Switches S1 are initially opened, while switch S2 is initially closed. In the initial configuration, branch 32 is the only active part of the system and it is energized by the ideal generator, but when the trigger event closes the S1 switches and opens S2, the topology of the circuit changes. The opening of S2.1 decouples the circuit into two subcircuits. The left circuit is purely a requirement of the software and does not have any practical significance (the ideal generator has to dissipate its energy through a resistor R1). On the other hand, the right circuit can be considered as the safety circuit. In this configuration, the solenoid dissipates its stored magnetic energy through a dump resistor, resulting in an exponential decrease of the current. The triggering condition of the switches can be deactivated by the user. In fact, if the activation of the safety circuit is essential for the magnet protection analysis, from the other side it does not allow to collect useful data on the quench propagation velocity. It turns out that it is strongly influenced by changes in the circuit topology and can be accurately evaluated only when the current through the cable is maintained at its operating value.

5.3. Results

In this section, I will present the results obtained using the simulation. Unlike the previous section (Section 5.2), where the plots and results were referred to a single configuration at a time, here I aim to provide more general results by comparing different configurations. This approach is beneficial for understanding the quench phenomenon as a whole and identifying the parameters on which it depends.

5.3.1. Maximum Temperature

In this paragraph, the results related to the protection side will be presented. A quench is initiated using the same magnet configuration, except for the change of a single parameter, and the results are compared. Here, the main focus is on the maximum temperature reached inside the cable, as it is one of the main concerns during the quench of a magnet. The first aspect I focused on is the number of tapes required to compose a cable for proper magnet protection. The magnet used as a case study was the solenoid in cell A1.

Its geometry was previously presented in Chapter 4. Here, it is important to state its magnetic characteristics: with a winding of isolated 12 mm x 0.11 mm tape, its inductance is 17.6 H, and it is subjected to a maximum magnetic field of 4.1 T at the inner radius. As evident from Eq (5.9), the maximum temperature reached as a result of a quench event also depends on the current flowing inside each cable. Increasing the number of electrically isolated tapes that composed a single cable does not have any effect on the stored magnetic energy, but definitely reduces the inductance of the magnet (the inductance scales as $\sim N^2$, see Eq (4.9)). The reduction of the inductance is of capital importance if one considers the characteristic time constant of the RL protection circuit ($\tau = L/R$). A shorter time constant means a faster dumping of the current which flows through the solenoid and hence a smaller integral contribution of the Joule heating. Fig 5.12 shows the evolution of the maximum temperature, at different applied magnetic field, as the number of tapes per each cable increases.

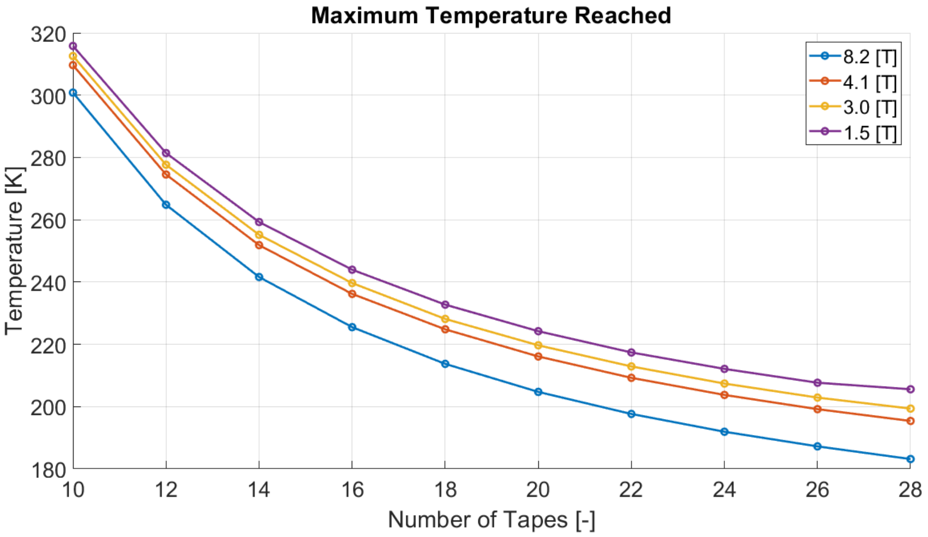

Figure 5.12: Maximum temperature evolution with respect to the number of tapes, at different magnetic fields.

As expected, increasing the number of tapes and, consequently, decreasing the magnet's inductance leads to a decrease in the maximum temperature reached. Taking into consideration the approximate result that such a simulation can provide, it can be inferred from the plot that at least approximately 30 tapes per cable are required to sufficiently reduce the inductance, ensuring that the maximum temperature does not exceed the safety threshold of 200 K. A second important result that can be inferred from this plot is that, from the perspective of maximum temperature, it is more challenging to protect the magnet when the quench starts in a low magnetic field region compared to a high

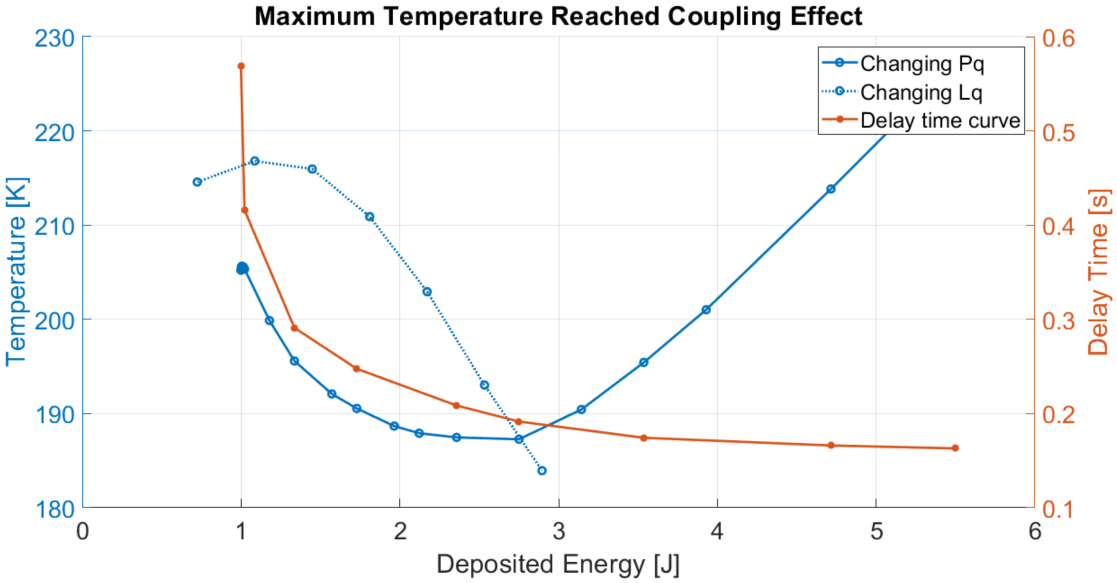

(a) Variation of maximum temperature with deposited energy and corresponding delay time. The Deposited Energy is changed by either changing the peak value of the gaussian power density impulse (solid curve, denoted as 'changing P_q') and keeping the disturbance length constant ($L_q = 1.9$ cm), or by keeping P_q constant ($P_q = 3.5$ GW/m^3) and varying the disturbance length (dashed curved, denoted as 'changing L_q'). The Delay time (solid red curve) is the time at which the switch activates based on the circuit shown in Fig 5.11.

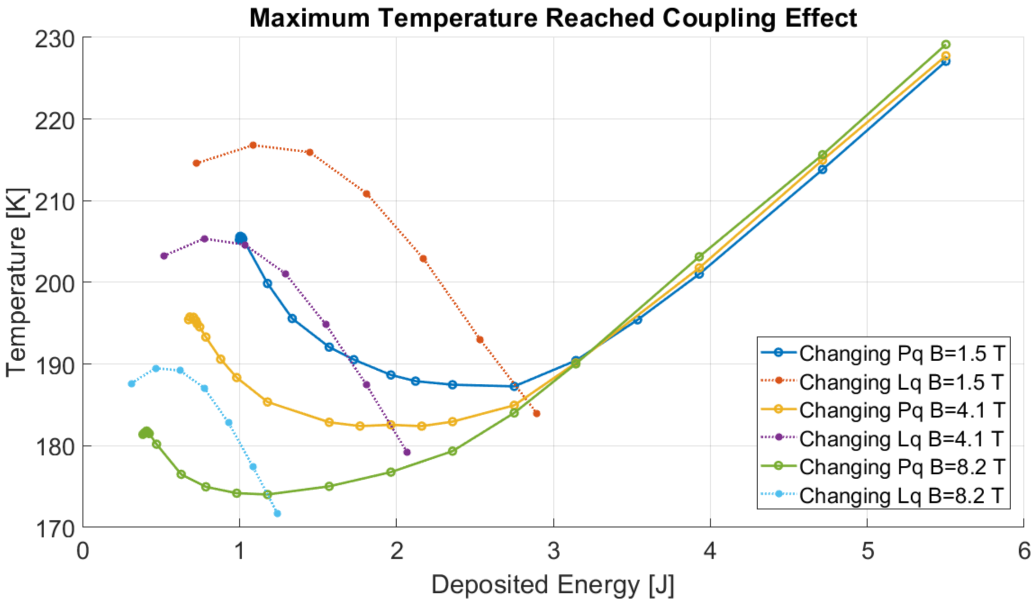

(b) Same curves but at different magnetic fields.

Figure 5.13: First panel: definition of the curves used as probes. Second panel: comparison changing the applied magnetic field.

field region. This finding may seem counterintuitive. Indeed, the thermal and electrical properties of the homogenized tape worsen as the applied magnetic field increases. However, as shown in the next paragraph, the normal zone expands at a higher velocity, leading to a faster increase in voltage. Consequently, the voltage threshold value is reached sooner, enabling the protection system to act sooner as well.

The conclusions drawn so far are all correct, but it turned out that they did not include the effect of a very important parameter. The profiles in Fig 5.12 are generated keeping constant all the parameters (operating temperature, operating current density, copper RRR, length of the heated region etc) excepts, of course, those under examination (magnetic field and number of tapes) and the power density deposited in the disturbance region. In fact, the power needed to initiate the quench is different for different values of applied magnetic field and hence it has to be changed. The problem is that the final maximum temperature turned out to depend also on the applied energy density. This is clear in Fig 5.13a. The solid blue line represents the maximum temperature reached, at constant disturbance length (in this case 1.9 cm), while changing the peak value of the gaussian power density impulse. The plot is expressed in terms of the absolute deposited energy

$$DE = L_{\text{disturbance}}\, A \int_0^\infty P_{\text{q}} e^{-\frac{(t-t_0)^2}{2\Delta t^2}}\, dt, \tag{5.22}$$

where P_{q} is the peak value of the impulse and Δt its standard deviation. Looking at Eq (5.22), it is evident that the deposited energy can be changed varying several different parameters (here the effect of P_q and $L_q \equiv L_{\text{disturbance}}$ The first point corresponds to $P_{\text{q}} = 1.27$ GW/m^3 ($\simeq$ 1J), which is the minimum power needed to initiate a quench, while the last one to 7 GW/m^3 ($\simeq$ 5.5J). Interestingly, there is an initial regime (from 1 J to approximately 2.5 J) where an increase in the deposited power results in a decrease in T_{max}. Looking at the solid orange line, the reason behind this phenomenon becomes clear. The line represents the time when the switches activate, indicating when the protection system comes into play. In this case, the delay time decreases rapidly and then reaches saturation after $\sim$ 3 J. This suggests that in this regime, the switching time no longer plays a significant role in determining the maximum temperature reached by the system. Actually, it appears that there is a linear correlation between the temperature and the power density impulse. This correlation may be attributed to the dominance of the Gaussian power impulse in overall power density generation with respect to the Joule heating caused by the quench event itself (see Figures 5.14). There will be another evidence of this and the end of the paragraph. In fact, the thermal balance equation in the case in which the Gaussian term overweights the Joule heating reads

$$C(T)\frac{\partial T}{\partial t} = P_q e^{-\frac{(t-t_0)^2}{2\Delta t^2}} \tag{5.23a}$$

$$\int_{T_0}^{T_{max}} C(T)\, dT = P_q \int_0^{\infty} e^{-\frac{(t-t_0)^2}{2\Delta t^2}}\, dt. \tag{5.23b}$$

It is evident from Eq (5.23b) how there is a linear relationship between the maximum temperature reached and the peak power density P_q.
The dashed blue line, instead, is constructed by fixing P_q to 3.5 GW/m^3 (the power density corresponding to the minimum of the solid blue line), and by changing the length of the disturbance (L_q). Also here we can observe a pattern. There are two regimes: in the first, the temperature increases increasing the length, while in the second it decreases. The decreasing pattern can be explained by the same voltage argument as before: the bigger is the normal zone, the sooner the voltage will reach the threshold value. Conversely, the increasing branch could be explained by a bigger contribution of the cooling due to conduction. There is one last interesting consideration that can be made using Fig 5.13a. The fact that the dashed blue and solid blue lines do not overlap, even when normalized to the same parameter as the deposited energy, indicates that changing the length of the disturbance or altering its peak power value (while maintaining the same deposited energy) has different consequences on the system.
Now, it should be clearer why Fig 5.12 is not a good representation of the phenomenon it aims to explain. The positioning of a constant magnetic field line above or below another can be a result of the specific values chosen for P_q and $L_{\text{disturbance}}$, rather than having a real physics motivation. With all of this in mind, Fig 5.13b can now be explained

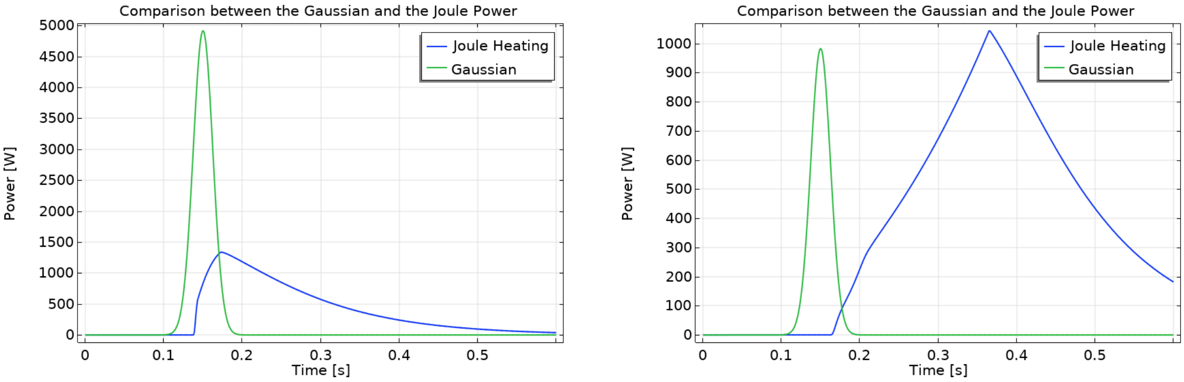

(a) $P_q = 7.0$ GW/m^3.

(b) $P_q = 1.4$ GW/m^3.

Figure 5.14: Comparison between heat contributions at different P_q

simply. In the "parabolic-like" part of the plot where the maximum temperature is directly influenced exclusively by the quench phenomenon, increasing the magnetic field results in an overall decrease of T_{max}. Instead, in the linear part, the degradation of the thermal properties of the material (especially the thermal conductivity of copper) due to a higher magnetic field results in a higher reached temperature. With the same approach other parameters can be studied. Fig 5.15a shows the behaviour of the temperature changing

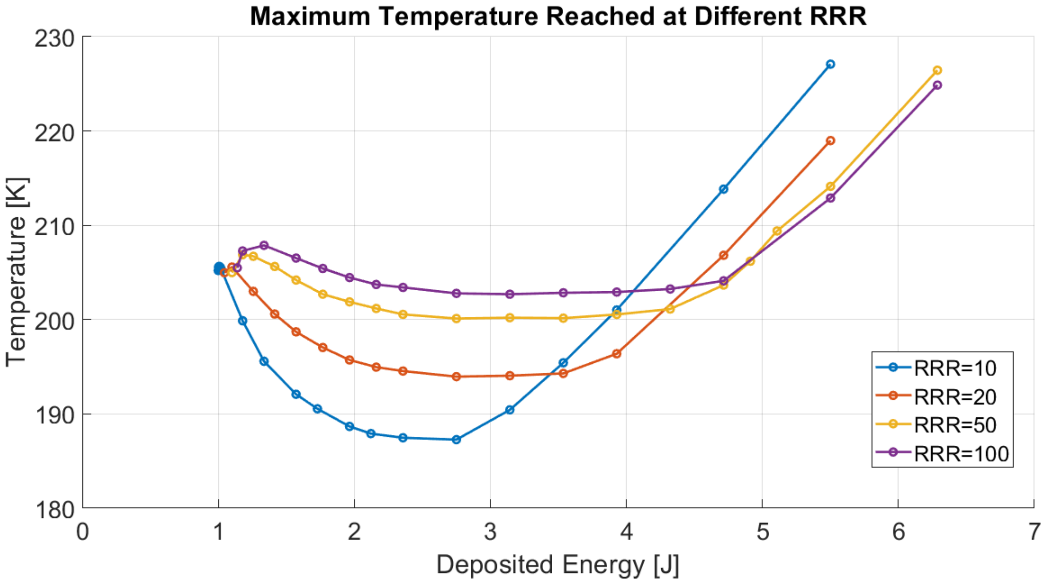

(a) Maximum temperature curves with different RRRs.

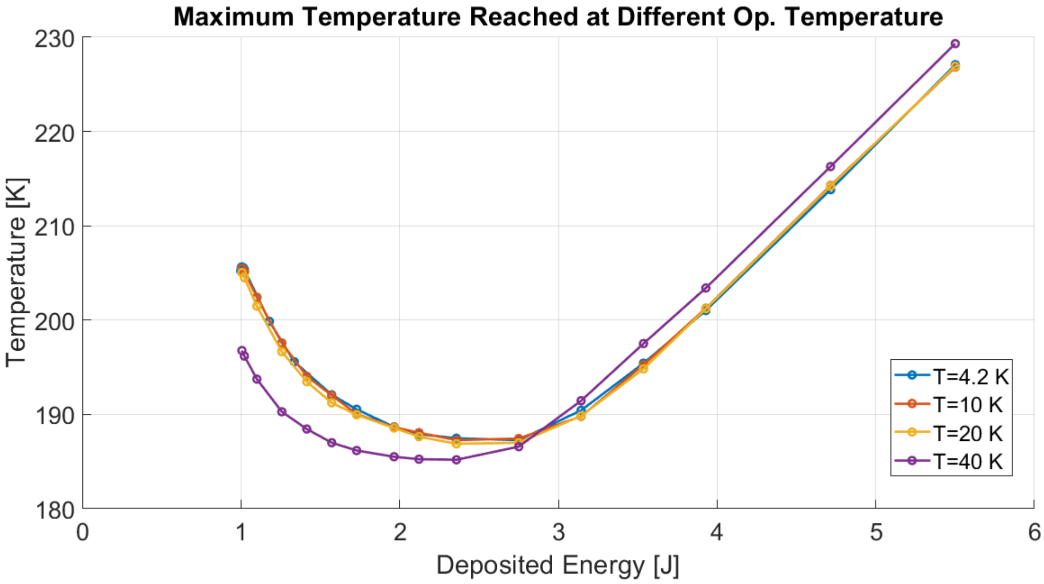

(b) Maximum temperature curves with different operating temperatures.

Figure 5.15: Other two cases: changing copper RRR (first panel) and changing the operating temperature (second panel).

the RRR of the copper. First, it can be noted that increasing the RRR by one order of magnitude (from 10 to 100) results in only a minimal increase in the minimum power needed to initiate the quench. In agreement with the explanation given so far, a smaller RRR (so worse thermal properties of copper) reflects in a lower value of the maximum temperature in the first regime and in a higher in the linear regime.

An interesting case is the change in operating temperature shown in Fig 5.15b. The curves related to $T_{op} = \{4.2,\ 10,\ 20\}$ K can be barely seen because they almost coincide. Conversely, the $T_{op} = 40$ K shows a different behaviour. While it is true that a more comprehensive understanding of the phenomenon would require a greater number of curves to be compared, it can also be equally asserted that the underlying reasons for this peculiar

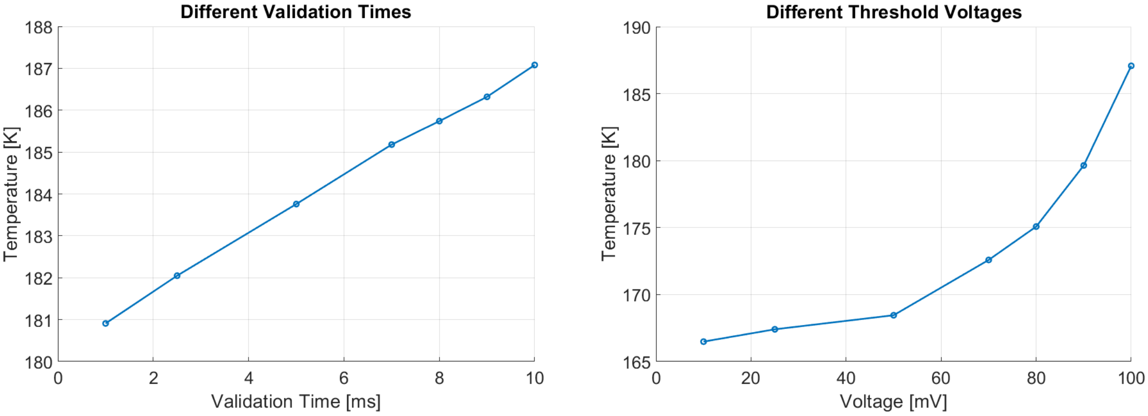

(a) Change of the validation time.

(b) Change of the voltage threshold.

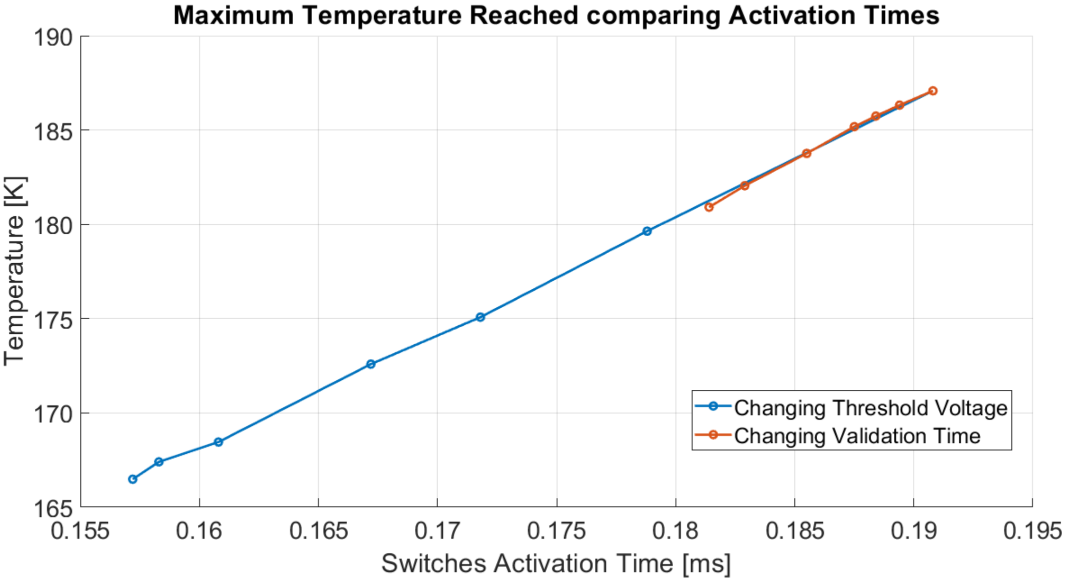

(c) Comparison of the two effects.

Figure 5.16: Study on the reaction (delay) time of the protection system.

behavior can be found in Fig 5.3. The integral of the ratio between the specific heat and the electrical resistivity of the homogenized material remains nearly constant at a low value in the lower temperature range, and then undergoes a sudden increase near approximately 40 K. It is interesting to note that each parameter whose change leads to a decrease in the maximum temperature in the "parabolic" regime, inversely results in an increase in the linear domain. Naively, it seems that having the material in worse thermal conditions is beneficial from just the maximum temperature quench protection perspective, as it ensures a higher voltage build-up and, consequently, a faster response of the protection circuit. Since the response time of the circuit has been shown to play such an an important role, it became evident that a targeted study focused on this aspect was necessary. Besides the maximum voltage allowed across the ends of the dump resistance (which has been fixed to 1 kV to avoid electrical failure of the resistance itself), the other two parameters that can be changed are the validation time and the voltage detection threshold. The validation time refers to the time period during which the system needs to remain above the threshold voltage in order to confirm that the voltage increase is indeed caused by a genuine quench event rather than a spurious occurrence. In all the previous simulations these parameters have been set to the default (and reasonable) values of, respectively, 10 ms and 100 mV. In the study of Fig 5.16a, the validation time has been decreased from its original value down to 1 ms (10 % of the default value). The plot shows a linear decrease of the temperature as the validation time decreases. In the study of Fig 5.16b the validation time has been set back to 10 ms while the voltage threshold has been changed from 100 to 10 mV (again 10 %). This time, the decrease does not appear to be linear, and moreover, compared to the same percentage reduction of the original value as in the previous case, the temperature reduction now is significant. At first glance, given the different profiles and their distinct effects on the final maximum temperature, one might be tempted to conclude that changing the validation time or the voltage threshold are two unrelated actions. However, Fig 5.16c reveals that, *at least* for the range of values that have been tested, they are two sides of the same coin. In fact, if the two previous profiles are plotted not in relation to their original changing parameters (i.e., validation time and threshold voltage), but with respect to their shared aspect (the safety system activation time), the appearance changes. The two curves now overlap, indicating that the crucial factor is not the specific type of change being made, but rather the amount of time in advance the specific change triggers the system. Noting that, it is also true that from a practical point of view, the two actions are not equivalent and a more effective improvement of the protection system lies in the reliable reduction of the threshold voltage rather than reducing the validation time.

5.3.2. Quench Propagation Velocity

The second part of this study focuses on the quench propagation velocity. The analytical approximate formula, which was previously presented in Section 5.1.3, was developed under the assumption of temperature-independent properties of the material. However, it is evident that this assumption is a significant simplification. In an attempt to extend its validity range also to a real case where all the material properties are functions of the temperature, the constant values are replaced by integral averages. Using as extremes of integration T_{op} and $T_s = (T_{cs} + T_c)/2$ leads to unsatisfactory results. So, as a last resort to give Eq (5.18) a final chance, I selected the lower bound in such a way that the two velocities (numerical and analytical) would coincide for the $B = 1$ T case. As it is evident from Table 5.1, also this attempt proved to be unsuccessful. The only viable approach is the use of a numerical method. The simulation that has been presented and developed in the previous sections also happens to be suitable for determining the quench front velocity. However, a couple of changes need to be made. The first change involves deactivating the safety circuit. The dynamics of the external circuit heavily influences the quench propagation, and to accurately evaluate the phenomenon, it is necessary to maintain constant the current conditions. The second consists in the addition of a proper speed detection system. This involves two steps. The first is to define a condition for the passage of the quench front. To avoid the calculation within the software of the magnetic field dependent critical temperature, a more general method has been employed. It turned out that an arbitrarily (but properly) chosen value of the space derivative of the Joule heating ($\partial(E \cdot J)/\partial x = [\partial(E \cdot J)/\partial x]_{threshold}$) is a good

Velocity comparison

Field [T]	Numerical [cm/s]	Analytical [cm/s]
1.0	3.43	3.43
2.5	3.73	3.52
5.0	4.28	3.71
10	5.91	4.34
15	8.91	5.59

Table 5.1: Comparison between the quench velocities using the analytical formula and the Comsol simulation under different magnetic fields.

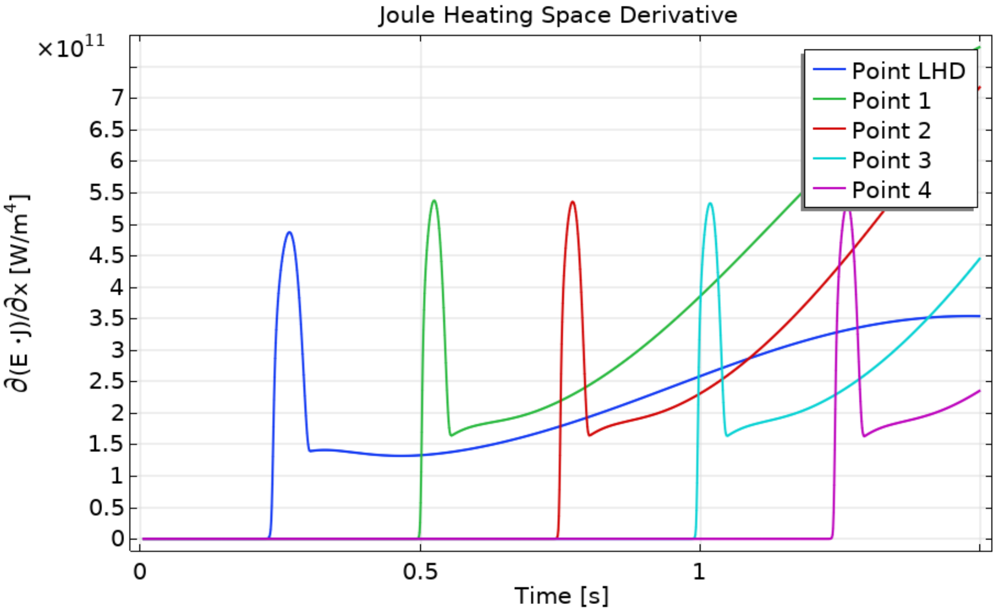

Figure 5.17: Space derivative of the Joule heating. Point LHD ("Left Heating Domain") is the same point as described below Fig 5.10 , and Points 1 to 4 are detection points at incremental increases of 0.5 cm

representation of the quench passage (see Fig 5.17). At the interface between the normal and the superconducting zones the derivative is extremely steep because, from one side (normal) the heat produced by the Joule effect is relevant, while on the other side (superconducting), it is practically zero. The final step involves defining the detection points and implementing timers that will enable the calculation of the average velocity between two consecutive points. The detection points were chosen as follows: the first point corresponds to one side of the heated domain, while the other eight points are spaced 0.5 cm apart from each other. In Comsol, there is no built-in "timer" function, so its ability to solve differential equations was awkwardly exploited by

$$\frac{d\tau_i}{dt} - \mathrm{Rect}(t) = 0, \tag{5.24}$$

where τ_i is the i-th timer and Rect(t) is the rectangular function which becomes 1 when the i-th point hits the quench passage condition and returns to 0 when the condition is hit by the $(i+1)$-th point.

In the same way as it was done in the previous paragraph, several quenches are initiated using the same magnet configuration, except for the change of a single parameter, and the results are compared.

The first study is about the effect of the type of disturbance on the quench propagation.

Figure 5.18 has a twofold goal. First, it will be used to explain the approach that has been used, and then it will serve as a sort of validation test bench for the model. As introduced earlier, the quench velocity is measured on eight different 0.5 cm long intervals. This approach is essential to capture the evolution of the wavefront propagation. It is evident from these plots (and subsequent ones) that the normal-superconducting interface near the disturbance propagates at a different rate compared to the outer regions, where the wave reaches a stationary state. The right plots, on the other hand, do not provide additional information compared to the left ones, but they are useful for quickly understanding the effect of the parameter under test on the propagation. The blue line shows the evolution of the velocity measured at the first data point, while the orange line represents the

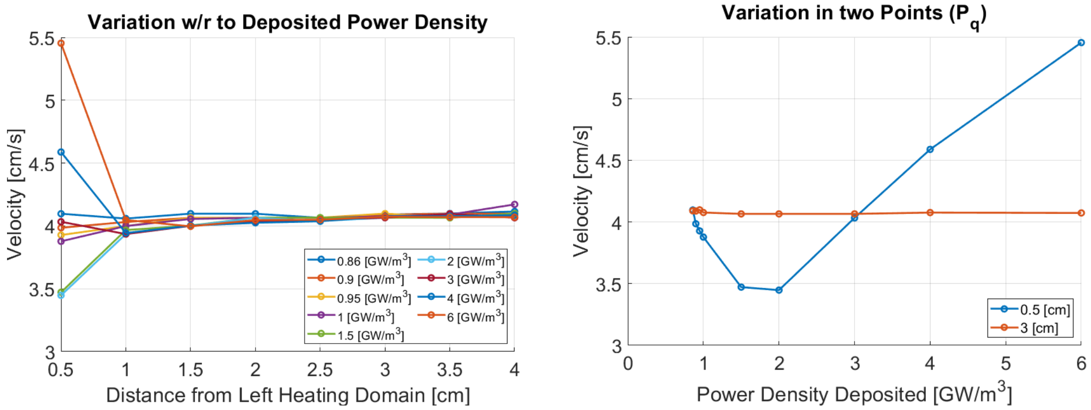

(a) Change of P_q.

(b) Variation in two points.

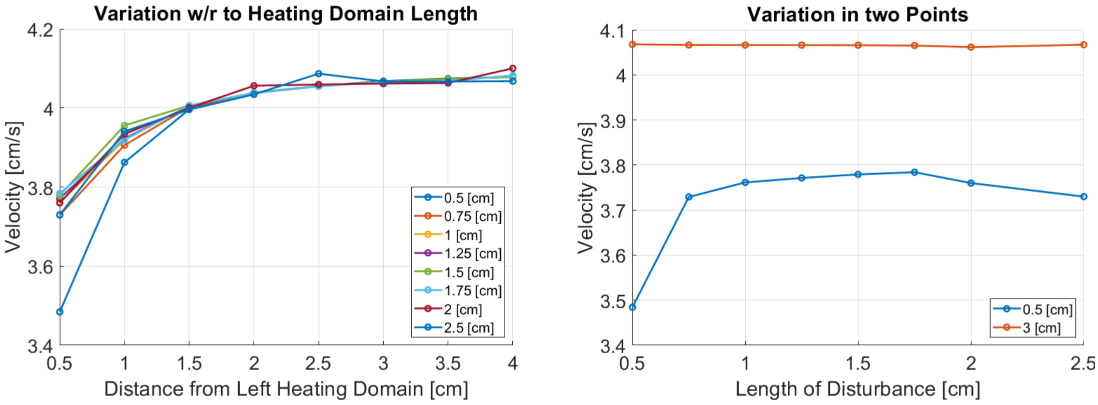

(c) Change of L_q.

(d) Variation in two points.

Figure 5.18: Left panels: evolution of the quench velocity as it moves away from the center. Right panels: Inspection of the velocity at two points (0.5 and 3 cm) as the total energy deposited [J] is changed by varying (b) the peak Gaussian power P_q or (d) the length of the energy deposition L_q.

evolution of the velocity at a point where it should have reached saturation. Figures 5.18a and 5.18b show the effect of the peak value of the power density deposition. The power density varies from 0.86 to 6 GW/m^3. As soon as the quench starts to propagate its velocity depends on the whole set of thermodynamics conditions it is subjected to, in an similar fashion with respect to the explanation given for the maximum temperature trend. However, once it reaches saturation, the velocities become identical, regardless of the input disturbance (as indicated by the flat orange line). This behaviour is what one

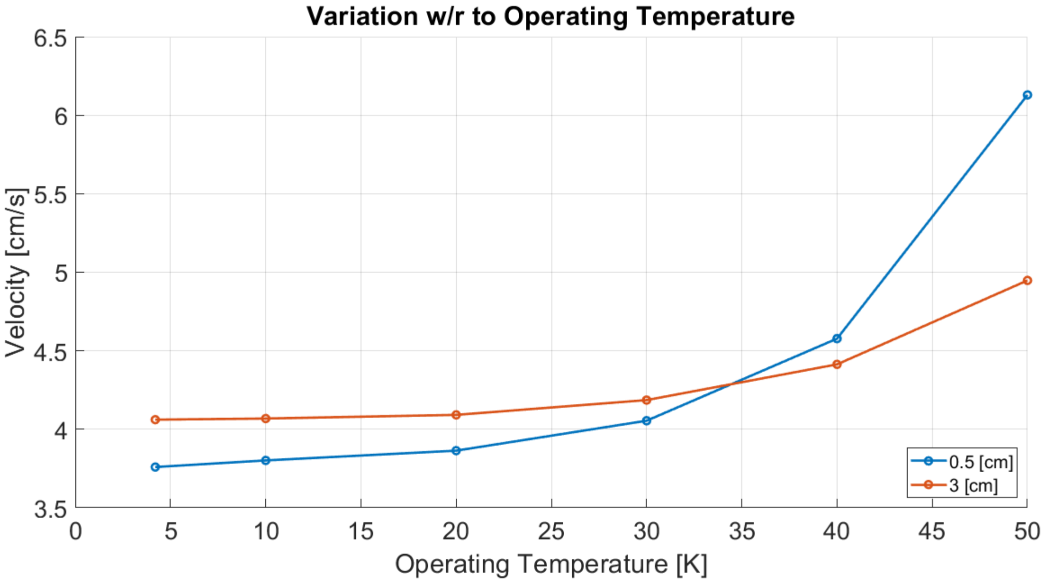

(a) Operating temperature study.

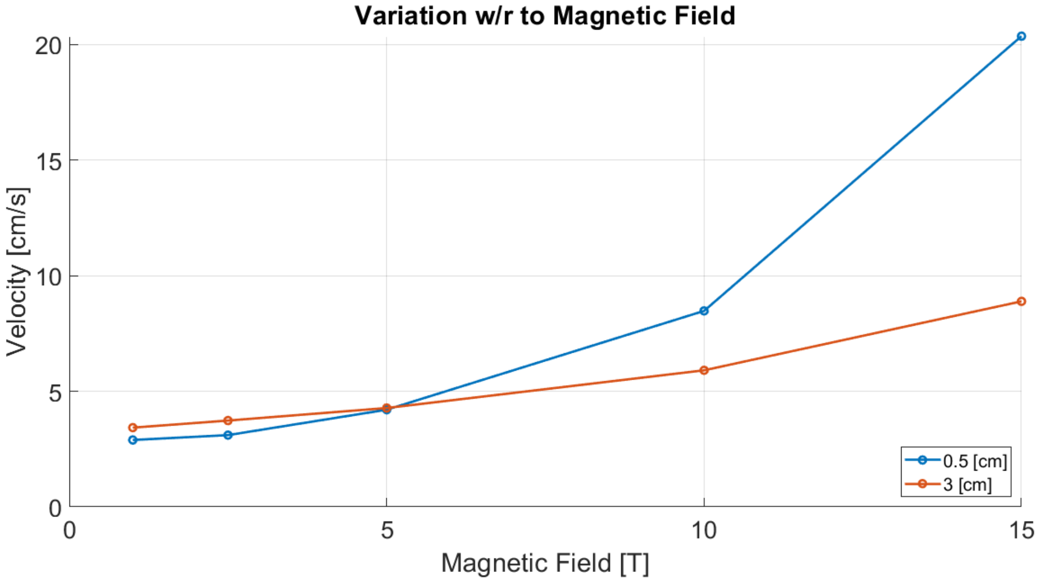

(b) Magnetic field study.

Figure 5.19: Variation with respect to T_{op} (up) and B (down).

expects from the phenomenon dynamics and hence its finding can be seen as a successful validation of the model simulation. The same conclusions can be drawn for the situation depicted in Figures 5.18c and 5.18d. Changing the length of the disturbance does not influence the quench saturation velocity. In summary, the characteristics of the disturbance, such as its magnitude and spatial extent, have the ability to influence the propagation in the initial stage but they seem to become irrelevant for the stationary behavior. Conversely, we will now examine some cases in which the variation of the parameter does have an influence of the stationary velocity. Fig 5.19a examines the effect of the operating temperature. The variation in velocity as the initial temperature increases appears to resemble the profile of the composite specific heat. It remains relatively constant up to around 30 K and then begins to rise. However, in absolute terms, this variation is moderate. At 4.2 K, the velocity is approximately 4 cm/s, and at 50 K, it is around 5 cm/s. Fig 5.19b shows the variation with respect to the the applied magnetic field. Both the initial and the equilibrium velocities clearly increase together with the field. This profile is a result of the various effects that the magnetic field has on the thermal and electrical properties of the HTS tape. A higher magnetic field worsens the electrical resistivity of copper and, more significantly, that of the superconductor. It also causes the critical and current-sharing temperatures to shift towards lower values. As previously mentioned in the paragraph 5.3.1, this overall behaviour is why, from a protection standpoint, it is preferable for a quench to initiate in a region with a higher magnetic field rather than a lower one.

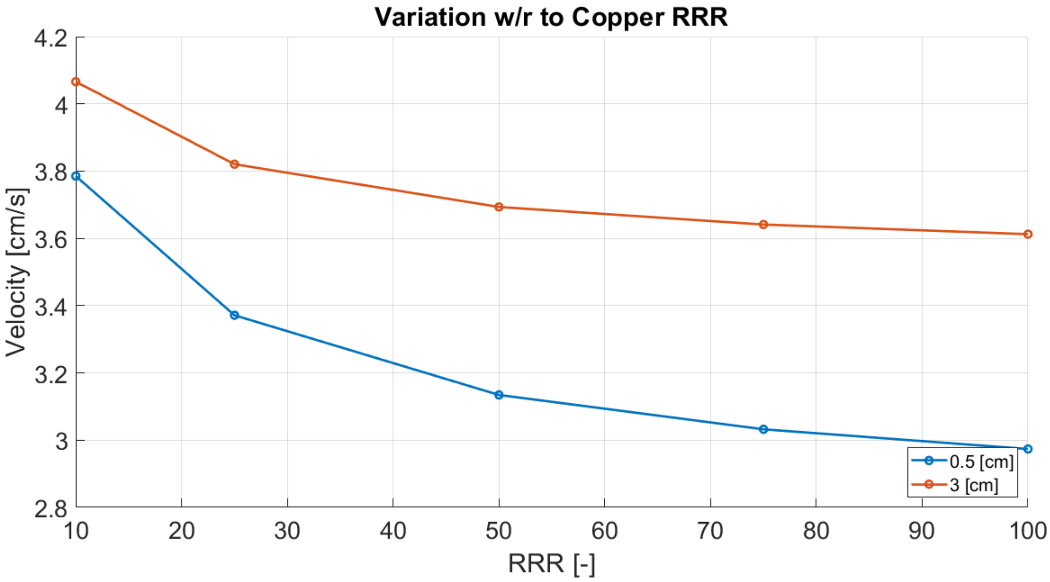

Figure 5.20: Variation with respect to copper RRR.

Another aspect that was considered is the variation due to the copper RRR. Also in this case the absolute variation is moderate and shows a decreasing pattern (see Figure 5.20). This observation could provide an explanation for the behavior of the maximum temperature as a function of RRR, as shown in Fig 5.15a. As the RRR increases, the quench velocity decreases, resulting in a slower rise of voltage and consequently a higher final maximum temperature. The last examined dependence concerns the operating current density. Equation (5.18) exhibits a linear relationship with respect to J_{op}. This behavior has also been confirmed through the numerical simulation. This dependence on the operating current density may be considered the most significant factor influencing the quench propagation velocity. Figure 5.21 illustrates that doubling the current density leads to a velocity value that is more than doubled.

As a conclusion, it is important to note the main characteristic of the *High Temperature Superconductor* cables is that, irrespective of the specific set of applied conditions (magnetic field, current density, RRR, etc.), the quench propagation velocity is orders of magnitude smaller than that of LTS (*Low Temperature Superconductor*). While LTS velocities range from tens to even hundreds of meters per second, we have observed in this section that HTS velocities barely reach values above a few centimeters per second. HTS magnets are notorious for being more stable (it is more difficult to initiate a quench) but once quenched, they are also more complicated to protect. What is evident is that, due to the extremely low propagation velocity, once a quench is initiated, it tends to remain localized, resulting in a hot spot that can reach temperatures higher than hundreds of degrees within a fraction of a second.

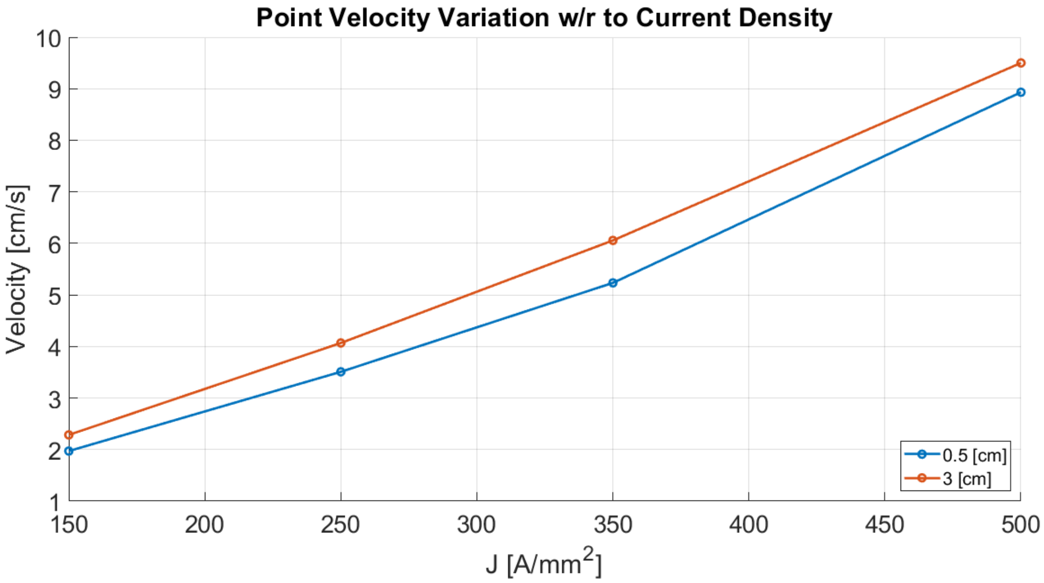

Figure 5.21: Variation with respect to J_{op}.

6 | Conclusions and future developments

Superconducting magnets and, in particular, solenoids will be essential components for the development of the Muon Collider. This collider is designed to accelerate, focus and collide bunches of counter-propagating muons and anti-muons. Muons have always been considered as a valuable option for a modern particle accelerator but the inherent difficulties associated with such a project have consistently hindered any potential progress towards its implementation. Muons are, indeed, unstable particles and decay in 2.2 μs into electrons and neutrinos and represent a paradigm shift from the well-established protons and electrons, which, in contrast, are stable particles and require no specific precautions in their handling. However, in recent times, the advancements in accelerator technologies, particularly in the field of superconducting magnets, have sparked a growing interest in this concept. A significant role in this regard is being played by HTS (High-Temperature Superconductors) superconductors. Propelled by investments in nuclear fusion, they are steadily gaining traction in the market and positioning themselves as a prominent technology for the future. The Muon Collider will be under evaluation for the next few years with the aim of assessing its feasibility, not only from a technical perspective but also considering its economic viability, and this thesis work fits precisely within this framework. In particular, this work has investigated the 6D Cooling stages of the Muon Collider and their solenoids. The analysis was based on input parameters from the US MAP study and encompassed two main aspects: the magnetic and mechanical considerations on one side, and the quench protection analysis on the other.

In the initial paragraphs of Chapter 4, the description of the analytical formulas, the FEM model in Comsol Multiphysics, and the methodology employed are provided. Finally, in Section 4.2.2, a comprehensive overview of the results is presented. The analysis sheds light not only on the characteristics of the 18 different types of solenoids involved but also, and perhaps more importantly, on their weak points. It becomes evident that certain magnet parameters need to be optimized from an energy, cost, and engineering perspective. The solenoids are found to have high values of self-inductance and stored magnetic energy.

Cell B1 alone, for example, has a stored energy of 44.5 MJ. As a reference, an LHC dipole, which is 15 m long and generates a field greater than 8 T, stores approximately 7 MJ of energy. It is crucial to emphasize the significance of these two parameters, particularly in the context of quench protection. Still considering the magnetic aspect, it is interesting to observe the difference between the peak value of the field on the axis compared to the value reached on the conductor. Depending on the stage and the solenoid, this ratio can be as high as approximately 3. This information is crucial because, although it may not be significant from a beam dynamics point of view, it is one of the most important parameters that a magnet designer should be concerned with. Moreover, the mechanical analysis has also brought to light certain points of concern. Several solenoids experience hoop stress values exceeding 150 MPa, which can be considered a threshold value indicating the necessity for a mechanical support structure. If the presence of the structure was already assumed to be necessary, the evaluated longitudinal force values (as high as 3700 tons), on the other hand, highlight the fact that this structure must be highly complex. The last aspect is related to the tensile radial stress state which some magnets experience. It has been emphasized that this condition is unfavorable for solenoids, and several possible solutions were presented to address this issue.

While this study has provided valuable insights and addressed important aspects, there are certain areas that were not included. These limitations should be taken into account for future research, and the following is a quick list of some of them. The roller boundary condition should be substituted with a more complete mechanical structure to have a more realistic representation of the full stress-strain state of the solenoids. Attention should be also given to the matching sections between different stages, as this would enable a comprehensive analysis of the magnetic field throughout the entire length of the cooling process. Lastly, it is crucial to incorporate the dipole component of the magnetic field.

As stated a few lines above, these solenoids need to be further optimized, and future development in this direction has already begun. In particular, the magneto-mechanical optimization process has been complemented by two studies. First, a sensitivity analysis on how and to what extent the magnetic fields are modified by changing the configuration of the magnets by a certain percentage. Secondly, a similar analysis has also been conducted on the Fourier spectrum of the sinusoidal on-axis and off-axis field, to establish the relationship between the configuration space of the solenoids and their field harmonics.

Chapter 5 provides an introductory yet comprehensive analysis of the quench protection aspects. The full analytical treatment is initially presented, followed by an exploration of the necessary approximations and simplifications which, it has been shown, are not only necessary but also vital in order to effectively represent the phenomenon using analytical tools. However, the main emphasis was placed on developing a one-dimensional Finite Element Method (FEM) simulation of a quench in an HTS cable. This simulation was not intended to serve as a comprehensive and complete numerical tool for analyzing the quench protection aspect. As stated in the introduction of Section 5.2, developing such a tool would have been excessively complex and beyond the scope of this thesis work, especially considering the existence of similar models already. However, the simulation was crucial for my personal understanding of the phenomenon and can serve as a solid foundation for future developments in this direction. The results presented in this chapter should be interpreted in light of the reasoning described above. These results are related to two distinct yet equally important considerations. The first aspect primarily focuses on the maximum temperature attained inside the cable, which is a significant concern during magnet quench events. The second involves the evaluation of the quench propagation velocity, which is vital for understanding the dynamics of the quench process. Lastly, it is worth highlighting the implementation of an application based on the existing simulation model. The aim of this application is to share and to provide a tool that can be accessed and utilized by anyone, even without the need for an expensive Comsol license.

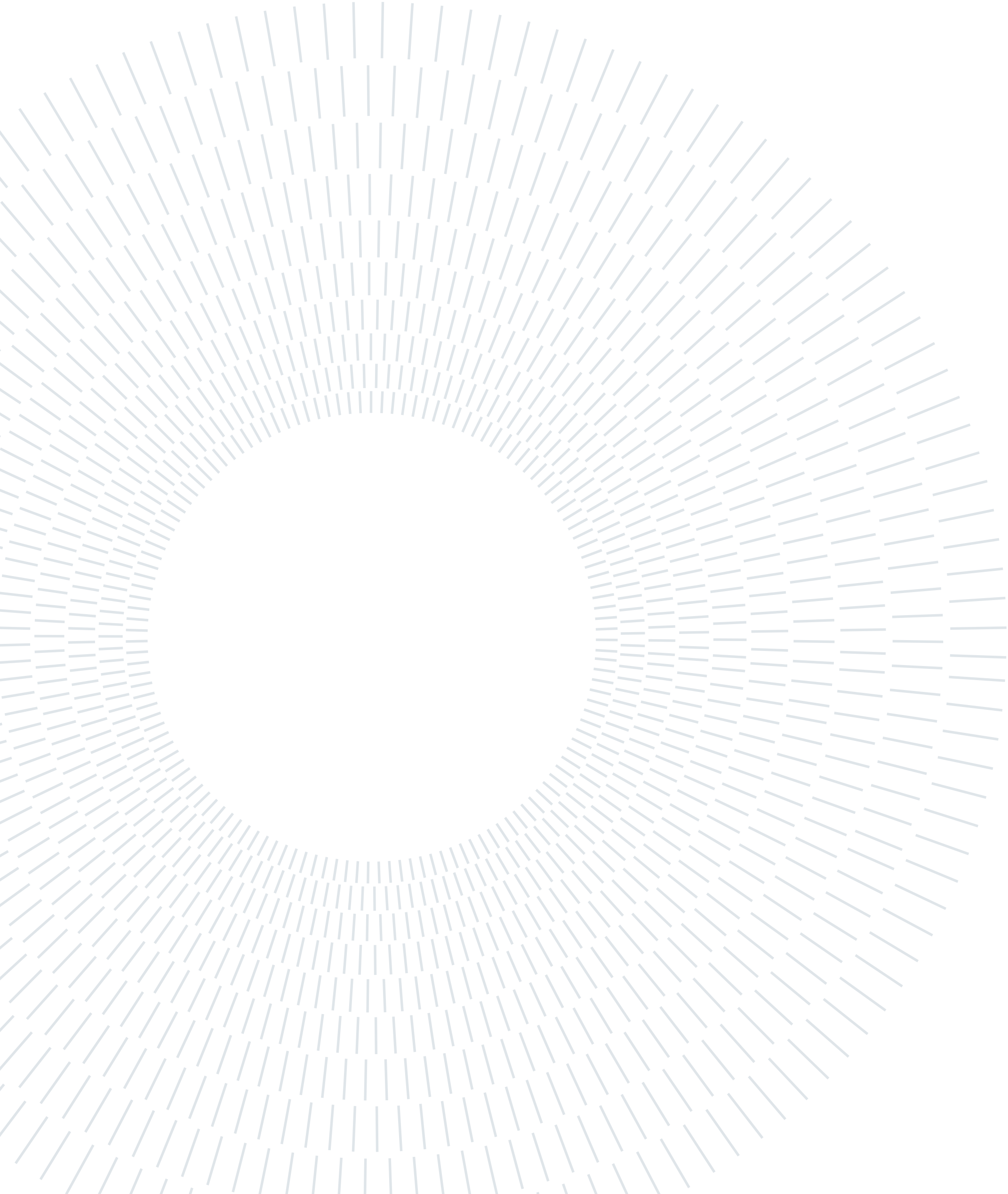

Bibliography

[1] In A. ROSE-INNES and E. RHODERICK, editors, *Introduction to Superconductivity (Second Edition)*. Pergamon, second edition edition, 1978. ISBN 978-0-08-021651-5. doi: https://doi.org/10.1016/B978-0-08-021651-5.50002-4. URL `https://www.sciencedirect.com/science/article/pii/B9780080216515500024`.

[2] *On Superconductivity and Superfluidity (What I Have and Have Not Managed to Do), As Well As on the 'Physical Minimum' at the Beginning of the 21st Century*, pages 1–34. Springer Berlin Heidelberg, Berlin, Heidelberg, 2009. ISBN 978-3-540-68008-6. doi: 10.1007/978-3-540-68008-6_1. URL `https://doi.org/10.1007/978-3-540-68008-6_1`.

[3] N. P. O. AB. The nobel prize in physics 1987. `https://www.nobelprize.org/prizes/physics/1987/summary/`, 2023. [Accessed: 25-Mar-2023].

[4] C. Aimè, A. Apyan, M. A. Mahmoud, N. Bartosik, A. Bertolin, M. Bonesini, S. Bottaro, D. Buttazzo, R. Capdevilla, M. Casarsa, L. Castelli, M. G. Catanesi, F. G. Celiberto, A. Cerri, C. Cesarotti, G. Chachamis, S. Chen, Y.-T. Chien, M. Chiesa, G. Collazuol, M. Costa, N. Craig, D. Curtin, S. Dasu, J. D. Blas, D. Denisov, H. Denizli, R. Dermisek, L. D. Luzio, B. D. Micco, K. Dienes, T. Dorigo, A. Ferrari, D. Fiorina, R. Franceschini, F. Garosi, A. Glioti, M. Greco, A. Greljo, R. Groeber, C. Grojean, J. Gu, T. Han, B. Henning, K. Hermanek, T. R. Holmes, S. Homiller, S. Jana, S. Jindariani, Y. Kahn, I. Karpov, W. Kilian, K. Kong, P. Koppenburg, K. Krizka, L. Lee, Q. Li, R. Lipton, Z. Liu, K. Long, I. Low, D. Lucchesi, Y. Ma, L. Ma, F. Maltoni, B. Mansoulie, L. Mantani, D. Marzocca, N. McGinnis, B. Mele, F. Meloni, C. Merlassino, A. Montella, M. Nardecchia, F. Nardi, P. Panci, S. P. Griso, G. Panico, R. Paparella, P. Paradisi, N. Pastrone, F. Piccinini, K. Potamianos, E. Radicioni, R. Rattazzi, D. Redigolo, L. Reina, J. Reuter, C. Riccardi, L. Ricci, U. van Rienen, L. Ristori, T. N. Robens, R. Ruiz, F. Sala, J. Salko, P. Salvini, E. Salvioni, D. Schulte, M. Selvaggi, A. Senol, L. Sestini, V. Sharma, J. Shu, R. Simoniello, G. H. Stark, D. Stolarski, S. Su, W. Su, O. Sumensari, X. Sun, R. Sundrum, J. Tang, A. Tesi,

B. Thomas, R. Torre, S. Trifinopoulos, I. Vai, A. Valenti, L. Vittorio, L. Wang, Y. Wu, A. Wulzer, X. Zhao, and J. Zurita. Muon collider physics summary, 2022.

[5] N. W. Ashcroft and N. D. Mermin. *Solid State Physics*. Cengage Learning, Philadelphia, PA, 1st edition, 1976. ISBN 978-0030839931.

[6] J. Bardeen, G. Rickayzen, and L. Tewordt. Theory of the thermal conductivity of superconductors. *Phys. Rev.*, 113:982–994, Feb 1959. doi: 10.1103/PhysRev.113.982. URL `https://link.aps.org/doi/10.1103/PhysRev.113.982`.

[7] J. G. Bednorz and K. A. Müller. Possible hightc superconductivity in the balacuo system. *Zeitschrift für Physik B Condensed Matter*, 64(2):189–193, 1986. ISSN 1431-584X. doi: 10.1007/BF01303701. URL `https://doi.org/10.1007/BF01303701`.

[8] R. N. Bhattacharya and M. P. Paranthaman. *High Temperature Superconductors*. Wiley-VCH, 1 edition, 2010. ISBN 978-3-527-40827-6.

[9] J. Black and R. Schaffer. Topological superconductivity. `https://saasfee15.manep.ch/pdf/Black-Schaffer-1.pdf`, Year. Accessed on: Month Day, Year.

[10] L. Bottura. Magnet quench 101. *WAMSDO, CERN*, 2013.

[11] L. Bottura, D. Aguglia, B. Auchmann, T. Arndt, J. Béard, A. Bersani, F. Boattini, M. Breschi, B. Caiffi, X. Chaud, M. Dam, F. Debray, E. De Matteis, A. Dudarev, S. Farinon, A. Kario, R. Losito, S. Mariotto, R. Musenich, and Y. Yang. A work proposal for a collaborative study of magnet technology for a future muon collider. 03 2022.

[12] R. W. Chabay and B. A. Sherwood. *Matter interactions (2th ed.)*. Hoboken, NJ: John Wiley Sons,, 2007. ISBN 9780470108314.

[13] S. Commission. Safety rules for the use of static magnetic fields at cern. Safety Instruction IS36, CERN, Geneva, Switzerland, June 2005. Rev. 2.

[14] W. Commons. File:solenoid and ampere law - 2.png — wikimedia commons, the free media repository, 2023. URL `https://commons.wikimedia.org/w/index.php?title=File:Solenoid_and_Ampere_Law_-_2.png&oldid=732631663`. [Online; accessed 31-May-2023].

[15] H. Davy. Xviii on the application of liquids formed by the condensation of gases as mechanical agents. *Philosophical Transactions of the Royal Society of London*, 113:199–205, 1823. doi: 10.1098/rstl.1823.0020. URL `https://royalsocietypublishing.org/doi/abs/10.1098/rstl.1823.0020`.

[16] H. Davy. On the application of liquids formed by the condensation of gases as a vehicle for transmitting power. *Philosophical Transactions of the Royal Society of London*, 114:1–16, 1824. doi: 10.1098/rstl.1824.0001.

[17] R. Fernow. Classification of periodic alternating-solenoid lattices. 01 2002.

[18] A. Goyal, editor. *Second-Generation HTS Conductors*. Springer New York, NY, 2005. ISBN 978-1-4020-8117-0. doi: 10.1007/b106635. URL `https://doi.org/10.1007/b106635`. Hardcover ISBN: 978-1-4020-8117-0, Softcover ISBN: 978-1-4419-5478-7, eBook ISBN: 978-0-387-25839-3.

[19] C. B.-S. . Hankwang Own work. Joule-thomson coefficients for various gases at 1.013 bar (reduced vertical scale); data source http://webbook.nist.gov/chemistry/fluid/, 2010. URL `https://commons.wikimedia.org/w/index.php?curid=10251180`. [Online; accessed 2022-12-28].

[20] R. M. Hazen. *The breakthrough : the race for the superconductor / Robert M. Hazen*. Summit Books New York, 1988. ISBN 0671658298.

[21] HyperPhysics. BCS Theory. `http://hyperphysics.phy-astr.gsu.edu/hbase/Solids/bcs.html`, n.d. Accessed: 6 April 2023.

[22] Y. Iwasa. *Case Studies in Superconducting Magnets: Design and Operational Issues*. Selected Topics in Superconductivity. Springer New York, 2 edition, 2009. doi: 10.1007/b112047. URL `https://doi.org/10.1007/b112047`.

[23] Q.-G. Lin. An approach to the magnetic field of a finite solenoid with a circular cross-section. *European Journal of Physics*, 42(3):035206, March 2021. doi: 10.1088/1361-6404/abd4c8.

[24] F. London, H. London, and F. A. Lindemann. The electromagnetic equations of the supraconductor. *Proceedings of the Royal Society of London. Series A - Mathematical and Physical Sciences*, 149(866):71–88, 1935. doi: 10.1098/rspa.1935.0048. URL `https://royalsocietypublishing.org/doi/abs/10.1098/rspa.1935.0048`.

[25] K. R. Long, D. Lucchesi, M. A. Palmer, N. Pastrone, D. Schulte, and V. Shiltsev. Muon colliders to expand frontiers of particle physics. *Nature Physics*, 17(3):289–292, jan 2021. doi: 10.1038/s41567-020-01130-x. URL `https://doi.org/10.1038%2Fs41567-020-01130-x`.

[26] J. Loram, K. A. Mirza, and J. Waldram. Scaling laws in high-temperature superconductors. *Journal of Superconductivity*, 6(2):285–302, 1993.

[27] D. Newbold. Introduction. In N. Mounet, editor, *European Strategy for Particle Physics - Accelerator R&D Roadmap*, volume 1 of *CERN Yellow Reports: Monographs*, page 1. CERN, 2022. ISBN 978-92-9083-731-5. doi: 10.23731/CYRM-2022-001.1. URL `https://cds.cern.ch/record/2764789`. © CERN, 2022. Published by CERN under the Creative Commons Attribution 4.0 license.

[28] Nobel Prize Outreach AB. Heike kamerlingh onnes - facts, 2023. URL `https://www.nobelprize.org/prizes/physics/1913/onnes/facts/`. Accessed: April 24, 2023.

[29] M. Palmer. The us muon accelerator program. *arXiv preprint arXiv:1502.03454*, 2015.

[30] R. B. Palmer. Muon Colliders. *Rev. Accel. Sci. Tech.*, 7:137–159, 2014. doi: 10.1142/S1793626814300072.

[31] A. S. Randy Simon. *Superconductors: Conquering Technology's New Frontier*. Springer New York, NY, 1 edition, 1988. ISBN 978-0-306-42959-0.

[32] S. Reif-Acherman. Liquefaction of gases and discovery of superconductivity: two very closely scientific achievements in low temperature physics. *Revista Brasileira de Ensino de Física [online]*, 33(2):1–17, 7 2011. Available from: <https://doi.org/10.1590/S1806-11172011000200016>. Epub 02 Sept 2011. ISSN 1806-9126. https://doi.org/10.1590/S1806-11172011000200016.

[33] S. Reif-Acherman. Studies on the temperature dependence of electric conductivity for metals in the nineteenth century: a neglected chapter in the history of superconductivity. *Revista Brasileira de Ensino de Física*, 33:4602–4302, 12 2011. doi: 10.1590/S1806-11172011000400020.

[34] C. Rey and A. Malozemoff. 2 - fundamentals of superconductivity. In C. Rey, editor, *Superconductors in the Power Grid*, Woodhead Publishing Series in Energy, pages 29–73. Woodhead Publishing, 2015. ISBN 978-1-78242-029-3. doi: https://doi.org/10.1016/B978-1-78242-029-3.00002-9. URL `https://www.sciencedirect.com/science/article/pii/B9781782420293000029`.

[35] E. B. Rosa and F. W. Grover. Formulas and tables for the calculation of mutual and self-inductance (revised). *Bulletin of the Bureau of Standards*, 8(1):1–15, January 1912. URL `http://dx.doi.org/10.6028/bulletin.185`.

[36] F. J. Saura, R. Franqueira, D. Calzolari, M. Calviani, A. Lechner, R. Losito, D. Schulte, A. M. Krainer, and C. Rogers. Muon Collider Graphite Tar-

get Studies and Demonstrator Layout Possibilities at CERN. In JACoW, editor, *Proceedings of the 13th International Particle Accelerator Conference (IPAC'22)*, Bangkok, Thailand, 2022. JACoW Publishing. ISBN 978-3-95450-227-1. doi: 10.18429/JACoW-IPAC2022-THPOTK052. URL `https://doi.org/10.18429/JACoW-IPAC2022-THPOTK052`. Paper presented at the 13th International Particle Accelerator Conference (IPAC'22), Bangkok, Thailand.

[37] C. Senatore, C. Barth, M. Bonura, M. Kulich, and G. Mondonico. Field and temperature scaling of the critical current density in commercial rebco coated conductors. *Superconductor Science and Technology*, 31(6):063002, 2018.

[38] R. G. Sharma. *The Phenomenon of Superconductivity and Type II Superconductors*, pages 15–72. Springer International Publishing, Cham, 2021. ISBN 978-3-030-75672-7. doi: 10.1007/978-3-030-75672-7_2. URL `https://doi.org/10.1007/978-3-030-75672-7_2`.

[39] D. Stratakis and R. B. Palmer. Rectilinear six-dimensional ionization cooling channel for a muon collider: A theoretical and numerical study. *Phys. Rev. ST Accel. Beams*, 18:031003, Mar 2015. doi: 10.1103/PhysRevSTAB.18.031003. URL `https://link.aps.org/doi/10.1103/PhysRevSTAB.18.031003`.

[40] G. Succi, A. Ballarino, and Y. Yang. Scaling law of the anisotropic magnetic field dependence of the critical current of rebco coated conductors. In *HiTAT workshop*. CERN, March 2023.

[41] D. van Delft and P. Kes. The discovery of superconductivity. *Physics Today*, 63(9): 38–43, 2010. doi: 10.1063/1.3490499. URL `https://doi.org/10.1063/1.3490499`.

[42] Y. Wang. *Fundamental Elements of Applied Superconductivity in Electrical Engineering*. Wiley, 2013. ISBN 9781118451144. URL `https://books.google.fr/books?id=N18DDQAAQBAJ`.

[43] Wikimedia Commons. File:timeline of superconductivity from 1900 to 2015.svg — wikimedia commons, 2023. URL `https://commons.wikimedia.org/wiki/File:Timeline_of_Superconductivity_from_1900_to_2015.svg`. [Online; accessed 1-April-2023].

[44] Wikipedia contributors. Thermodynamic free energy — Wikipedia, the free encyclopedia, 2022. URL `https://en.wikipedia.org/w/index.php?title=Thermodynamic_free_energy&oldid=1115092061`. [Online; accessed 14-February-2023].

[45] Wikipedia contributors. Phase transition — Wikipedia, the free encyclopedia, 2022. URL `https://en.wikipedia.org/w/index.php?title=Phase_transition&oldid=1126050973`. [Online; accessed 18-February-2023].

[46] Wikipedia contributors. Cryogenics — Wikipedia, the free encyclopedia, 2022. URL `https://en.wikipedia.org/w/index.php?title=Cryogenics&oldid=1128020014`. [Online; accessed 28-December-2022].

[47] Wikipedia contributors. Joule–thomson effect — Wikipedia, the free encyclopedia, 2022. URL `https://en.wikipedia.org/w/index.php?title=Joule%E2%80%93Thomson_effect&oldid=1123584995`. [Online; accessed 2-January-2023].

[48] Wikipedia contributors. Hampson–linde cycle — Wikipedia, the free encyclopedia, 2022. URL `https://en.wikipedia.org/w/index.php?title=Hampson%E2%80%93Linde_cycle&oldid=1100205383`. [Online; accessed 29-December-2022].

[49] Wikipedia contributors. Inductance — Wikipedia, the free encyclopedia, 2023. URL `https://en.wikipedia.org/w/index.php?title=Inductance&oldid=1154394294`. [Online; accessed 1-June-2023].

[50] Wikipedia contributors. Bcs theory — Wikipedia, the free encyclopedia, 2023. URL `https://en.wikipedia.org/w/index.php?title=BCS_theory&oldid=1147733083`. [Online; accessed 6-April-2023].

[51] M. Wilson. *Superconducting Magnets*. Monographs on cryogenics. Clarendon Press, 1983. ISBN 9780198548102. URL `https://books.google.it/books?id=AObvAAAAMAAJ`.

A | 1D Quench HTS Simulator: Instructions

This application simulates a quench in an 1D HTS (High Temperature Superconductor). For a better insight on the physics and on the design choices taken to implement this application refer to Chapter 5.

A.1. Main

In the *Main* window, the user can find the main parameters that can be changed to personalize the desired simulation. Furthermore, they can let the simulation run using the "Compute" bottom, or they can view the 1D geometry by pressing the "Geometry" button.

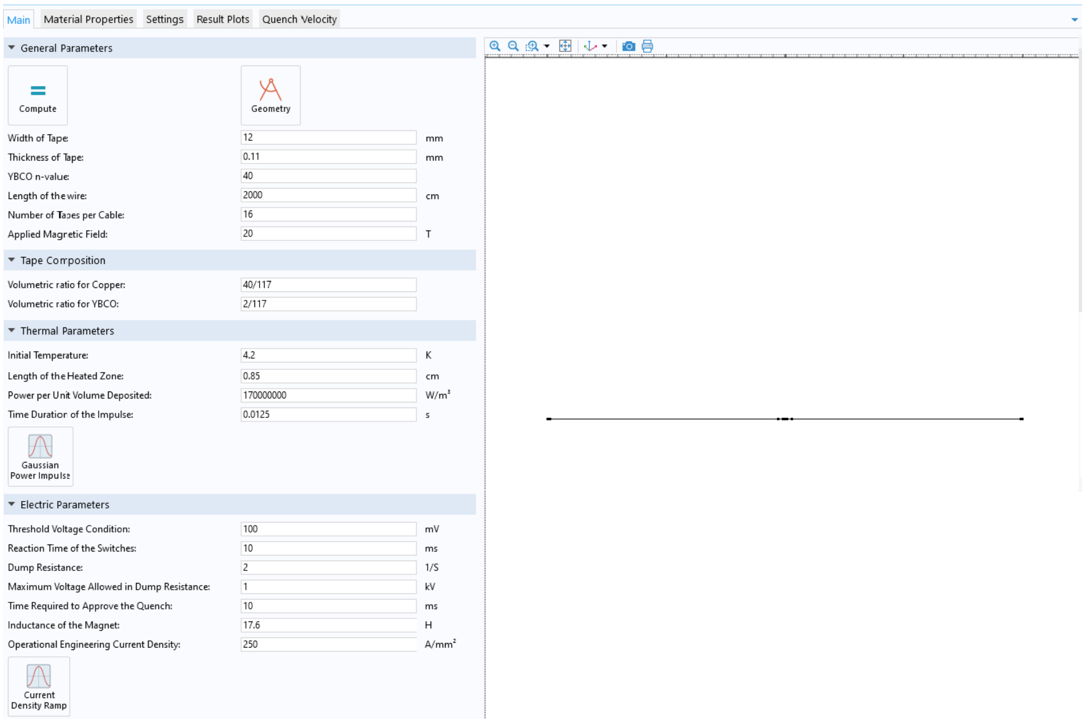

Width of Tape: 12 mm
Thickness of Tape: 0.11 mm
YBCO n-value: 40
Length of the wire: 2000 cm
Number of Tapes per Cable: 16
Applied Magnetic Field: 20 T

Volumetric ratio for Copper: 40/117
Volumetric ratio for YBCO: 2/117

Initial Temperature: 4.2 K
Length of the Heated Zone: 0.85 cm
Power per Unit Volume Deposited: 170000000 W/m³
Time Duration of the Impulse: 0.0125 s

Threshold Voltage Condition: 100 mV
Reaction Time of the Switches: 10 ms
Dump Resistance: 2 1/S
Maximum Voltage Allowed in Dump Resistance: 1 kV
Time Required to Approve the Quench: 10 ms
Inductance of the Magnet: 17.6 H
Operational Engineering Current Density: 250 A/mm²

Figure A.1: *Main* window interface.

General Parameters The user can choose the dimensions of the HTS tape by means of "Width of Tape" and "Thickness of Tape". The default values are, respectively, 12 mm and 0.11 mm. "YBCO n-value" is the n-value of the superconductor which enters inside the power-law. To shorten or lengthen the length of the domain and hence of the tape, change the "Length of the wire" option.To maintain the system adiabatic, it is preferable to simulate a long cable ($\sim$ 20 m). The "Number of Tapes per Cable" allows for the composition of a cable with this number of tapes, thereby reducing the inductance of the solenoid (the inductance scales as "Number of Tapes per Cable"^{2}). The "Applied Magnetic Field" is the constant magnetic field at which the cable is subjected to.

Tape Composition These are the volumetric ratios of the tape components (YBCO, Copper and Hastelloy). The Hastelloy ratio is obtained by complementing the sum of Copper and YBCO to 1. Please make sure that the sum of the ratios of Copper and YBCO is smaller than or equal to 1.

Thermal Parameters The "Initial Temperature" is both the initial temperature for the whole domain but it is also the temperature at which the two domain extremities are fixed to. The next parameters define the input disturbance which could be able to initiate the quench. It is a Gaussian power density impulse

$$Q(t) = P_{\mathrm{q}}\, e^{-\frac{(t-t_0)^2}{2\Delta t^2}}. \tag{A.1}$$

"Power per Unit Volume Deposited" corresponds to P_q, while Δt to "Time Duration of the Impulse". The actual length of the disturbance can be change by "Length of the Heated Zone". The bottom shows the shape of the impulse.

Electric Parameters "Threshold Voltage Condition" controls the value of the voltage at which the first alarm bell of the safety system goes off. Once the voltage condition is reached a timer starts. If after a time equivalent to "Time Required to Approve the Quench" the voltage is still above the voltage threshold, the safety system activates the switches. The switches activate after "Reaction Time of the Switches". The safety system can operate under two different configurations: the user can choose to set the resistance of the dump resistor ("Dump Resistance") or fix the maximum voltage across the dump resistor ("Maximum Voltage Allowed in Dump Resistance"). The "Inductance of the Magnet" set the value of the inductance of the lumped inductor in the electric circuit. If "Number of Tapes per Cable" $>$ 1, then the inductance is divided by that value squared. "Operational Engineering Current Density" is the current density which flows inside each tape. The bottom allows to see the current density ramp profile.

A.2. Material Properties

In the *Material Properties* window the user has the possibility to change some parameters that influence the materials behaviours.

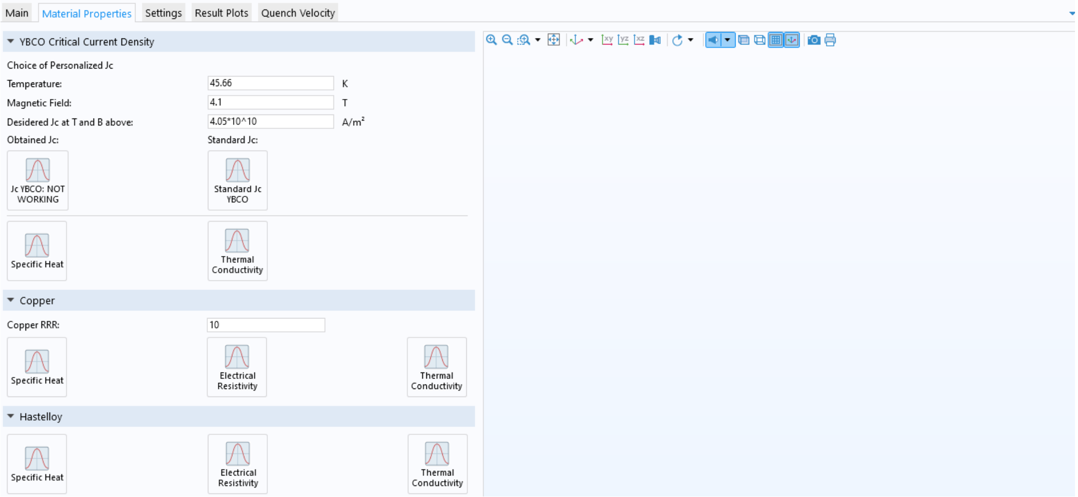

Temperature: 45.66 K
Magnetic Field: 4.1 T
Desidered Jc at T and B above: 4.05*10^10 A/m²
Copper RRR: 10

Figure A.2: *Material Properties* window interface.

YBCO Critical Current Density Here the user can decide to personalize its own J_c. Embedded in the model there is a fitted curve of the critical current of YBCO. The user can decide its own value of the critical current in "Desired Jc at T and B above" when the superconductor is subjected to "Magnetic Field" at the operating temperature "Temperature". The model adapts its J_c such that the personalized J_c passes through "Desired Jc at T and B above". The bottoms show the indicated thermal properties.

Copper The user can choose the copper RRR (Residual-resistivity ratio) by changing "Copper RRR". The bottoms show the indicated thermal and electrical properties.

Hastelloy The bottoms show the indicated thermal and electrical properties.

A.3. Settings

In the *Setting* window the user can personalize the type of simulation that is performed and change some solver settings and parameters.

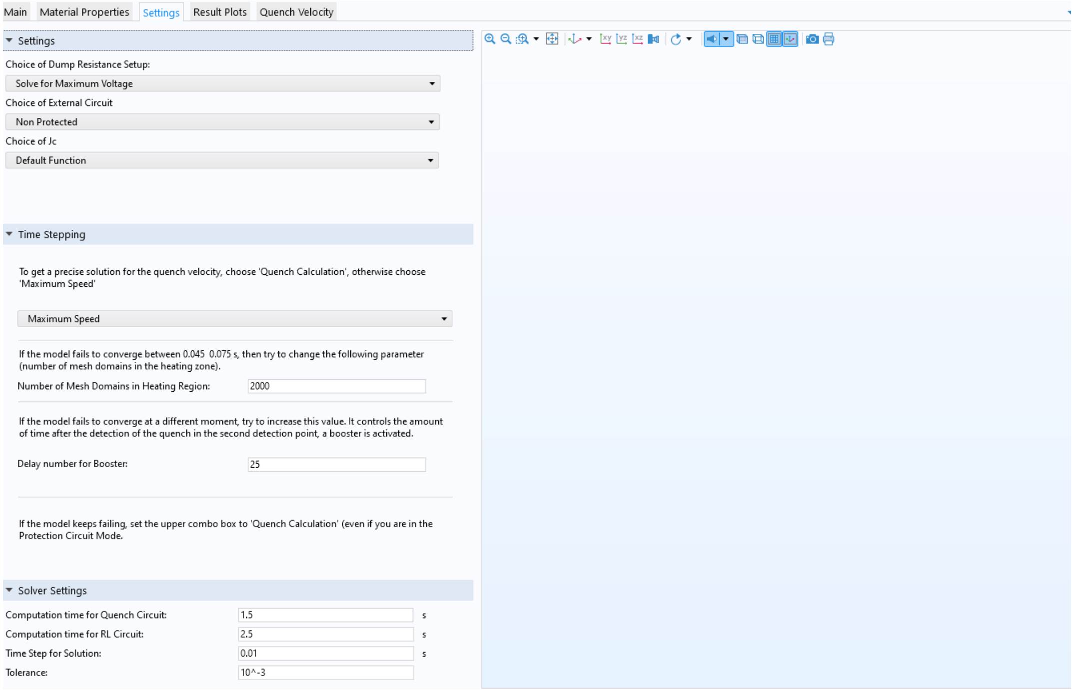

Settings

Choice of Dump Resistance Setup: Solve for Maximum Voltage

Choice of External Circuit: Non Protected

Choice of Jc: Default Function

Time Stepping

To get a precise solution for the quench velocity, choose 'Quench Calculation', otherwise choose 'Maximum Speed'

Maximum Speed

If the model fails to converge between 0.045 0.075 s, then try to change the following parameter (number of mesh domains in the heating zone).

Number of Mesh Domains in Heating Region: 2000

If the model fails to converge at a different moment, try to increase this value. It controls the amount of time after the detection of the quench in the second detection point, a booster is activated.

Delay number for Booster: 25

If the model keeps failing, set the upper combo box to 'Quench Calculation' (even if you are in the Protection Circuit Mode.

Solver Settings

Computation time for Quench Circuit: 1.5 s

Computation time for RL Circuit: 2.5 s

Time Step for Solution: 0.01 s

Tolerance: 10^-3

Figure A.3: *Setting* window interface.

Settings If the "Choice of Dump Resistance Setup" is set to "Solve for Maximum Voltage" the dump resistor's resistance is calculated by the model in such a way to guarantee that the maximum value of the voltage across it does not exceed "Maximum Voltage Allowed in Dump Resistance". If instead, it is set to "Solve for Dump Resistance Value", the dump resistance simply becomes "Dump Resistance".

If the "Choice of External Circuit" is set to "Protected by Dump Resistor", the magnet is protected by the safety circuit and its stored magnetic energy is dissipated on the dump resistor. If it is set to "Non Protected", the safety circuit is deactivated and the simulation is suited for the quench velocity evaluation.

If the "Choice of Jc" is set to "Default Function", the critical current density which is used by the model is the default function. If it is set to "User Defined Function", the function defined in the *Material Properties*-YBCO Critical Current Density node is used.

Time Stepping Here the user can use some strategies when the simulation fails to converge. It is worth noting that this model can accept an extensive range of parameters as input. Therefore, there may be instances where it does not converge for certain configurations of these parameters. Follow the advises given in this section to try to fix the convergence issues.

Solver Settings "Computation time for Quench Circuit" determines the simulation time when the "Choice of External Circuit" is set to "Non Protected". Typically, 1.5 s is enough but it should be increased when the quench propagation velocity is expected to be particularly low.

"Computation time for RL Circuit" determines the simulation time when the "Choice of External Circuit" is set to "Protected by Dump Resistor". Typically, a duration of 2.5 seconds is sufficient to capture the maximum temperature. However, if the user wish to observe the decay of certain parameters such as voltage or temperature, the computation time can be increased accordingly.

"Time Step for Solution" is the parameter that determines the frequency at which the solution is outputted, specifying the time interval between each output. "Tolerance" is the solver tolerance. Reasonable values are 10^{-3} for "Protected by Dump Resistor" and 10^{-4} for "Non Protected". However, if a higher level of precision is required, the tolerance can be decreased to 10^{-4} or even lower values also in the first scenario. It is useful to remind that decreasing the tolerance increases the probability of non convergence.

A.4. Result Plots

In the *Result Plots* window, the user can visualize a collection of pre-defined plots. These plots are categorized based on their relevant category, such as thermal, electric, etc. To view a plot in the graphic window on the right, simply press the corresponding button associated with that plot.

A.5. Quench Velocity

In the *Quench Velocity* window the user can evaluate the quench propagation velocities in eight different subsequent intervals (0.5 cm long). It is sufficient to press the "Evaluate Velocities" bottom and a table with the eight velocities will appear below. Please use this feature only if the "Choice of External Circuit" is set to "Non Protected".

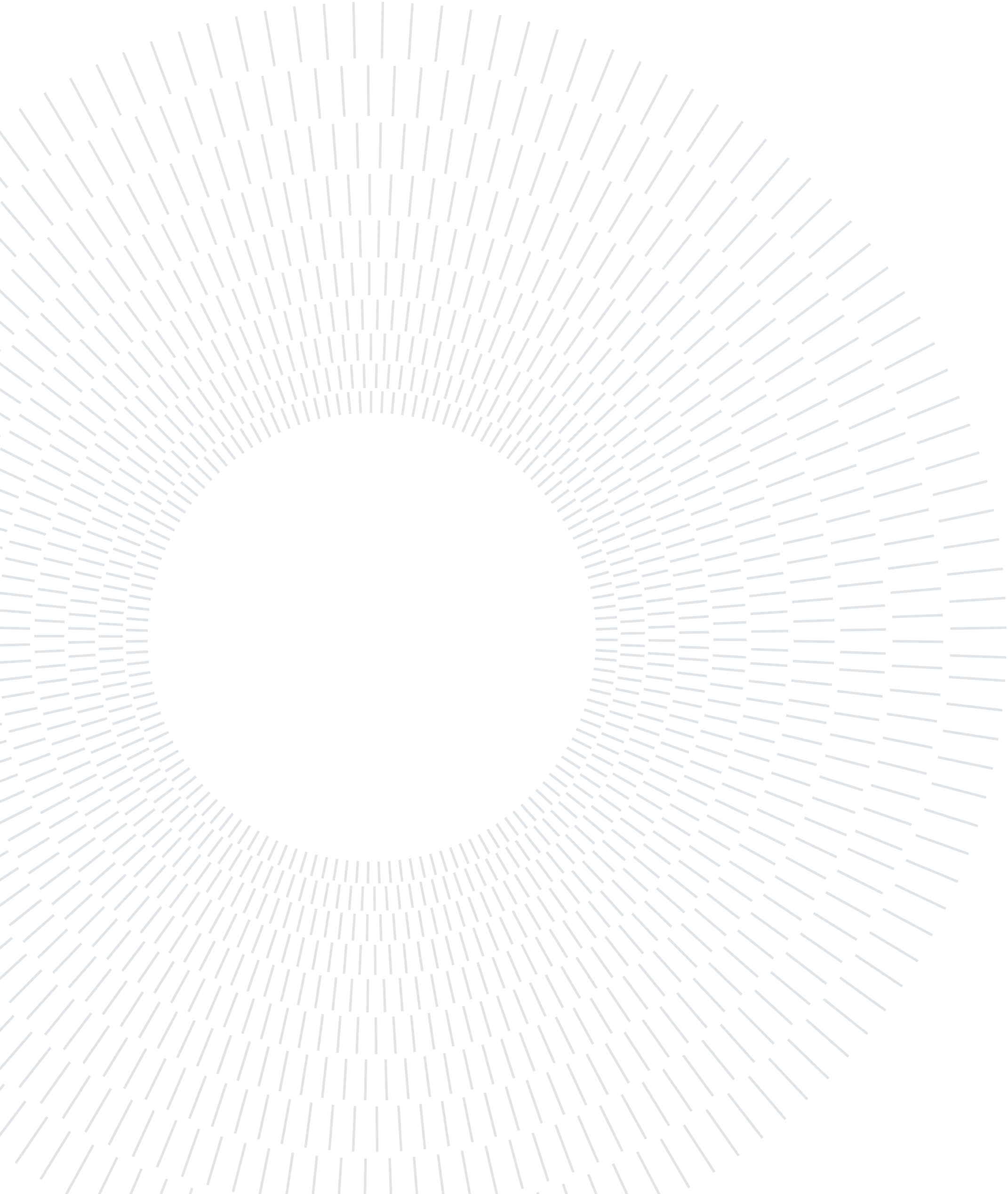

List of Figures

List of Tables

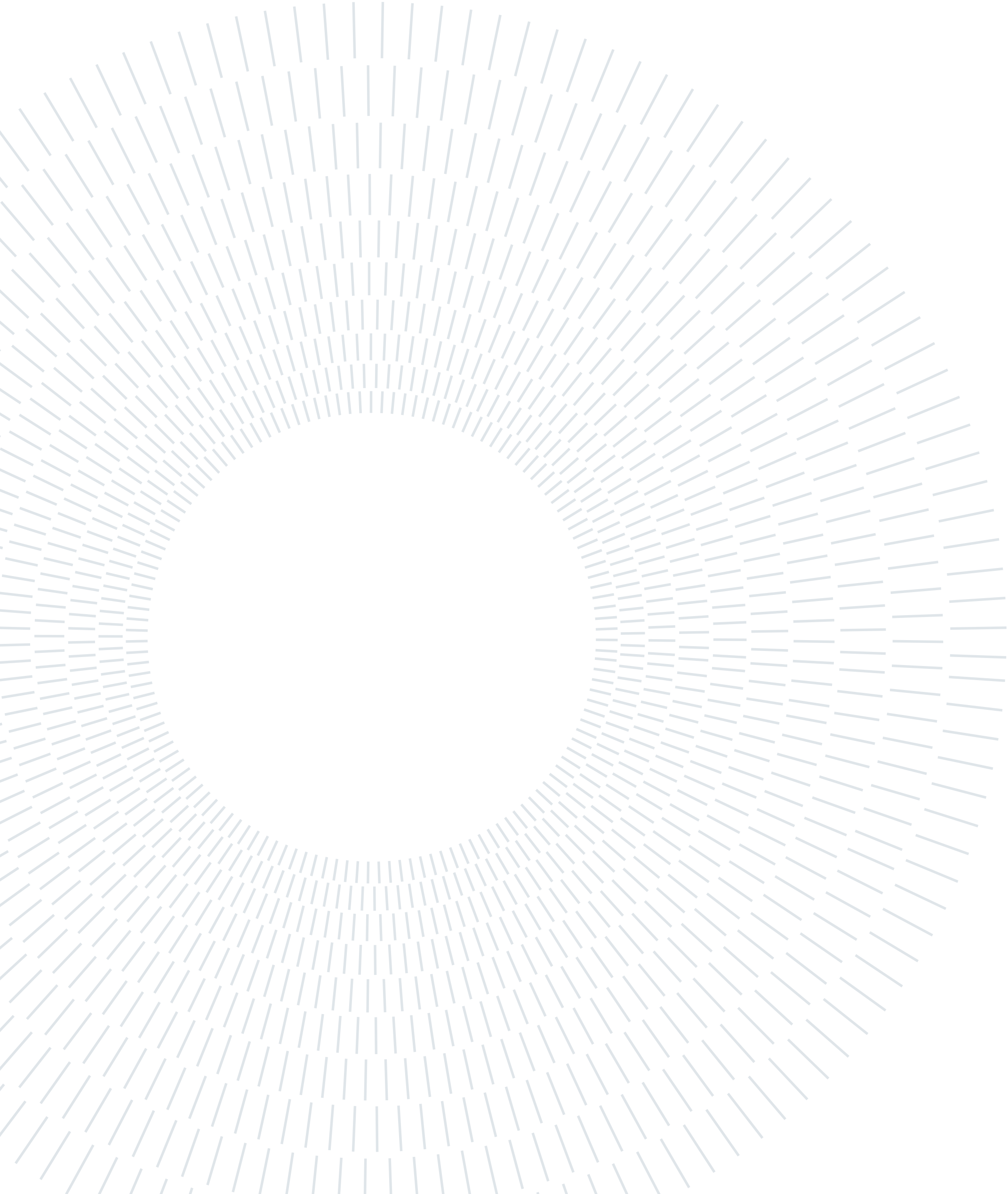

List of Symbols

Variable	Description	SI unit
$\boldsymbol{B}$	magnetic flux density	T
$\dot{\boldsymbol{B}}$	time derivative of magnetic flux density	$\mathrm{T/m}$
$\boldsymbol{H}$	magnetic field strength	$\mathrm{A/m}$
$\dot{\boldsymbol{H}}$	time derivative of magnetic flux density	$\mathrm{A/m\,s}$
$\boldsymbol{M}$	induced magnetization	$\mathrm{A/m}$
$\boldsymbol{A}$	vector potential	$\mathrm{A/m}$
μ_0	vacuum permeability	$\mathrm{kg\,m/s^2A^2}$
T	temperature field	K
μ_{JT}	Joule-Thomson coefficient	$\mathrm{K/Pa}$
P	pressure	Pa
V	volume	$\mathrm{m^3}$
C_p	heat capacity at constant pressure	$\mathrm{J/kg\,K}$
C_s	heat capacity at constant pressure of superconducting phase	$\mathrm{J/kg\,K}$
C_n	heat capacity at constant pressure of normal phase	$\mathrm{J/kg\,K}$
α	thermal expansion coefficient	$\mathrm{1/K}$
T_c	critical temperature	K
H_c	critical magnetic field strength	$\mathrm{A/m}$
J_c	critical current density	$\mathrm{A/m^2}$
$\boldsymbol{J}$	current density	$\mathrm{A/m^2}$
$\boldsymbol{J_s}$	superconducting current density	$\mathrm{A/m^2}$
$\boldsymbol{J_n}$	normal current density	$\mathrm{A/m^2}$
g	Gibbs free energy density	$\mathrm{J/m^3}$
g_s	Gibbs free energy density of superconducting phase	$\mathrm{J/m^3}$
g_n	Gibbs free energy density of normal phase	$\mathrm{J/m^3}$
G	Gibbs free energy	$\mathrm{J/mol}$

U	internal energy	J
S	entropy	J/K
s	entropy density	$\mathrm{J}/\mathrm{K\,m^3}$
m	magnetic moment	$\mathrm{Am^2}$
ν	specific volume	$\mathrm{m^3}/\mathrm{kg}$
L	latent heat	J/kg
x	superconducting-to-normal electrons ratio	-
m	mass	kg
$\boldsymbol{v}$	velocity	m/s
$\dot{\boldsymbol{v}}$	acceleration	$\mathrm{m}/\mathrm{s^2}$
n_s	superconducting electron number density	$1/\mathrm{m^3}$
e	elementary charge	C
$\boldsymbol{E}$	electric field	V/m
c	speed of light	m/s
λ	characteristic length	m
Ψ	order parameter	$\mathrm{J}^{1/2}$
$\hbar$	reduced Planck constant	Js
F	Helmotz free energy density	$\mathrm{J}/\mathrm{m^3}$
$\varkappa$	GL parameter	-
ξ	coherence length	m
Υ	antisymmetrizer	-
$\boldsymbol{f}_L$	Lorentz force density	$\mathrm{N}/\mathrm{m^3}$
ϕ_0	fluxon	T
n	superconductor n-value	-
I_c	critical current	A
B_{irr}	irreversibility field	T
$\hat{s}$	first Mandelstam variable	J^2
β	beta function	m
ϵ	emittance	m
R_i	inner radius	m
R_f	outer radius	m
L	inductance	H
V	voltage	V

R	resistance	Ω
M	mutual inductance	H
E_m	stored magnetic energy	J
$\boldsymbol{F}_L$	Lorentz force density	N/m^3
$\underline{\underline{\sigma}}$	stress tensor	Pa
σ_r	radial stress	Pa
σ_θ	circumferential stress	Pa
σ_z	axial stress	Pa
τ_{rz}	shear stress	Pa
E	Young modulus	Pa
v	Poisson ratio	-
$\underline{\underline{S}}$	compliance matrix	$1/\mathrm{Pa}$
ϵ_r	radial strain	-
ϵ_θ	circumferential strain	-
ϵ_z	axial strain	-
γ_{rz}	shear strain	-
ζ_r	normalized radial stress	-
ζ_θ	normalized circumferential stress	-
L_{cell}	length of a cell	m
$\boldsymbol{u}$	displacement field	m
k	thermal conductivity	J/mK
g_d	disturbance power density	W/m^3
g_c	cooling power density	W/m^3
T_∞	coolant bulk temperature	K
ρ	electrical resistivity	m/S
A	conductor cross sectional area	m^2
J_{op}	operational current density	A/m^2
τ_{delay}	delay time in saf.circ. activation	s
$\tau_{circuit}$	time constant of RL circuit	s
f_i	volume fraction of a layer	-
Δe_h	safety margin	J/m^3
T_{cs}	current-sharing temperature	K
RRR	residual-resistance ratio	-

v_{ad}	quench adiabatic velocity	$^{\mathrm{m}}/_{\mathrm{m}}$
P_q	Gaussian peak power density	$^{\mathrm{W}}/_{\mathrm{m}^3}$
L_q	disturbance length	m
Δt	disturbance standard deviation	s

Acknowledgements

Dopo innumerevoli pagine scritte in inglese, mi si conceda di fare i ringraziamenti in italiano.

Per primi vorrei ringraziare i miei supervisori, per la loro guida saggia, il loro sostegno costante e i preziosi consigli. Il prof. Marco Beghi, il quale ha avuto fiducia in me e dei suoi colleghi al di fuori del Politecnico, e che per questo mi ha permesso di fare questa incredibile avventura lunga quasi un anno. Il Prof. Lucio Rossi e il Prof. Marco Statera. Il primo per l'instancabile costanza con la quale persegue il suo lavoro e per questo esempio per tutti, giovani e non. Il secondo per la sua professionalità e conoscenza. Vorrei ringraziare Luca Bottura e Bernardo Bordini per essersi presi "scientificamente" cura di me durante i miei 4 mesi al Cern. In particolare Luca per la sua pacatezza, con la quale riesce sempre ad infondere fiducia e Bernardo per la sua implacabile curiosità (ma soprattutto per le ore spese insieme a combattere contro Comsol).

Grazie ai miei colleghi al LASA, Lorenzo, Anna Giulia, Gabriele, Samuele e tutti gli altri. Un ringraziamento speciale a Stefano, da me soprannominato "mentore di Matlab", per l'infinita lista di consigli che mi ha saputo dare.

I would like to extend a special thanks to Siara, my colleague at CERN, who not only provided invaluable scientific guidance but also gave me a glimpse to new cultures and traditions beyond Italy. Thanks also for the time spent correcting this thesis.

Grazie anche a Xu Yu, il coinquilino che tutti vorrebbero.

Grazie ai miei amici. Alberto, Alessandro, Davide, Giorgio, Luca, Pietro, Tommaso e tutti gli altri. Amici da una vita e amici per la vita. Grazie per il supporto, grazie per aver compreso quelle volte in cui era impossibile uscire perchè un esame era troppo vicino e grazie soprattutto per quelle volte in cui, al contrario, siete stati presenti per qualche parola di conforto o semplicemente di svago.

Grazie ai miei parenti. In particolare alle mie due nonne, i pilastri della mia esistenza, una che mi guarda da quaggiù e non smette mai di dirmi bravo e l'altra da lassù, ca spero sì fiera 'e mme.

Grazie alla mia famiglia. Grazie a Jacopo, la cui esperienza e il cui percorso sono sempre stati per me fonte di immensa ispirazione. Grazie a Teresa e Flavio, mia mamma e mio papà, per avermi insegnato i valori fondamentali, per avermi sostenuto nelle sfide e per aver creduto in me. Grazie a papà Flavio, che non è ingegnere solo perchè il Politecnico non gli ha ancora consegnato la laurea ad honorem, e che mi ha trasmesso questa passione. Grazie a mamma Teresa, che è la mamma migliore del mondo e non serve altro.

Last but not least, grazie a Martina. Mia amica e compagna. Perchè mi sopporti e mi supporti, e perchè sei il mio porto sicuro in ogni situazione. Grazie per le difficoltà superate insieme, perchè solo noi sappiamo quanta forza sappiamo darci l'un l'altro.

Jonathan,
Giugno 2023

Per aspera,
ad astra